Study of Charmed Baryon Sigma(C)(2800) Production at the BaBar Experiment

Shamona Ahmed

SLAC-R-887

Prepared for the Department of Energy
under contract number DE-AC02-76SF00515

Printed in the United States of America. Available from the National Technical Information Service, U.S. Department of Commerce, 5285 Port Royal Road, Springfield, VA 22161.

Study of Charmed Baryon $\Sigma_c(2800)$ Production at the *BABAR* Experiment

by

Shamona Ahmed

A Dissertation

submitted to The University at Albany

State University of New York

in Partial Fulfillment of

the Requirements for the Degree of

Doctor of Philosophy

College of Arts & Sciences

Department of Physics

2006

Study of Charmed Baryon $\Sigma_c(2800)$ Production at the *BABAR* Experiment

by

Shamona Ahmed

Study of Charmed Baryon $\Sigma_c(2800)$ Production at the *BABAR* Experiment

Shamona Ahmed, Ph.D.

Advisor: Professor M. Sajjad Alam

The University at Albany, State University of New York, 2006

This dissertation reports on a study of search for an orbitally excited state of charmed baryons $\mathbf{\Sigma}_c^0(2800)$ and $\mathbf{\Sigma}_c^{++}(2800)$. We measure the widths, momentum spectrum and production cross-section for these states decaying into a Λ_c^+ and a charged π.

The analysis uses 230 fb^{-1} of data collected at *BABAR* detector operating at PEP-II collider at Stanford Linear Accelerator Center. The data is collected in the region of $\Upsilon(4S)$ and ≈ 40 MeV below the resonance. Λ_c^+ baryon is reconstructed in the decay mode $pK^-\pi^+$. The $\Sigma_c(2800)$ baryon production at continuum is observed to be quite significant for $x_p > 0.7$, where $x_p = \frac{p}{\sqrt{E^2+M^2}}$ is the scaled momentum and varies from 0.0 to 1.0. The momentum spectrum is measured by considering the corrected yield for momentum bins above $x_p > 0.5$ and can be parameterized very well by a Peterson function, given by;

$$\frac{dN}{dx_p} \propto \frac{1}{x_p\left(1 - \frac{1}{x_p} - \frac{\epsilon}{1-x_p}\right)^2}, \tag{1}$$

The values for the peterson parameter ϵ, are found to be 0.050 ± 0.010 for $\Sigma_c^0(2800)$ and 0.057 ± 0.012 for $\Sigma_c^{++}(2800)$. We use the momentum spectrum to evaluate the

production cross-sections to be;

$$\sigma(e^+e^- \to \Sigma_c^0(2800)X).\mathcal{B}(\Sigma_c^0(2800) \to \Lambda_c^+\pi^-) = 1.36 \pm 0.42\ pb \tag{2}$$

and

$$\sigma(e^+e^- \to \Sigma_c^{++}(2800)X).\mathcal{B}(\Sigma_c^{++}(2800) \to \Lambda_c^+\pi^+) = 1.68 \pm 0.54\ pb. \tag{3}$$

We also measure the widths to be 65.6 ± 14.9 MeV and 67.7 ± 16 MeV, for the neutral and charged modes, respectively, and the corresponding observed mass differences $(\Lambda_c^+\pi - \Lambda_c\ + 2.285)$, are $2.8008 \pm 0.0023 \mathrm{GeV/c^2}$ and $2.7980 \pm 0.0028 \mathrm{GeV/c^2}$. The uncertainty here is statistical only.

Biographical Sketch

Shamona Ahmed was born in Islamabad, where she grew up and went to high school. After completing her Bachelors, she decided to pursue a career in Physics and joined the Physics Program at Quaid-i-Azam University in Islamabad. She completed her M.Sc.(equivalent to US Bachelors degree) in Physics in 1994 and joined the Advanced Theoretical Physics Program at Quaid-i-Azam University. She finished her MPhil. in Theoretical Astro-Physics in 1996. While she was working as a Medical Physicist at Shifa International Hospital Islamabad, she recieved an offer of Research Assistantship from Prof. Sajjad Alam. She joined Ph.D. program at State University of New York at Albany in 1998. She recieved her M.S. in Physics in 2000. She joined the High Energy Physics group and was part of the CLEO collaboration in the beginning. Later the group joined Babar Experiment at Stanford Linear Accelerator Center and she became a member of the Collaboration in 2001.

To my Father and (late) Mother

Acknowledgments

This thesis is a labor of love; a product of numerous direct and indirect contributions. Though the task is momentous, yet I will try my best to thank all those individuals who lent their help and support to me throughout this arduous work.

At the onset, I would like to thank my mentor and advisor, Dr.M Sajjad Alam for giving me the opportunity to work at Albany High Energy Physics Group and for achieving my goal. His never ending support, encouragement and kind guidance has helped me stay the course to the end.

A very special thanks is owed to Dr.Frank Wappler for his readily available solutions to all kinds of problems.

I am particularly grateful to my fellow group members, Rahmi Bula, Vivek Jain, Liu Jian, Bin Pan, M Saleem and Samya Zain. It was a pleasure working with all of them. A special thanks is reserved for all the BABAR collaborators as well as the PEP-II staff for their hard work in providing data and analysis tools.

I also want to thank my thesis committee members, Dr.Jesse Ernst, Dr. Akira Inomata, Dr.Akhtar Mahmood and Dr. Brian Petersen.

A great deal of gratitude is owed to my friends Lubna, Ismat, Riffat, Fahmida, Morag and Don for all the good times we shared during my stay in Albany. Those are cherished memories that I will never forget.

I am highly indebted to my parents for teaching me how to combine a challenging career and a rewarding life. I wish my mother was here to see the finished article. I miss her so much and would say that, had it not been for them, I would not have been writing this document today.

I have special appreciation for my parents-in law Azra and Nuruddin Qazi, my

aunt Kausar, my brothers Hammad and Junaid, and the rest of my family for always being there for me through the good and the bad times.

Lastly and most importantly, I want to thank my husband Fawad for his boundless faith in me, his endless love, care and support and above all, his sacrifice without which this milestone would have always remained a distant dream for me.

I conclude this piece with loving thoughts of my little angel Maryam; the joy of my life. Her presence and company gave meaning and purpose to the dreary days and nights I spent toiling after physics problems and compelled me to finish as early as possible.

Contents

List of Figures

List of Tables

Chapter 1

Introduction

1.1 Introduction

"The most incomprehensible thing about the universe is that it is comprehensible." –Albert Einstein

Throughout history, mankind has pondered over the mysteries of the nature. Philosophers and scientists of each era have tried to answer the basic questions concerning our existence.

- What is the universe made of?
- What holds the pieces together?
- How did it all begin?
- How did it become the way it is?
- How will it all end ?

Present day particle physics research represents man's most ambitious and most organized effort to answer these questions.

1.1.1 What is Particle Physics ?

Particle physics is :

- Studying the smallest things in the universe. These things are the building blocks of everything around us: seen and unseen.
- Figuring out how the universe started, and how it got to look like it does now.
- Figuring out all the forces in the universe. Forces are what makes things happen.
- Predicting the future behavior of small particles and how they merge into bigger objects or transform into smaller ones.
- Knowing what's inside everything.
- Understanding how Energy (E) and matter (m) are related (Like in Einstein's formula).

Early astronomers, such as Ptolemy, believed that the earth was the center of the universe with all other celestial bodies revolving around it. Then came Copernicus, suggesting that the earth revolved around the sun. As the science and technology developed, new realizations about the universe unfolded and today we have a much better understanding of the present and past. In early 1900's, Henrietta Leavitt [1], solved the problem of measuring distances across the universe. She showed that Cepheid variable stars, which vary periodically in brightness, could be used to measure distances across the universe. She realized that the rate of variation of a Cepheid star gave a strong indication of its actual brightness, which could then be compared with its apparent brightness as seen from Earth, which then indicated the

distance to the star. When Cepheid variable stars were found in distant galaxies, it became possible to measure the distance to the galaxies. In 1929, Edwin Hubble (1889-1953), made the major discovery that the universe is expanding. He discovered that each galaxy is moving at a velocity which is proportional to its distance. This led the scientist to think that it all began with all the matter and energy squished into an infinitely tiny volume at one point. From this point the Universe exploded and from this original explosion not only matter and energy were created, but also space and time.

1.1.2 The Big Bang

At the beginning of time, nature is believed to have been exceedingly simple, possessing many symmetries that were subsequently broken via the actions of the governing forces as the universe expanded and passed through several phase transitions during the cooling process, as shown in Fig. 1.1 [2].

Big Bang Theory - Evidence for the Theory

- First, there is a reasonable certainty that the universe had a beginning.
- Second, the discovery of Hubble's Law, which states that the galaxies appear to be moving away from us at speeds proportional to their distance. This observation supports the expansion of the universe and suggests that the universe started off as compact.
- Third, as suggested by Big Bang, if the universe was very, very hot initially, then we should be able to find some remnant of this heat. This remnant was found in 1965, when radio-astronomers Arno Penzias and Robert Wilson

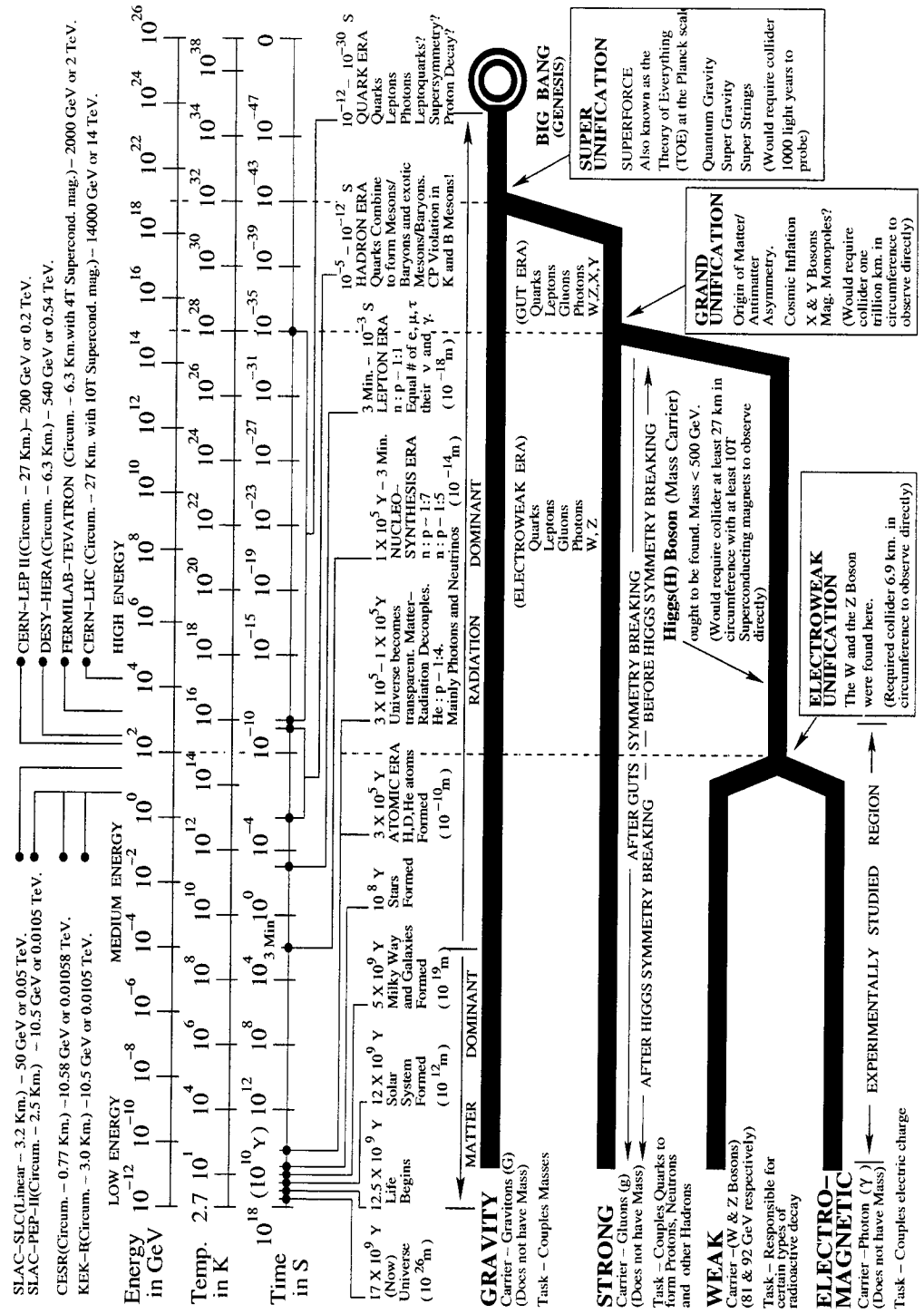

Figure 1.1: *History of the universe based on the four fundamental forces [2].*

discovered a 2.725 Kelvin (-454.765°F, -270.425°C) Cosmic Microwave Background radiation (CMB) which pervades the observable universe.

- Finally, the abundance of the "light elements" found in the universe today also support the Big Bang model of origins.

Big Bang - What happened?

Most physicists refer to the Big Bang as a "singularity" that is, an ultimate boundary or edge, a "state of infinite density" where space-time has ceased. Thus it represents an outer limit of what we can know about the universe. Assuming that there is no "before the Big Bang", here is a short summary of what went on during the various epochs:

1. **Quantum Gravity Era (The Big Bang to 10^{-43} s) :** The hot big bang model stipulates that the universe began about 13.7 billion years ago as a tiny point of infinite density and zero size. This spot exploded in a tiny, hot, dense explosion of all matter in the universe. It was tiny in the sense that all matter, and even space itself, was condensed into a single point. It was very hot and dense, and as the universe exploded, all the particles of matter and anti-matter rushed outward, away from each other. All forces were united into a single force. As time progressed, the universe expanded and cooled. As this happened, different types of interactions became dominant in the universe, defining the different cosmological epochs.

2. **GUT Era (10^{-43} s to 10^{-35} s):** Initially, the universe was comprised of the fundamental constituents of matter and lots of radiation rushing around and interacting with each other freely. It was too hot for them to combine

into stable systems, such as atoms or even protons, but too dense for them not to interact at all. During this period the gravitational force separated out and the strong, weak, and the electromagnetic force acted as a single force, as described in the Grand Unified Theory (GUT).

3. **Electroweak Era (10^{-35} s to 10^{-12} s):** Within a very small fraction of a second, the universe expanded enough, and thereby cooled sufficiently, for the strong force to become independent, leaving only the Electroweak force to continue acting as a single force. The universe contained dense soup of quarks, leptons, and massless gluons, photons, W, and Z bosons. The temperature cooled down from 10^{28} K to 10^{15} K.

4. **Spontaneous Symmetry Breaking Era (10^{-12} s to 10^{-10} s):** At this stage of the Big Bang, the universe was filled with radiation creating pairs of particles and antiparticles, and pairs of particles and antiparticles annihilating back into radiation. But as the universe expanded, it cooled, and the cooler radiation was less likely to create quark-antiquark pairs. As quarks and antiquarks "froze" out of the radiation background, a greater number of quarks than antiquarks ware left over. The universe was dominated by matter rather than antimatter. W and Z bosons acquired mass via interaction with the Higgs.

5. **Hadron Era (10^{-10} s to 10^{-6} s):** The quarks combined to form hadrons and, the electrons and positrons were in equilibrium with the photons, neutrinos and antineutrinos. Antineutrinos were combining with protons to form positrons and neutrons, and neutrinos were combining with neutrons to form electrons and protons. At this stage the number of protons was about equal to

the number of neutrons. This is the era of the Standard Model –and most of the particle physics research done nowadays is to understand the spectroscopy and interactions of particles present at that time.

6. **Proton Era (10^{-6} s to 10^{-1} s):** The temperature had dropped to 10^{11} K. Because a free neutron is slightly less stable than a free proton, neutrons underwent beta decay to form protons, electrons and anti-neutrinos. Thus, the initial approximately equal balance between neutrons and protons began to be tipped in favor of protons over the next several minutes. The free neutron is unstable, but neutrons in composite nuclei can be stable, so the decay of neutrons continued until the simplest nucleus (deuterium, the mass-2 isotope of hydrogen) could form. But the temperature implied an average energy for particles in the gas of about 2.6 MeV, and deuterium has a binding energy of only 2.2 MeV and so could not hold together at these temperatures. This barrier to the production of composite nuclei, which allows the free neutrons to be steadily converted to protons, is called the deuterium bottleneck.

7. **Lepton Era (10^{-1} s to 13.8 s):** The temperature had now fallen to about 3×10^9 K. At this temperature the neutrinos and antineutrinos ceased to play a role in the continuing evolution and decoupled from the rest of the matter and radiation. The average energy of the particles in the gas had fallen to about 0.25 MeV. This was too low for photons to produce electron-positron pairs so they fell out of thermal equilibrium and the free electrons began to annihilate all the positrons to form photons. The deuterium bottleneck still kept appreciable deuterium from forming and the neutrons continued to decay to protons. At this stage the abundance of neutrons had fallen to about 13%

and the abundance of protons had risen to about 87%.

8. **Nucleosynthesis Era (13.8 s to 3 min.):** Finally the temperature dropped sufficiently low (about 1 billion K) so that the deuterium nuclei could hold together. The deuterium bottleneck was thus broken and a rapid sequence of nuclear reactions combined neutrons and protons to form deuterium, and the resulting deuterium with neutrons and protons to form the ^{4}He. Thus, all remaining free neutrons were rapidly "cooked" into ^{4}He, ^{3}He, ^{2}He and ^{7}Li. Excess of protons resulted in excess of hydrogen over helium, as observed today.

9. **Radiation Era (3 min. to 10^5 years):** The Universe was still expanding and cooling. But as this happened more and more matter was created. Eventually the energy density in matter became larger than the energy density in radiation. Atoms condensed without being ionized. As the free electrons are bound up in atoms, the primary cross section leading to the scattering of photons (interaction with the free electrons) was removed and the universe (which had been very opaque until this point) became transparent: light could now travel large distances. The photons could now move through space without being absorbed. As a result the energy exchange between matter and radiation became less efficient. The photons thermalized and started behaving as black body radiation. Due to continued expansion this temperature fell from 10^9 K to a few degrees above absolute zero. The measured temperature of this cosmic microwave background today is 2.725 K [3].

10. **Formation of Galaxies and Stars (2-13 billion years):** When stars first began to form and galaxies took shape, hydrogen, helium and lithium

were basically the only three elements in the Universe. The heavier elements come from inside stars. Stars consume hydrogen and create heavier elements through the process of nuclear fusion. The heavier elements we see in the world today were all ejected from stars that had reached the end of their lifespan and exploded into supernovas before settling into old age as a white dwarf, a neutron star or a black hole (The process of making the heavy elements and then ejecting them into the Universe takes place over a time scale that is the lifespan of a star).

11. **Life Evolved (13 Billion years to present):** The events leading to the origin of life are perhaps the least understood chapters of the story. Life began during the first billion years of an Earth history which encompasses approximately 4.5 billion years. In the beginning volcanoes, oceans, and a turbulent atmosphere dominated the landscape. Chemical activity in clouds which were fed by volcanoes and penetrated both by lightning discharges and solar radiation, along with the oceans which received organic matter from the land and the atmosphere, as well as from in falling meteorites and comets were important factors in evolution of life. Here, substances such as water, carbon dioxide, methane, and hydrogen cyanide formed key molecules such as sugars, amino acids, and nucleotides. Such molecules were the building blocks of proteins and nucleic acids, compounds ubiquitous to all living organisms. A critical early triumph was the development of RNA and DNA molecules, which directed biological processes and preserved life's "operation instructions" for future generations.

    Most of life's history involved the biochemical evolution of single-celled micro-

organisms. Individual fossilized microbes in rocks which are 3.5 billion years old have been found, yet we can conclusively identify multi-celled fossils only in rocks younger than 1 billion years. The oldest microbial communities often constructed layered mound-shaped deposits called stromatolites, whose structures suggest that those organisms sought light and were therefore photosynthetic. These early stromatolites grew along ancient seacoasts and endured harsh sunlight as well as episodic wetting and drying by tides. Thus it appears that, even as early as 3.5 billion years ago, micro-organisms had become remarkably durable and sophisticated.

Many important events mark the interval between 1 and 3 billion years ago. Life learned how to release oxygen from water, and it populated the newly expanded continental shelf regions. Finally, between 1 and 2 billion years ago, the eukaryotic cells with their complex system of organelles and membranes developed and began to experiment with multi-celled body structures. Jellyfish and sea-pens are of those primitive life forms. The evolution of the plants and animals most familiar to us occurred only in the last 550 million years, the appearance of marine invertebrates (such as shell-making ammonites), then fish, amphibians, reptiles, mammals, and humanity.

Perhaps the most recent significant evolutionary innovation has been humanity's ability to record and build upon its experience, thus triggering the rise of civilization and technology. These developments bring us to the present, and here we are, trying to uncover the secrets of this marvelous Universe.

1.2 History of Elementary Particle Physics

From the Big Bang theory, it is clear that the creation of universe was a very complicated process. Particle Physics is the quest to understand and reveal the nature of those basic constituents of matter that existed during the Big Bang (actually approximately Era 4).

In the last century scientists have learned to make these particles in the laboratories. And by studying them, we hope to learn about the origin of the universe. It is through particle physics, the tunning fork of the intellectual sphere of mankind, that we hope to understand the birth and the ultimate future of the universe. A major portion of Big Bang is beyond the Standard Model. This period at the moment also lies beyond what we can study with current accelerators. Even with the LHC($E \approx 14$ TeV), we will merely reach up to 10^{-14} s, just a tiny fraction of this era. Regardless, although we cannot be sure what LHC may (or may not) discover, we can try to answer as many questions as we can with the current technology available to us.

In 1897, the first of the basic particles, the electron was discovered by Joseph John Thomson. So began a remarkable journey inward to smaller and smaller distance scales, from 10^{-10} m to 10^{-15} m and eventually 10^{-18} m, from an atom composed of electrons and a nucleus, to the nucleus composed of protons and neutrons, to protons and neutrons composed of quarks - soon to realize and discover that there are six quark "flavors" and six leptons. Table 1.1 gives a sense of how the various particles were first discovered.

With these discoveries of the fundamental constituents of matter came an understanding of the interactions between them via the three of the four fundamental

Table 1.1: History of Elementary Particle Physics

Era	Discoveries	Scientists	Year
Classical (1897-1932)	Electron	J.J.Thomson	1897
	Proton	E.Rutherford	1919
	Neutron	J.Chadwick	1931
The Photon (1900-1924)	Blackbody Spectrum	M.Planck	1900
	Photoelectric Effect	A. Einstein	1905
	Compton Scattering	A.H.Compton	1923
Mesons (1934-1963)	Strong Force	H.Yukawa	1933-34
	Muon	C.Powell...	1937
	$\pi^{\pm}$	C.Powell...	1947
	Λ		1951
	π^0		1958
	ρ, ω, η		1961
	η', Ω^-		1963
Antiparticles (1930-1956)	Dirac equation	P.A.M.Dirac	1927
	Positron	C.D.Anderson	1931
	Anti Proton	E.Segrè & O.Chamberlin	1955
	Anti Neutron	B Cork*et al.*	1956
Neutrinos (1930-1962)	Proposed neutrino	W.Pauli	1930
	Theory of beta decay	E.Fermi	1933-34
	ν_e	C.Cowan & F.Reines	1956
	ν_μ		1962
Strange Particles (1947-1960)	K^0	Q.Rochester & C.Butler	1947
	K^+	Powell	1949
	Σ, Ξ, Δ		1950-60
	Strangeness Conservation rules	M.Gell-Mann & K.Nishijima	1953
The Eightfold Way	Baryon & Meson Octets	M.Gell-Mann	1961
	Baryon Decuplet		
The Quark Model	Quark Idea	M.Gell-Mann & Q.Zweig	1964
	substructure for baryons	SLAC & CERN	
	Color quantum Number	O. W. Greenberg	1964
Heavy Flavor Particles	c-quark	S.Ting & B.Richter	1974
	Λ_c^+ Σ_c^{++}		1975
	τ	M. Perl	1976
	D^0 D^+	G Goldhaber & F pierre	1976
	Υ, Υ', Υ''	L. Lederman	1977
	Λ_b	G. Bari*et al.*	1992
	t-quark		1995
Intermediate Vector Bosons	Prediction of $W^{\pm}$, Z^0	Glashow, Weinberg & Salam	1967
	Discovery of $W^{\pm}$, Z^0	C.Rubbia & S. Van der Meer	1983

forces, the electromagnetic, the weak and the strong force. A remarkable achievement of the last quarter of the 20th century has been the unification of the electromagnetic and the weak force, known as the electroweak force. This electroweak force, the strong force, six quarks and the six leptons form the basis of what we call the Standard Model (SM).

1.3 The Standard Model: Quarks, Leptons and the Fundamental Forces

The Standard Model [4] (SM), provides a theoretical description of interactions between elementary particles. This model has proven to be the most adequate in explaining current experimental observations in High Energy Physics. It not only provides a framework in which high energy physicists can work but also the basis on which a more extended theory may be built in future. The development of the Standard Model came about through theoretical and experimental advances, at times theorists making predictions which were later confirmed by experiments while at other times, unexpected experimental results improved the physical theories.

In the Standard Model, the fundamental constituents of matter are either quarks or leptons. These quarks and leptons are spin $\frac{1}{2}$ particles and are called fermions (named for the Italian physicist Enrico Fermi). Altogether there are 24 such elementary particles; the 6 quark flavors (u, d, c, s, t, b) all of which carry either a fractionally positive or negative charge, and 6 anti-quark flavors which carry the fractional charges in opposite manner, and the 6 leptons (the Greek for the "light ones") out of which 3 are negatively charged (e, μ , τ) and 3 are their corresponding neutrally charged neutrinos (ν_e, ν_μ, ν_τ), similarly there are 6 anti-leptons carrying

positive and neutral charges, respectively.

Interactions between the constituents of matter are mediated by the gauge bosons (named for the Indian physicist, S.N.Bose). Corresponding to four fundamental forces there are spin 1 bosons for the electromagnetic, weak and strong force and spin 2 for the gravitational force. The classical treatment of these forces was as fields or potentials but the modern Quantum Field Theory views the interaction to be an exchange of "vector gauge bosons".

1.3.1 Quarks and Leptons

The quarks and leptons are grouped into three families or generations of isospin doublets, denoted as I, II and III as given in Eq. 1.1.

$$\begin{array}{cccccc} & \underline{\text{Leptons}} & & & \underline{\text{Quarks}} & \\ I & II & III & I & II & III \\ \begin{pmatrix} e \\ \nu_e \end{pmatrix} & \begin{pmatrix} \mu \\ \nu_\mu \end{pmatrix} & \begin{pmatrix} \tau \\ \nu_\tau \end{pmatrix} & \begin{pmatrix} u \\ d \end{pmatrix} & \begin{pmatrix} c \\ s \end{pmatrix} & \begin{pmatrix} t \\ b \end{pmatrix} \end{array} \tag{1.1}$$

While both quarks and leptons are treated as elementary particles, quarks are bound inside the hadrons. Leptons interact weakly and electromagnetically, but not strongly, whereas quarks interact weakly, electromagnetically and strongly. The sizes (charge radius) of these quarks and leptons are $< 10^{-18}$ m.

The first family of both leptons and quarks are long-lived and constitute the matter which makes the world around us. The other two families form the short-lived hadronic matter, which is believed to have existed between 10^{-12} to 10^{-6} seconds after the Big Bang. Since the u and d quarks make up nearly all of ordinary matter, they can be studied easily. Whereas for the heavy quarks, charm and beauty bound within hadrons, we can only study them by producing, detecting and then

reconstructing them in the high energy physics laboratories around the world. They are good candidates for the study of weak and electromagnetic interactions and its inter-play with the strong interaction.

The quarks and leptons, both carry additional distinct properties or quantum numbers which further distinguish these two classes of fermions. Leptons carry a baryon number of 0 and quarks carry a baryon number of $\frac{1}{3}$. This baryon number has to be conserved during each interaction. Leptons have a lepton quantum number L, further divided into three separate lepton numbers L_e, L_μ, and L_τ corresponding to each lepton family, and that too needs to be conserved separately in each interaction. Further, quarks also have the four flavor quantum numbers S, C, B, T for the s, c, b and t quarks. Tables 1.2 and 1.3 list the summary of lepton and quark properties, respectively.

Table 1.2: Summary of Lepton Properties as given in [5]

Lepton Name	Symbol	Charge (e)	Mass (MeV/c^2)	J	Baryon #	Electron #(L_e)	Muon #(L_μ)	Tauon #(L_τ)	Lifetime (sec)
electron	e	-1	0.511	$\frac{1}{2}$	0	+1	0	0	stable ($> 10^{26}$ Years)
electron neutrino	ν_e	0	$< 3 \times 10^{-3}$	$\frac{1}{2}$	0	+1	0	0	stable
muon	μ	-1	105.7	$\frac{1}{2}$	0	0	+1	0	2.197×10^{-6}
muon neutrino	ν_μ	0	< 0.19	$\frac{1}{2}$	0	0	+1	0	stable
tauon	τ	-1	1777.0	$\frac{1}{2}$	0	0	0	+1	2.91×10^{-13}
tau neutrino	ν_τ	0	< 18.2	$\frac{1}{2}$	0	0	0	+1	stable

Table 1.3: Summary of Quark Properties as given in [5]

Quark Flavor	Symbol	Charge (e)	Mass (GeV/c^2)	J^p	Baryon #	I	I_3	Y	S	C	B	T
up	u	$+\frac{2}{3}$	0.0015 - 0.004	$\frac{1}{2}^+$	$\frac{1}{3}$	$\frac{1}{2}$	$+\frac{1}{2}$	$+\frac{1}{3}$	0	0	0	0
down	d	$-\frac{1}{3}$	0.004 - 0.008	$\frac{1}{2}^+$	$\frac{1}{3}$	$\frac{1}{2}$	$-\frac{1}{2}$	$+\frac{1}{3}$	0	0	0	0
charm	c	$+\frac{2}{3}$	1.15 - 1.35	$\frac{1}{2}^+$	$\frac{1}{3}$	0	0	$+\frac{4}{3}$	0	+1	0	0
strange	s	$-\frac{1}{3}$	0.08 - 0.13	$\frac{1}{2}^+$	$\frac{1}{3}$	0	0	$-\frac{2}{3}$	-1	0	0	0
top	t	$+\frac{2}{3}$	174.3 ± 5.1	$\frac{1}{2}^+$	$\frac{1}{3}$	0	0	$+\frac{4}{3}$	0	0	0	+1
bottom	b	$-\frac{1}{3}$	4.1 - 4.4	$\frac{1}{2}^+$	$\frac{1}{3}$	0	0	$-\frac{2}{3}$	0	0	-1	0

For each of the above particles, there also exists an antiparticle. The antiparticle possesses the same mass and spin as that of its corresponding particle, but is of opposite charge, baryon number, and lepton number. Besides flavor, quarks carry another degree of freedom, called "color," which comes in three varieties ("red," "green," and "blue," or in short, r, g, and b). Antiquarks carry anticolors. According to the (SM) all observable particles are colorless, consistent with the fact that no single quark has been observed experimentally. This means that either a color and the corresponding anticolor come together or all three different colors are mixed together to form a hadron. Hadrons are therefore formed by either quark-antiquark pairs (mesons) or by colorless mixtures of three quarks (baryons). Naturally, a meson has B=0 and a baryon has B=1. For mesons, colorless states are easily formed by combining a quark of a particular color with an antiquark of the same (anti-)color, leaving the mesons with no net color. In the case of the baryons, there are numerous ways to form colorless states by combining three quarks.

In the language of group theory, the three colors generate a color SU(3) symmetry, and the colorless states correspond to the singlet representation of the color symmetry group. For the quark-antiquark combination, the direct product of quark and antiquark representations of SU(3) may be decomposed into the direct sum of an 8-dimensional (octet) representation and the one-dimensional (singlet) representation as;

$$3 \otimes \overline{3} = 8 \oplus 1.$$

The singlet representation yields colorless states; for instance, the positively charged pion is given by;

$$\psi(\pi^+) \sim u_r\overline{d}_r + u_g\overline{d}_g + u_b\overline{d}_b,$$

which is completely symmetric under the exchange of any two colors and certainly

compatible with the boson nature of the pion. When combining the three quarks of three different colors, the direct product of three fundamental representations of SU(3) decomposes according to the rule;

$$3 \otimes 3 \otimes 3 = 10 \oplus 8 \oplus 8 \oplus 1.$$

By combining three colors, we obtain a color decuplet, two color octets, and a color singlet. Only the color singlet state of a baryon is completely antisymmetric under the interchange of any two quarks. The color state of all baryons is therefore given by;

$$\Psi(\text{color}) = \frac{1}{\sqrt{6}} \left[(\text{r},\text{g},\text{b}) - (\text{r},\text{b},\text{g}) + (\text{g},\text{b},\text{r}) - (\text{g},\text{r},\text{b}) + (\text{b},\text{r},\text{g}) - (\text{b},\text{g},\text{r})\right],$$

which, by definition, has to be antisymmetric for fermions. The total wave function of any hadron can be expressed as;

$$\Psi = \Psi(\text{space})\,\Psi(\text{spin})\,\Psi(\text{flavor})\,\Psi(\text{color}),$$

In the case of baryons, where the color part of the wave function is always antisymmetric, the combination of the remaining parts must always be symmetric. For example, the wave function of the Σ_c^0 baryon is the product of the antisymmetric baryon color singlet, given above and the symmetric flavor-spin factor

$$\begin{aligned}\Psi(\Sigma_c^0) \;=\; \frac{1}{\sqrt{8}} \big[\, & 4/3\ (d\uparrow, d\uparrow, c\downarrow) - 2/3\ (d\uparrow, d\downarrow, c\uparrow) - 2/3\ (d\downarrow, d\uparrow, c\uparrow) + \\ & 4/3\ (d\uparrow, c\downarrow, d\uparrow) - 2/3\ (d\uparrow, c\uparrow, d\downarrow) - 2/3\ (d\downarrow, c\uparrow, d\uparrow) + \\ & 4/3\ (c\downarrow, d\uparrow, d\uparrow) - 2/3\ (c\uparrow, d\uparrow, d\downarrow) - 2/3\ (c\uparrow, d\downarrow, d\uparrow)\,\big],\end{aligned}$$

The possible number of mesons and baryons constructed in the above way easily exceeds one hundred, many of which have been confirmed experimentally [5].

1.3.2 Fundamental Forces

The interactions between particles can be one of the four types, strong, weak, electromagnetic or gravitational. The four fundamental forces and their mediators after the Higgs symmetry breaking when all the four forces act as separate entities.are shown in Table 1.4. Before the Higgs symmetry breaking the electromagnetic and weak forces are unified as one force described by the Standard model and have four mediators W^+, W^-, Z^0 and γ. Since all mediators have integer spin=1, they follow Bose-Einstein statistics and transform as polar vectors under rotation. Table 1.5 shows a comprehensive list of the properties of the four forces.

Table 1.4: Forces and their Mediators.

Forces	Mediators
Strong	$g_1 ... g_8$
Electromagnetic	γ
Weak	W^+, W^-, Z^0
Gravitational	G

Gravitational force mediated by the spin-2 massless gravitons that act on mass-energy is the weakest of the four forces. It is a long-ranged (extends out to infinity) force that binds all massive particles together with an attraction that is proportional to their masses and falls off with the distance squared between them. The gravitational force acts on all particles, however, it is far too weak to play any significant role in subatomic objects such as quarks or leptons and it is not considered a part of the Standard Model.

The electromagnetic (EM) force was first observed as an extra-nuclear phenomenon and is also a long-ranged force like the gravitational force. It is mediated

Table 1.5: Properties of the four fundamental forces [5]

Forces	Strong	Electromagnetic	Weak	Gravitational
		Electroweak		
Mediator	Gluon (g)	Photon (γ)	$W^{\pm}$, Z^0	Graviton (G)
		Higgs(H^0) - Electroweak Mass Carrier		
Spin	1	1	1	2
Mass (GeV/c^2)	0	0	81.0 ($W^{\pm}$) 92.0 (Z^0)	0
Lifetime (s)	N/A	∞	3.2×10^{-25}($W^{\pm}$) 2.65×10^{-25}(Z^0)	N/A
No. of Mediators	8	1	3	1
Range (m)	$\leq 10^{-15}$	∞	$\leq 10^{-18}$	∞
Rel. Strength (Coupling Const.)	$\alpha_s = 1(10^0)$ at 1 GeV ($\alpha_s = 10^2\alpha_e$) $\alpha_s \sim 1$, large r $\alpha_s < 1$, small r	$\alpha_e = \frac{1}{137}(10^{-2})$ at 1 GeV	$\alpha_w = 10^{-6}$ at 1 GeV ($\alpha_w = 10^{-4}\alpha_e$)	$\alpha_g = 10^{-38}$ at 10^{15} GeV ($\alpha_g = 10^{-36}\alpha_e$)
Interaction Lifetime (s)	$10^{-23} - 10^{-24}$	$10^{-17} - 10^{-20}$	$10^{-6} - 10^{-13}$	N/A
Cross Sec. at 1 GeV (μb)	10^4	10^1	10^{-8}	N/A
Interacting Fermions	Quarks	Quarks Charged Leptons	Quarks Charged Leptons Neutral Leptons	Quarks Charged Leptons Neutral Leptons
Acts On	Color Charge (R,G,B)	Electric Charge	Quark Flavor Leptons	Mass-Energy
Field Theory	QCD	QFD	QED	QGD
Symmetry Group	$SU(3)_c$	$U(1)$	$SU(2)$	$SO(N)$ $E_8 \otimes E_8$ Superstrings
Local Symmetry		$SU(2) \otimes U(1)$		
	$SU(3)_c \otimes SU(2) \otimes U(1)$: After GUTs Symm. Breaking			
Experimental Evidence	Observed Directly at DESY-TASSO in 1979	Observed Directly in the Early 1900s	Observed Indirectly CERN-UA1 in 1983	Observed Indirectly as Gravity Waves in Binary Pulser PSR 1913+16 in 1974

by the massless photons (γ) acting on electric charge and becomes weaker as the distance between two particles or objects increases. Besides gravitation, it is the one responsible for most of the physical interactions that take place at the human length scale. Unlike the gravitational force, the EM force can be either attractive for particles with opposite charges, or repulsive for particles with like charges, that falls off with the distance squared between two charged particles. The theory describing electromagnetic interactions is called Quantum Electrodynamics (QED).

The strong and the weak forces are both short ranged, in contrast to the gravitational and the electromagnetic force. While the EM interaction range is infinite, the strong interactions occur on the order of a Fermi. The protons inside a nucleus are electrically repelled from each other, nevertheless they are held in the nucleus by the "strong" force, so called, since it is about 100 times stronger than the electromagnetic force. The strong force is also what holds the quarks together inside hadrons, and is therefore responsible for binding three quarks together to form baryons and a quark and an anti-quark to form mesons. The field theory describing the strong force is called Quantum Chromodynamics (QCD). The strong force is mediated by eight spin-1 massless gluons, $g_1 ... g_8$. While photons do not carry electric charge, gluons on the other hand, carry the color quantum number like the quarks, and thus can interact via the strong force. The fact that the gluons interact among themselves through the strong force leads to an increase in the strong force between quarks and gluons with distance. The farther apart the quarks and gluons are, the more strongly they attract one another (which is why quarks do not exist separately, but always bound as hadrons) and any effort to pull quarks and gluons out of the nucleon by supplying energy, is therefore bound to fail. For this reason, the effect of the strong force between hadrons is of short range and vanishes when the colorless

hadrons are far apart. In contrast, the EM force gets weaker, gradually, as the separation distance increases. Leptons do not have color charge and do not interact via the strong force. As a result, leptons can exist independently as free particles.

The fourth force is the weak force and is about 10^4 times weaker than the electromagnetic force and about 10^{32} times stronger than the gravitational force. However, the weak force does not hold particles together since it can act only over extremely short distance ($< 10^{-18}$ m) and so instead, it is responsible for radioactive decay of nuclei (β-decay) in particular and for changing a heavy quark to a lighter quark (via changing the flavors), or changing a lepton to a lighter lepton. However, it should be noted that no flavor changing neutral currents exist in nature at tree level and only flavor changing charge currents exist.

Lifetimes of weakly decaying particles are large compared to typical EM and strong decays. The weak force is carried or mediated by one of three particles called W^+, W^- and Z^0 bosons. Unlike the other force carriers, the photon and gluon, the weak force carriers have mass. In fact, this is the reason for the weak force being very short ranged force. The weak interaction acts on all leptons and quarks, all of which carry "weak charges."

Using the same analogy that Maxwell did to reveal that the electric and the magnetic forces are different aspects of the same electromagnetic force, a field theory of the weak force called the electroweak theory was developed. It successfully proved that the electromagnetic force and the weak force are different aspects of a single electroweak force. The strength of the weak force is related to the electromagnetic coupling constant through the equation given in 1.2 [4].

$$\alpha_w \approx \alpha_e \, tan \, \theta_W \tag{1.2}$$

where θ_W is called the "Weinberg angle". This relationship between the electromagnetic and the weak force is one of the major advancements of the electroweak theory and hence the SM, which unified the two forces. The three interactions of interest in particle physics are therefore described by two theories, Quantum Chromodynamics (QCD) and the Electroweak theory of Glashow, Weinberg, and Salam. The Electroweak unification is discussed in detail in the next section.

All kinds of interactions, whether its a scattering with another particle or a decay into lighter particles, or an annihilation into heavier particles, they are governed by some conservation rules. Table 1.6 shows a list of some of the quantities conserved or violated for each type of the force. While some of the conservation rules are absolute, others depend on the type of the force, the interaction is mediated by.

Table 1.6: Conservation Rules for the four forces [4]

Quantity Conserved	Strong	Electromagnetic	Weak
Charge	Yes	Yes	Yes
Energy/Momentum	Yes	Yes	Yes
Baryon Number	Yes	Yes	Yes
Lepton Number	Yes	Yes	Yes
Isospin (I)	Yes	No	No ($\Delta I_3 = 0, \frac{1}{2}, 1$ or $\frac{3}{2}$)
Strangeness (S)	Yes	Yes	No ($\Delta S = 0$ or 1)
Hypercharge (Y)	Yes	Yes	No
Charm (c)	Yes	Yes	No ($\Delta C = 0$ or 1)
Beauty (B)	Yes	Yes	No ($\Delta B = 0$ or 1)
Parity (P)	Yes	Yes	No
G-Parity (G)	Yes	No	No
Charge Conjugation (C)	Yes	Yes	No
CP	Yes	Yes	No
Time-reversal (T)	Yes	Yes	No
CPT	Yes	Yes	Yes

1.3.3 Electroweak Interaction

In 1967–68, Glashow, Weinberg, and Salam proposed a gauge theory unifying the weak and the electromagnetic interactions [6]. In the gauge field theory, the Lagrangian is invariant under local gauge transformations provided that all gauge fields involved are massless. In renormalizable theories, the unphysical divergent terms that exist in quantum field theories must be cancelled to describe an observable physical process. The Electroweak Unification is basically an extension of QED [4], which is a gauge field theory describing electromagnetic interactions based on the U(1) symmetry group. The Lagrangian of QED is invariant under a global $U(1)$ transformation where the electron's field everywhere is changed by an arbitrary phase. QED is also invariant under a local phase transformation whereby the phase of the electron's field can change arbitrarily at different locations. It is important to note that while the Lagrangian of a free charge, represented by the current J^{μ}, is not invariant under a local $U(1)$ transformation, the electromagnetic field (A_{μ}) compensates for this and leaves the Lagrangian invariant under a local $U(1)$ transformation. The fact that the symmetry of $U(1)$ phase transformations is unbroken requires electric charge to be conserved which is observed in all interactions.

The Glashow-Weinberg-Salam theory (GWS) used a "weak isospin", I, $SU(2)$ group and a "weak hypercharge", Y, $U(1)$ group (where $Y = 2(Q - I_3)$), thus forming a non-Abelian $SU(2) \otimes U(1)$ gauge symmetry group to describe the electroweak gauge field. The combination $SU(2) \otimes U(1)$ reveals the symmetry between the lepton and quark families, plus the similarities between electromagnetic and weak interactions. In the Standard Model, fermions are grouped into three generations of left-handed doublets and right-handed singlets of weak isospin given as;

$$\begin{pmatrix} \nu_e \\ e \end{pmatrix}_L, \begin{pmatrix} \nu_\mu \\ \mu \end{pmatrix}_L, \begin{pmatrix} \nu_\tau \\ \tau \end{pmatrix}_L \quad , \quad e_R,\, \mu_R,\, \tau_R,$$

$$\begin{pmatrix} u \\ d \end{pmatrix}_L, \begin{pmatrix} c \\ s \end{pmatrix}_L, \begin{pmatrix} t \\ b \end{pmatrix}_L \quad , \quad u_R,\, c_R,\, t_R,\, d_R,\, s_R,\, b_R.$$

Only the left-handed doublets participate in the weak interactions. The weak isospin doublets serve as the bases of the $SU(2)$ group, while the isosinglets form the bases of the $U(1)$ group.

The two components, right- and left-handed, ψ_R and ψ_L, of a fermion field, ψ are obtained by applying the projection operators: $\psi_R = \frac{1}{2}(1+\gamma_5)\psi$ and $\psi_L = \frac{1}{2}(1-\gamma_5)\psi$. The left handed Fermion fields transfer as doublets under $SU(2)$ rotations, and the right handed fields transform as singlets. This is a consequence of the fact that weak interactions violate parity maximally and are mediated by V-A (Vector-Axial) interactions.

A Lagrangian which is invariant with respect to the weak isospin $SU(2)$ and with respect to rotations in weak hypercharge space, is needed. There are four electroweak bosons, the weak isospin triplet W_μ^i with $i = 1, 2, 3$, and the singlet B_μ, relating to the $SU(2)$ and the $U(1)$ groups, respectively. The two charged bosons, W_μ^1 and W_μ^2, , couple with a scalar Higgs field via a spontaneous symmetry breaking mechanism [7], to become the massive $W^+$and W^-. The linear combination of the neutrals, W_μ^3 and B_μ couple with the Higgs to form a massive neutral vector boson Z^0 and the massless photon. The presence of the Higgs field is essential for the renormalizability of the theory.

The interaction energy (usually represented by the so-called Lagrangian energy density $\mathcal{L}$) of fermions with the fields W_μ, B_μ is the product of the fermion currents

and fields, that is of the form

$$\mathcal{L}_{int} = g_w \mathbf{J}_\mu \cdot \mathbf{W}_\mu + g_z J_Y^\mu B_\mu \tag{1.3}$$

where $\mathbf{J}$ and J_Y^μ represent the isospin and hypercharge currents of the fermions (leptons or quarks) respectively, and g_w and g_z are their couplings to $\mathbf{W}_\mu$ and B_μ. The hypercharge current is related to the electromagnetic current J_μ^{EM} and the third component of the isospin current J_μ^3 by;

$$J_\mu^Y = J_\mu^{EM} - J_\mu^3 \tag{1.4}$$

The electroweak interaction Lagrangian contains three terms, one for the weak charged current interaction, one for the weak neutral current interaction and one for the electromagnetic interaction;

$$\mathcal{L}_{int} = \frac{g_w}{\sqrt{2}} \left(J_\mu^- W_\mu^+ + J_\mu^+ W_\mu^- \right) + g_z \left(J_\mu^0 - sin^2\theta_w \, J_\mu^{EM} \right) Z_\mu + e \, J_\mu^{EM} A_\mu \ ,$$

with the weak charged and neutral current coupling constants being related to the basic unit of electric charge through the "Weinberg angle" θ_w;

$$\begin{aligned} g_w &= \frac{e}{sin\theta_w} \ , \\ g_z &= \frac{e}{sin\theta_w \, cos\theta_w} \ . \end{aligned}$$

The $W_\mu^\pm$, Z_μ, and A_μ are the field operators representing the physical $W^\pm$, Z^0, and γ particles, respectively. As noted earlier, they are given by the linear combinations of electroweak bosons;

$$\begin{aligned} W_\mu^\pm &= (W_\mu^1 \pm i \, W_\mu^2) / \sqrt{2} \ , \\ Z_\mu &= W_\mu^3 \, cos\theta_w - B_\mu \, sin\theta_w \ , \\ A_\mu &= W_\mu^3 \, sin\theta_w + B_\mu \, cos\theta_w \ . \end{aligned}$$

Finally, the $J_\mu^\pm$, J_μ^0, and J_μ^{EM} denote the charged weak, neutral weak, and electromagnetic currents. The charged weak current are given by the first two components of the isospin current;

$$J_\mu^\pm = J_\mu^1 \pm J_\mu^2 \tag{1.5}$$

The charged weak current for leptons is given by;

$$J_\mu^+ = (\overline{\nu}_e, \overline{\nu}_\mu, \overline{\nu}_\tau) \frac{1}{2} \gamma_\mu (1 - \gamma^5) \begin{pmatrix} e \\ \mu \\ \tau \end{pmatrix}, \tag{1.6}$$

where the γ_μ are the usual Dirac matrices and $\gamma^5 = i\,\gamma_0\,\gamma_1\,\gamma_2\,\gamma_3$.

The formulation of this current expresses the empirical fact that leptons only couple within their own generation. In the case of the quarks, on the other hand, inter-generational couplings are observed, e.g. $\Lambda \rightarrow p\pi^-$ decay, where an s quark from the second generation gives rise to a u quark of the first generation. The theory handles this experimental fact by making the weak eigenstates of quarks different from the mass eigenstates. By convention, the u, c, and t quarks are unmixed, while the weak eigenstates of the d, s, and b quarks are given by linear combinations of their mass eigenstates. The weak charged current involving quarks is therefore given by;

$$J_\mu^+ = (\overline{u}, \overline{c}, \overline{t}) \frac{1}{2} \gamma_\mu (1 - \gamma^5) \begin{pmatrix} d' \\ s' \\ b' \end{pmatrix}, \tag{1.7}$$

with the primed quarks being related to their physical counterparts by the Cabibbo-Kobayashi-Maskawa (CKM) matrix [8] given by;

$$\begin{pmatrix} d' \\ s' \\ b' \end{pmatrix} = \begin{pmatrix} V_{ud} & V_{us} & V_{ub} \\ V_{cd} & V_{cs} & V_{cb} \\ V_{td} & V_{ts} & V_{tb} \end{pmatrix} \begin{pmatrix} d \\ s \\ b \end{pmatrix}.$$

One possible parametrization of the CKM matrix, which is supposed to be a unitary matrix, is via three angles and a phase [5] as given below;

$$\begin{pmatrix} c_{12}c_{13} & s_{12}c_{13} & s_{13}e^{-i\delta_{13}} \\ -s_{12}c_{23} - c_{12}s_{23}s_{13}e^{i\delta_{13}} & c_{12}c_{23} - s_{12}s_{23}s_{13}e^{i\delta_{13}} & s_{23}c_{13} \\ s_{12}s_{23} - c_{12}c_{23}s_{13}e^{i\delta_{13}} & -c_{12}s_{23} - s_{12}c_{23}s_{13}e^{i\delta_{13}} & c_{23}c_{13} \end{pmatrix},$$

with $c_{ij} = cos\theta_{ij}$, $s_{ij} = sin\theta_{ij}$, and i, j denoting the quark generations. When combined with experimental data, the unitarity constraint yields the following 90% confidence limits on the magnitude of the CKM matrix elements [5];

$$\begin{pmatrix} 0.9747 \text{ to } 0.9759 & 0.218 \text{ to } 0.224 & 0.002 \text{ to } 0.007 \\ 0.218 \text{ to } 0.224 & 0.9735 \text{ to } 0.9751 & 0.032 \text{ to } 0.054 \\ 0.003 \text{ to } 0.018 & 0.030 \text{ to } 0.054 & 0.9985 \text{ to } 0.9995 \end{pmatrix}.$$

The fact that the diagonal elements are close to unity reflects the experimental observation that quarks preferably couple within their own generation. Such decays are called Cabibbo favored decays. Cross-generational decays are called Cabibbo suppressed decays.

There is yet another symmetry between leptons and quarks under this theoretical frame. For all fermions, inter-generational transitions involve $W^{\pm}$, never γ or Z^0. In the case of the leptons, this mechanism explains the observed conservation of lepton family number. For quarks, it explains the nonexistence of the flavor changing neutral current (FCNC) at the tree-level. In fact, following this line of argument, Glashow, Iliopoulos and Maiani, proposed the GIM mechanism [9] in 1970 and predicted the existence of the charm quark. In the limit of no mixing with the third generation, $\theta_{13} = \theta_{23} = 0$, the CKM matrix reduces to the original Cabibbo matrix for four flavors;

$$\begin{pmatrix} cos\theta_c & sin\theta_c \\ -sin\theta_c & cos\theta_c \end{pmatrix} \tag{1.8}$$

where the angle $\theta_{12} = \theta_c$ is the Cabibbo angle and has been measured to be $\approx 13°$. It was observed that all neutral processes were characterized by the selection rule $\Delta S = 0$; in other words no neutral-current processes which involved change of strangeness were observed. For example, decays such as $K^0 \rightarrow \mu^+\mu^-$ are highly suppressed ($\sim 10^{-8}$) relative to corresponding charged current processes such as $K^0 \rightarrow \pi^+\pi^-$. The weak neutral current involving quarks of first generation only is given by;

$$J^0_\mu = (\overline{u}, \overline{d}') \frac{1}{2} \gamma_\mu (1 - \gamma^5) \begin{pmatrix} u \\ d' \end{pmatrix}$$

Ignoring the factors $\gamma_\mu (1 - \gamma^5)$ we can write

$$\begin{aligned} J^0_\mu &= \overline{u}u - \overline{d}'d' \\ &= \overline{u}u - \overline{d}dcos^2\theta_c - \overline{s}ssin^2\theta_c \\ &\quad -(\overline{s}d + s\overline{d})sin\theta_c cos\theta_c \end{aligned}$$

where the first three terms correspond to $\Delta S = 0$, and the last term corresponds to $\Delta S = 1$. After adding a new charm quark the neutral current modifies to;

$$\begin{aligned} J^0_\mu &= \overline{u}u - \overline{d}'d' + \overline{c}c - \overline{s}'s' \\ &= \overline{u}u + \overline{c}c - (\overline{d}d + \overline{s}s)cos^2\theta_c - (\overline{d}d + \overline{s}s)sin^2\theta_c \\ &\quad +(\overline{s}d + s\overline{d} - \overline{s}d - s\overline{d})sin\theta_c cos\theta_c \end{aligned}$$

The strangeness changing neutral current gets completely cancelled out at the tree level. This predicted c quark was discovered in November 1974, mentioned earlier as November Revolution, which in the particle physics community, refers to the discovery of J/ψ resonance by B. Richter's group [10] at SLAC and independently by S. Ting's group [11] at BNL. It was interpreted as a $c\overline{c}$ bound state.

The value of the Weinberg angle θ_w is related to the ratio of W and Z^0 boson masses. Its value was determined from experiment to be;

$$\theta_w = \frac{M_W}{M_Z} \approx 28.4^\circ \qquad (\, sin^2\theta_w \approx 0.226\,).$$

The derivation of this angle stands as a major challenge for any theory going beyond the Standard Model. Furthermore, the Higgs boson has not yet been confirmed by experiment. Nevertheless, the SM has been extremely successful in describing particle decays. Also, the discovery of the $W^{\pm}$ particles with $M_W \approx 80$ GeV/c^2 and the Z^0 with $M_Z \approx 91$ GeV/c^2 at CERN in 1983 [12] was taken as a persuasive evidence for the GWS theory.

1.3.4 Quantum Chromodynamics

The currently accepted theory of interacting quarks is Quantum Chromodynamics in which colored quarks interact via the exchange of gluons. Like the photon in QED, the gluons are massless and at short distance the QCD potential has the form of the QED Coulomb-like potential (interaction);

$$V(r)_{QED} = -\frac{\alpha_e}{r} \tag{1.9}$$

$$V(r)_{QCD} \approx -\frac{\alpha_s}{r} \qquad \text{as } r \rightarrow 0 \tag{1.10}$$

where α_s is the strong coupling constant. To be more explicit, we can write the actual form of $V(r)$ for short distances ($\leq 1fm$) as

$$V(r)_{QCD} = -\frac{4}{3}\frac{\alpha_{s(r)}}{r} \tag{1.11}$$

for a $q\bar{q}$ meson color singlet and

$$V(r)_{QCD} = -\frac{2}{3}\frac{\alpha_{s(r)}}{r} \tag{1.12}$$

for a qqq baryon color singlet. The factor of 4/3 for mesons and 2/3 for baryons comes from the group theory of SU(3). At long distances, i.e. $> 1fm$, $V(r)$ becomes a linear relation by Gauss's law, given as;

$$V(r) = \sigma r \qquad \text{as } r \rightarrow \infty \tag{1.13}$$

where σ is a force constant with a value of 0.7 - 1.0 GeV/fm. So for baryons the combined $V(r)$ at any distance is

$$V(r)_{QCD} = -\frac{2}{3}\frac{\alpha_{s(r)}}{r} + \sigma r. \tag{1.14}$$

While Coulomb-like interaction dominates at small values of r, the linear term dominates at larger values of r and is responsible for the confinement of quarks. Thus an infinite amount of energy would be required to separate the quarks to an arbitrarily large distance. This theory of the strong interaction, (QCD) [4], is analogous to the quantum theory of electromagnetic interaction (QED), but there is however, a significant qualitative difference between the two. In QCD, the bosons that transmit the force (the gluons) carry the quantity that they couple to, the strong charge. Here we say that the *Gluons have strong charge.* In QED, the boson that transmits the force (the photon) does not carry the quantity that it couples to, the electric charge. Here we say *Photons have zero electric charge*, a consequence of this is that photons do not couple directly to photons, while gluons do couple directly to gluons. There is also a quantitative difference in the strengths of the electromagnetic and strong interactions. The value of the dimensionless strong coupling (α_s) in the present range of experiments is much larger than the electromagnetic coupling (α_e). Perturbation theory, the technique of calculating interaction probabilities in powers of the dimensionless coupling, is more difficult in QCD and very often not possible. All hadrons have a net strong charge (color) of zero, and their net quark content

has zero strong charge even though the quark content of the hadron is continuously changing. The hadrons are color singlets as described in earlier sections, analogous to a spin singlet (a combination of $s = 1/2$ particles with zero net spin). In QCD, there are simple zero-color combinations of a hadron: (a) quark-antiquark, (b) three quarks, or (c) three antiquarks.

One central feature of QCD that has been verified by experiment is the property of *asymptotic freedom*. Asymptotic freedom refers to the fact that while quarks are permanently bound into hadrons, at shorter and shorter distances they do behave more and more as free particles. The concept of asymptotic freedom was realized theoretically in 1973 by H. David Politzer and independently by David Gross and Frank Wilczek. The strength of the interaction α_s changes quite rapidly with the wavelength of the quark at distances near $1fm$. In terms of the equivalent quark energy ($E = hc/\lambda$), we have $\alpha_s \approx 1$ at $E = 1$ GeV, and $\alpha_s \approx 0.1$ at $E = 100$ GeV. Thus, α_s is often referred to as *the running constant*. This property is called the asymptotic freedom: the fundamental parameter that specifies the quark-quark coupling strength decreases at shorter distances, since the quarks are free of the linear portion of the potential as stated in Eq. 1.13 and so the closer they are, the weaker the strong interaction between them. The qualitative reason for this is that at shorter distances, the gluon cloud surrounding the quark is penetrated. The gluons carry strong charge so that the effective strong charge of a quark is reduced at shorter distances. The variation of the strong coupling with energy is quantitatively determined in QCD. The value of α_s at a given energy depends on the number of quark flavors (n_f) that can participate in the binding process through their coupling to gluons. At energies much greater than the mass energies of the quarks, all flavors of quarks participate. In specifying the theoretical energy dependence of α_s, there

remains one fundamental constant that can be determined only from experiment. The definition of this constant is arbitrary, but conventionally a constant (Λ_{QCD}) that has dimensions of energy, is used. The constant Λ_{QCD} then defines a boundary in energy, below which we have hadrons and above which we have quarks. The order-of-magnitude of Λ_{QCD} is the mass energy of the lightest hadron, the pion. In terms of Λ_{QCD} and the number of quark flavors (n_f), the energy dependence of the strong coupling parameter is;

$$\alpha_s \approx \frac{12\pi}{(32 - 2n_f) ln\left(\frac{E^2}{\Lambda^2_{QCD}}\right)} \tag{1.15}$$

to lowest order in the energy E. From a variety of experiments [5], it is determined to be;

$$\Lambda_{QCD} \approx 200\ MeV \tag{1.16}$$

1.4 Particle Interactions

The basic physical quantities for any interaction are

- Decay rates (for decaying particles)
- Scattering cross-sections (for scattered particles)

In both cases there are two basic ingredients in the recipe, amplitude $\mathcal{M}$ for the process and the phase space available.

The Amplitude contains all the dynamical information and is calculated using Feynman diagrams. Phase space contains all the kinematical information and depends on masses, energies and momenta of the particles. The transition rate for any

given process is determined by Fermi's Golden Rule;

$$Transition\ Rate = \frac{2\pi}{\hbar} \mid M \mid^2 \times Phase\ Space \tag{1.17}$$

The decay rate for a process $1 \rightarrow 2+3+4\cdots n$ is given by;

$$\begin{aligned} d\Gamma &= \mid M \mid^2 \frac{S}{2\hbar m_1}\left[\left(\frac{cd^3\overline{p}_2}{(2\pi^3)2E_2}\right)\left(\frac{cd^3\overline{p}_3}{(2\pi^3)2E_3}\right)\cdots\left(\frac{cd^3\overline{p}_n}{(2\pi^3)2E_n}\right)\right] \\ &\times(2\pi)^4\delta^4(p_1-p_2-p_3\cdots p_n) \end{aligned}$$

where $p_i = \left(\frac{E_i}{c}, p_i\right)$ is the four momentum of ith particle with mass m_i and S is a product of statistical factor: $\frac{1}{j!}$ for each group of j identical particles.

The scattering Cross-section for a process $1+2 \rightarrow 3+4\cdots n$ is given by;

$$\begin{aligned} d\sigma &= \mid M \mid^2 \frac{\hbar^2 S}{4\sqrt{(p_1.p_2)^2-(m_1m_2c^2)^2}}\left[\left(\frac{cd^3\overline{p}_2}{(2\pi^3)2E_2}\right)\left(\frac{cd^3\overline{p}_3}{(2\pi^3)2E_3}\right)\cdots\left(\frac{cd^3\overline{p}_n}{(2\pi^3)2E_n}\right)\right] \\ &\times(2\pi)^4\delta^4(p_1-p_2--p_3\cdots p_n) \end{aligned}$$

Except for the electrons, protons, photons and neutrinos, all known particles [5] are unstable, and decay to lighter particles. The life span of an unstable particle is governed by statistics. For a group of a particular kind of particles, we have

$$N = N_0 e^{-t/\tau_0} \tag{1.18}$$

where N_0 is the number of particles at time $t = 0$ and N is the number of particles remaining after a time period t. The quantity τ_0 is the average lifetime of the particle. The lifetime of a particle is related to its observed natural width;

$$\Gamma_{Total} = \frac{1}{\tau_0} \tag{1.19}$$

This total width is the sum of the particle width for decay into all possible channels: from an initial state, i, to final states, $f_1, f_2, \ldots f_n, \ldots$, that is,

$$\Gamma_{Total} = \Gamma_{i\rightarrow f_1} + \Gamma_{i\rightarrow f_2} + \cdots + \Gamma_{i\rightarrow f_n} + \cdots \tag{1.20}$$

where f_i represents a specific decay mode. The branching fraction of a decay process leading to a specific final state, i $\rightarrow$ f, is defined as;

$$\mathcal{B}(i \rightarrow f) = \frac{\Gamma_{i \rightarrow f}}{\Gamma_{Total}}. \tag{1.21}$$

The described interactions (their perturbative expansion in terms of coupling constants) and the corresponding particle decay mechanisms can be concisely represented through Feynman diagrams. Fig. 1.2 shows the principal verteces of a fermionic constituent interacting with each of the gauge fields. Of course, any interaction of a pair of fermionic constituents with each other (or of any one with itself) must be described by at least two of those verteces. In the Feynman diagrams that appear in the following sections, the pervasive strong interaction between the quarks (and/or antiquarks) is often not drawn explicitly, but their association in strongly bound states is indicated through brackets.

1.5 Physics at PEP-II - e^+e^- Asymmetric Collider

At an asymmetric e^+e^- collider like PEP-II the bunches of high-energy electrons (9.0 GeV) are brought into collision with low-energy positrons (3.1 GeV). This operates at a high luminosity which is of the order $10^{33}\,\mathrm{cm}^{-2}\mathrm{s}^{-1}$, and the total center-of-mass energy is; E_{cm}=10.58 GeV/c, corresponding to the mass of the $\Upsilon(4S)$ resonance. Since electron and positron energies are not equal, therefore the center-of-mass frame is boosted in the laboratory frame, resulting in B mesons with significant momenta in the laboratory frame (the small Q-value of the $\Upsilon(4S) \rightarrow B\overline{B}$ decay results in B mesons almost at rest in the center-of-mass frame). This enables the measurement of the difference in decay time from the two B's. Also, the high luminosities provide enough B mesons, which is important in order to measure the

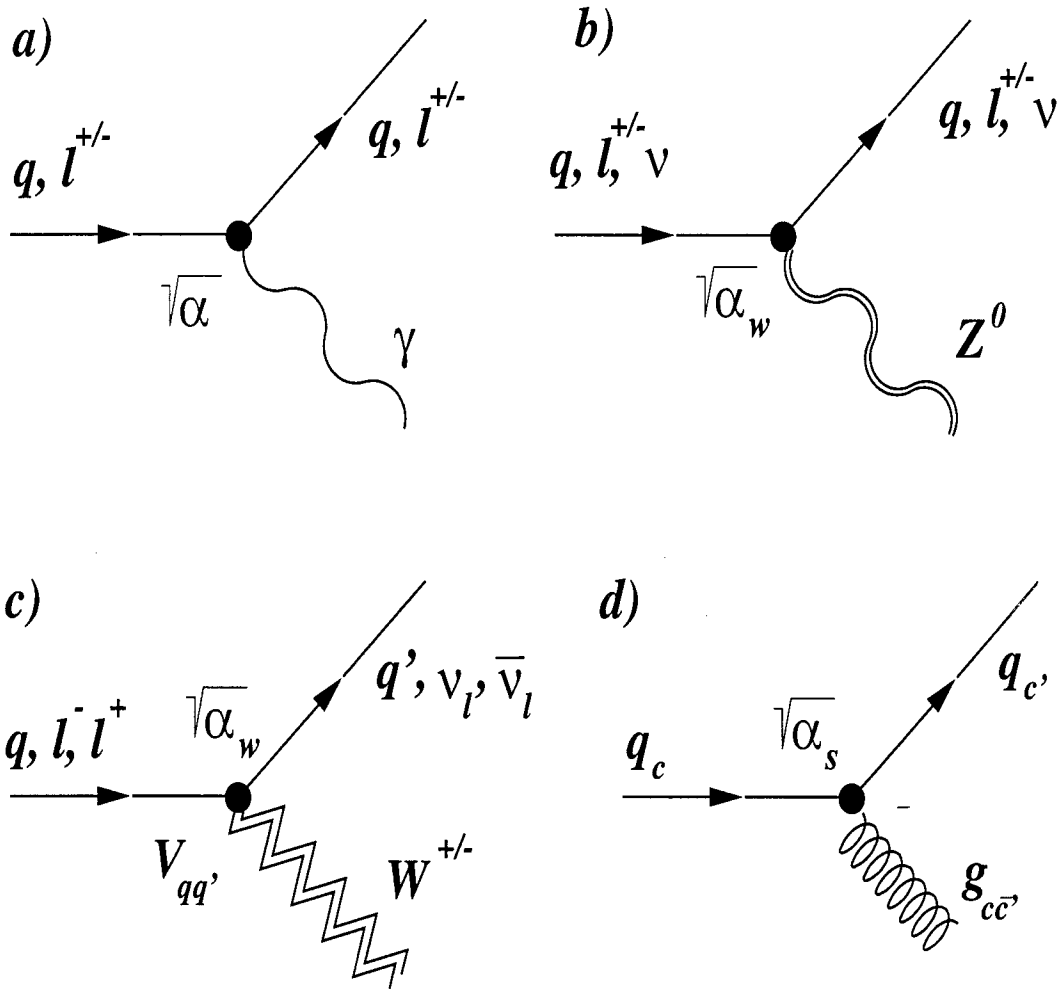

Figure 1.2: *The Interaction Vertices of the Standard Model:*
a) Electromagnetic, b) Weak Neutral, c) Weak Charged, d) Strong [4].

direct CP violation. Besides the CP violation, the other interesting phenomena which can be studied at the high luminosity collider, are the production mechanism of charmed baryons.

In an e^+e^- collider, a certain fraction of electron positron pairs annihilate to produce a virtual photon which then fragments into a pair of fermions. According to the Standard Model, the most elementary processes resulting from e^+e^- collisions are;

1. $e^+e^- \rightarrow (\gamma^*, Z) \rightarrow l^+l^- \qquad (l = e, \mu, \tau)$

2. $e^+e^- \rightarrow (\gamma^*, Z) \rightarrow \gamma\gamma$

3. $e^+e^- \rightarrow (\gamma^*, Z) \rightarrow q\bar{q} \qquad (q = u, d, s, c, b, t)$

For PEP-II since $\frac{E_{cm}}{c^2} < M_{Z^0}$, the Z^0 contribution is negligible; thus e^+e^- collisions are well described by Quantum Electrodynamics (QED), where an e^+e^- pair couples to a virtual photon, which then decays into a pair of fermions, creating quantum states having the quantum number of the photon ($J^{PC} = 1^{--}$). The final state must have the same quantum numbers as those of the photon ($J^{PC} = 1^{--}$). The general differential cross-section for fermion pair production for point-like spin 1/2 fermions (e.g. quarks) through single photon annihilation to first order is the given by;

$$\frac{d\sigma}{d\Omega}(e^+e^- \rightarrow f\overline{f}) = \frac{\alpha^2}{4s}\beta\left[1 + cos^2\theta + (1-\beta^2)sin^2\theta\right]Q_f^2 \qquad (1.22)$$

where the charge of the electron $e_e = \sqrt{\alpha}$ (hence $e_e^2 = \alpha$) is implicit, and $s = E^2 = E_{beam}^2$ or $4(pc)^2$, E_{beam} being the beam energy and E being the center-of-mass (c.m) energy. $\beta = v/c$ parameterizes the velocity of the final state fermions in the c.m frame relative to the speed of light; and Q_f is the charge of the fermion

$f = e, \mu, \tau, d, u, s, c, b, t$ in units of the electron charge, e. If the mass of the product fermions is negligible, and β approaches 1, then Eq. 1.22 becomes the familiar

$$\frac{d\sigma}{d\Omega}(e^+e^- \rightarrow f\overline{f}) = \frac{\alpha^2}{4s}\left[1 + cos^2\theta\right] Q_f^2 \tag{1.23}$$

By integrating over Ω and assuming $\beta \rightarrow 1$ (which is a good assumption for PEP-II energies), we arrive at;

$$\sigma(e^+e^- \rightarrow f\overline{f}) = \frac{4\pi\alpha^2}{3s}Q_f^2 = \frac{86.7\text{nb (GeV}^2)}{s}Q_f^2 = \sigma_{pt}Q_f^2 \tag{1.24}$$

where σ_{pt} is often called the "point" cross section. To arrive at the total hadronic cross-section, we have to sum over flavors and colors of the quarks,

$$\sigma(e^+e^- \rightarrow \text{hadrons}) = \frac{4\pi\alpha^2}{3s}\sum_{colors}\sum_{flavors} Q_f^2 = \sigma_{pt}\sum_{colors}\sum_{flavors} Q_f^2 \tag{1.25}$$

The color summation results in a factor of 3. It is conventional to relate the cross-section of $e^+e^- \rightarrow$ hadrons to that of $e^+e^- \rightarrow \mu^+\mu^-$. Then the ratio of hadronic to leptonic cross-section is,

$$R \equiv \frac{\sigma(e^+e^- \rightarrow \text{hadrons})}{\sigma(e^+e^- \rightarrow \mu^+\mu^-)} = 3\sum_{N_f=1}^{N_f=6} Q_f^2 \tag{1.26}$$

For PEP-II energies at $\Upsilon(4S)$ we have,

$$R = 3\left[2\left(\frac{2}{3}\right)^2 + 2\left(\frac{1}{3}\right)^2 + \left(\frac{1}{3}\right)^2\right] = \frac{11}{3} = 3.66 \qquad (\mathrm{N_f} = 5 : \mathrm{u, d, s, c, b})$$

and below $b\overline{b}$ threshold, we have,

$$R = 3\left[2\left(\frac{2}{3}\right)^2 + 2\left(\frac{1}{3}\right)^2\right] = \frac{10}{3} = 3.33 \qquad (\mathrm{N_f} = 4 : \mathrm{u, d, s, c})$$

Here it is important to mention that R is actually the ratio of the hadronic cross-section to the muon cross pairs when the radiation of the gluons by q and $\overline{q}$ is ignored. So, some corrections are needed to be able to compare with quantitative measurements. The hadronic cross-section at different energies for CLEO is shown in Fig. 1.3.

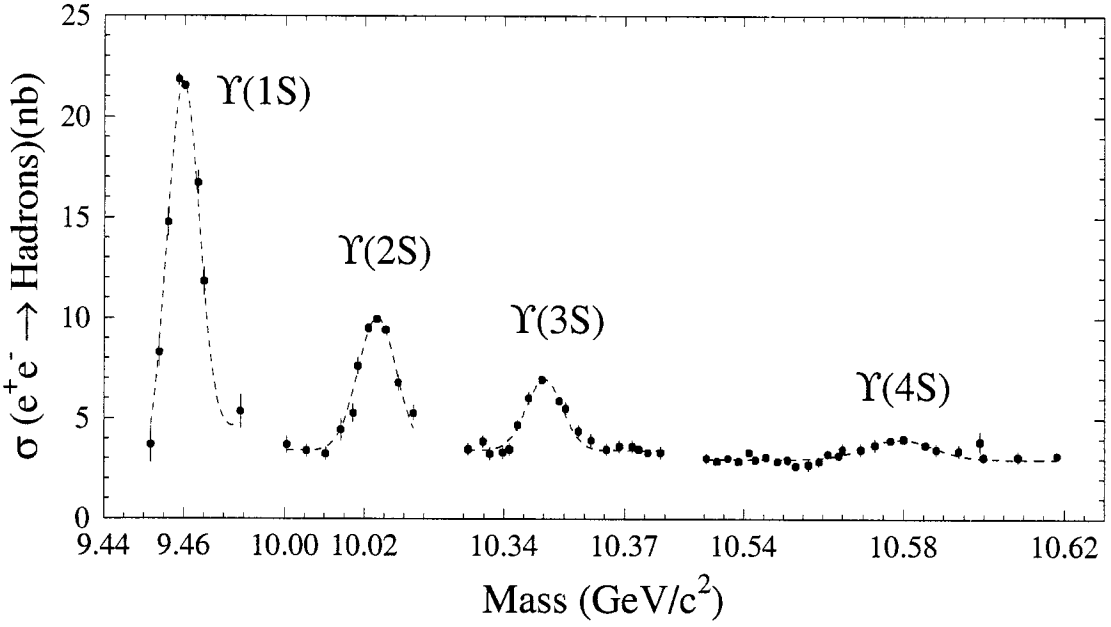

Figure 1.3: *The four* Υ *resonances, as observed at CESR.*

1.5.1 $e^+e^- \rightarrow B\overline{B}$

When the center-of-mass energy is near the threshold for a new flavor, a new vector meson is produced. In case of beauty or bottom $b\bar{b}$ pairs can be produced and form bound states, like $\Upsilon(1S)$, $\Upsilon(2S)$, and $\Upsilon(3S)$ resonance. At even higher energies excited $b\bar{b}$ bound states like $\Upsilon(4S)$ are formed, leading to the production of $B\overline{B}$ mesons. The production cross sections for these resonances is shown in Fig. 1.3 as a function of energy.

In 1977, a narrow resonance was found by Leon Lederman's group in a $\mu^+\mu^-$ (dimuon) invariant mass spectrum in a pN scattering (collision of 400 GeV protons on a Beryllium target) experiment at Fermilab [13]. They had observed a high yield of muon pairs at invariant masses of 9.44 GeV/c^2, which at the time was named Υ (now called $\Upsilon(1S)$). It was immediately interpreted as $b\bar{b}$ bound (bottomonium)

state of yet another new generation of heavy quark, called beauty or bottom, denoted as b. Soon thereafter, in early 1978, the PLUTO and DASP experiments at the DORIS e^+e^- storage ring at DESY verified the discovery of the Υ [14], by showing a sharp peak in the reaction $e^+e^- \rightarrow$ hadrons, at the same mass. In Figs. 1.4 (a) through (c), we show the possible mechanisms through which the $\Upsilon(1S)$, $\Upsilon(2S)$, and $\Upsilon(3S)$ resonances can decay. The mass of the $\Upsilon(4S)$ (10.58 GeV/c^2) is high enough so that a second pair of light quarks can be produced from the vacuum such that $\Upsilon(4S)$ decays via strong interaction. Fig. 1.4 (d) shows how B mesons are formed from the $\Upsilon(4S)$ resonance, via popping off a light quark-antiquark pair ($q = u, d$). The $\Upsilon(4S)$ bound state disintegrates and either a $u\overline{u}$ or a $d\overline{d}$ pair is created from the vacuum to form a B and a $\overline{B}$ mesons, each of mass $\sim$ 5.279 GeV/c^2. The availability of this decay channel makes the $\Upsilon(4S)$ significantly broader than the first three Υ resonances, whose widths are consistent with the storage ring energy spread. Their narrow widths are explained by the empirical Okubo-Zweig-Iizuka (OZI) rule [15] which states that, if in a particle decay all the energy is transferred via gluons ("hard gluons"), then the decay is heavily suppressed. Since Υ states have $J^{PC} = 1^{--}$, they can decay via ggg, $gg\gamma$, $\gamma\gamma\gamma$, or γ^*. Furthermore, each gluon exchange introduces a factor of strong coupling constant, $\sqrt{\alpha_s}$, in the decay amplitude and hence suppresses the annihilation amplitude. Examples of this suppression can be seen in Fig. 1.4 (a) and (b). The electromagnetic annihilation process shown in Fig. 1.4 (c) is also suppressed compared to the $\Upsilon(4S) \rightarrow B\overline{B}$ decay mode, but this is because of the different relative strengths of the involved interactions. The decay of B mesons can be described by five basic decay diagrams, shown in Fig. 1.5: (a) external spectator, (b) internal or color mixed spectator, (c) annihilation, (d) W-exchange, and (e) penguin processes. The external spectator

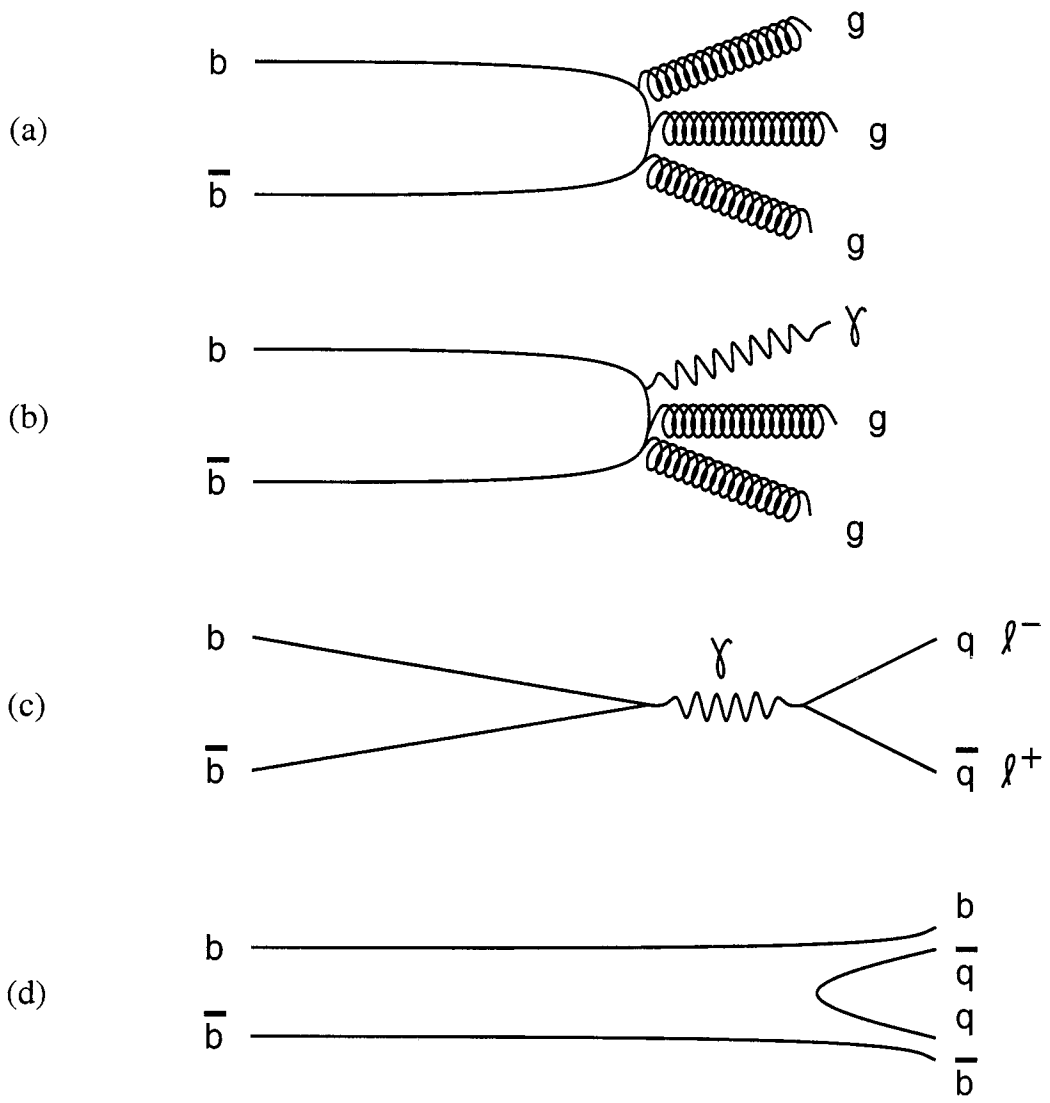

Figure 1.4: *Decay mechanisms of the* Υ *resonances; (a) through (c) show how the* $\Upsilon(1S)$ *through* $\Upsilon(3S)$ *resonances decay via annihilation of the b and* $\overline{b}$ *quarks, and (d) shows how B mesons are formed in* $\Upsilon(4S)$ *decay.*

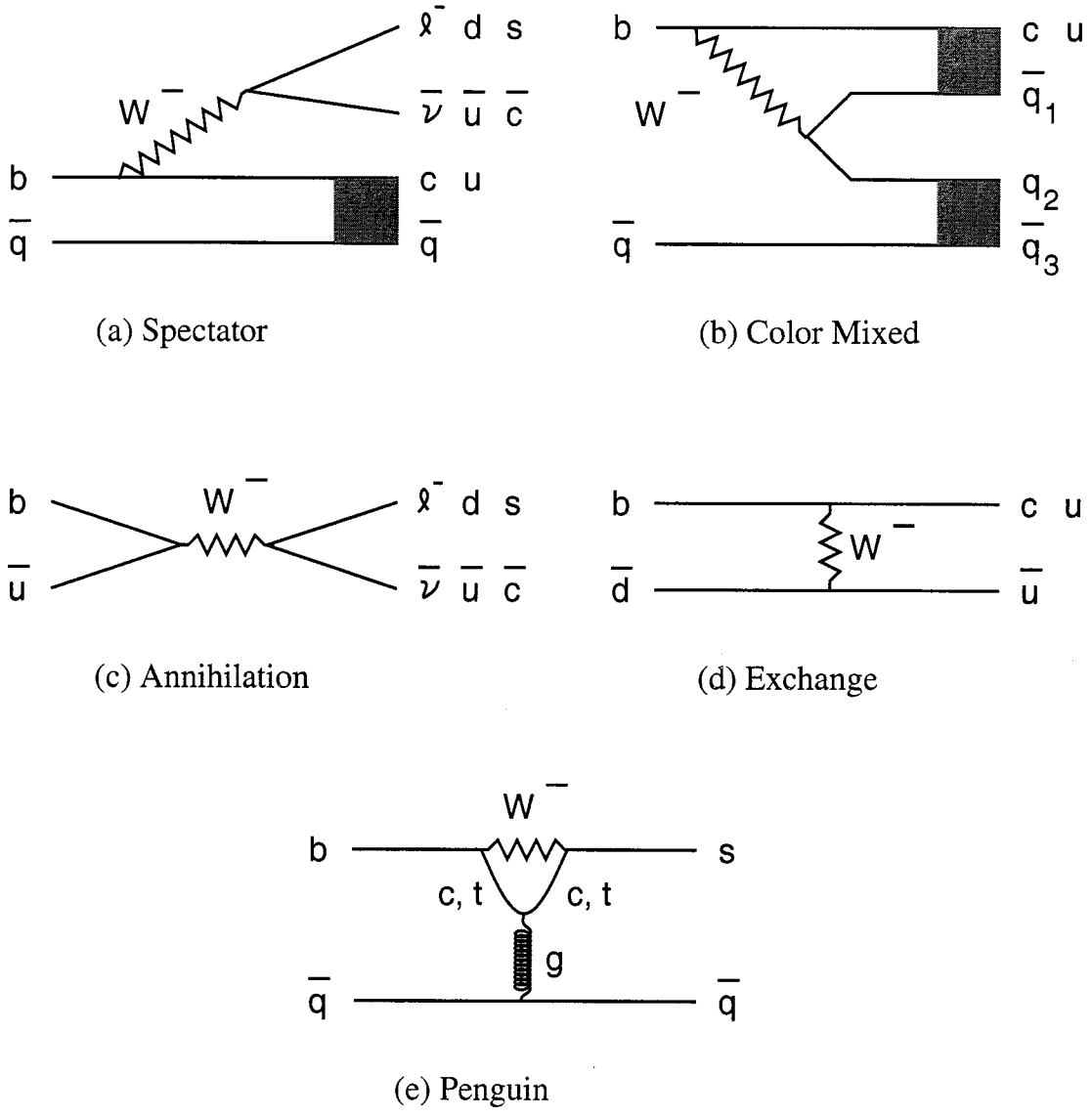

Figure 1.5: *Decay mechanisms of B mesons, shown in form of the quark level diagrams: (a) External W-emission ("spectator"), (b) Internal W-emission ("color mixed"), (c) Annihilation, (d) W-exchange, and (e) gluonic "Penguin."*

is the simplest process because the light quark does not participate in the weak decay process. One of the final state particles is produced by the W^-, whereas the other one is formed by the c (or u) quark and the light spectator. In the internal spectator (also called color mixed or color suppressed) diagram, the c and the spectator quarks combine with the quarks from the virtual W to form final state particles. It is suppressed because the color of the W-daughter quarks has to match with that of the c and the spectator quark, since the final states have to be colorless. One would therefore naively expect this decay to be suppressed by a factor of $1/N_c^2 = 9$, with N_c being the number of colors, but the suppression is mitigated by gluon exchange effects. W-annihilation and W-exchange processes are helicity suppressed, and W-annihilation is also color suppressed. Penguin processes are also heavily suppressed because of additional gluon exchanges between the heavy and the light quark.

1.5.2 $e^+e^- \rightarrow c\bar{c}$

At energies around the $\Upsilon(4S)$ resonance, e^+e^- annihilations can produce any of the four quark - anti-quark pairs shown below along with $b\bar{b}$;

$$e^+e^- \rightarrow u\bar{u},\ d\bar{d},\ s\bar{s},\ \text{and},\ c\bar{c}. \tag{1.27}$$

The $q\bar{q}$ pairs then hadronize, producing families of mesons and baryons. The hadronic cross-section for the $c\bar{c}$ production is 40% of the total cross-section, so that we get copious $c\bar{c}$ jets just below the $\Upsilon(4S)$ resonance. Fig. 1.6 represents possible ways of charmed meson and charm baryon production at *BABAR* at continuum. Most of the times a charmed baryon does not accompany the corresponding charmed anti-baryon, but does accompany some other anti-baryon to conserve baryon number. The decay mechanisms of charmed baryons, specific to this thesis, will be

discussed later in the third chapter.

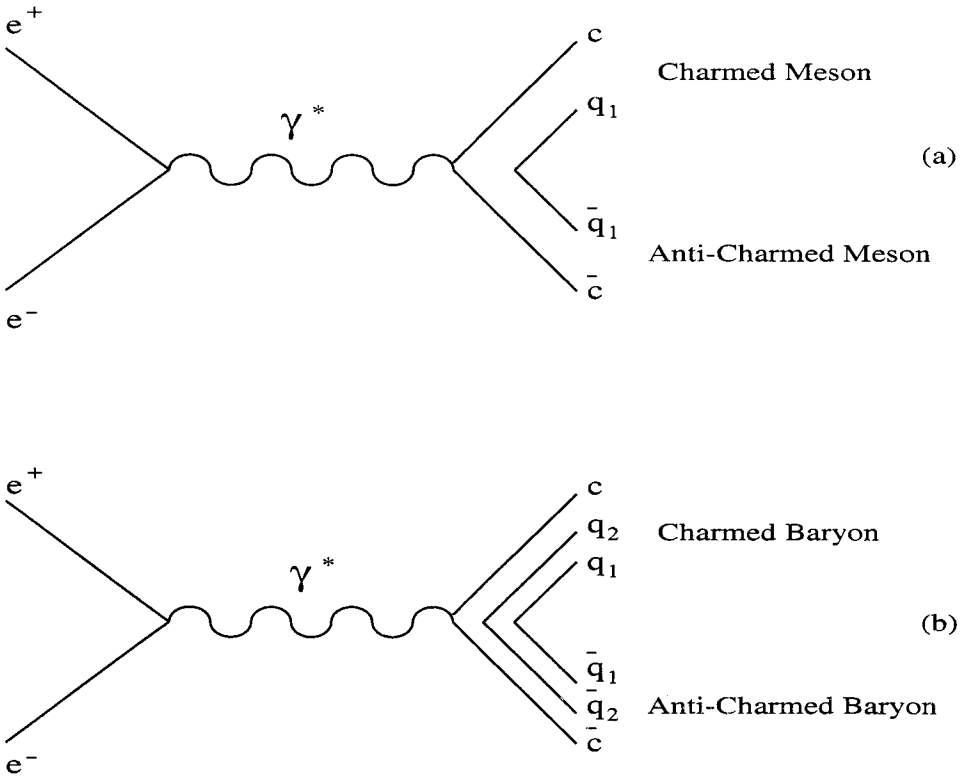

Figure 1.6: *A Feynman diagram of the (a) continuum charmed meson production route via* $e^+e^- \rightarrow c\bar{c} \rightarrow$ Charmed Mesons *and (b) continuum charmed baryon production route via* $e^+e^- \rightarrow c\bar{c} \rightarrow$ Charmed Baryons.

1.6 Invariant Mass of a Particle

Special relativity gives the relation between the energy, E, momentum p, and the mass M, of any subatomic particle as;

$$E^2 = p^2c^2 + M^2c^4 \tag{1.28}$$

where c is the speed of light. When the object is at rest, Eq. 1.28 becomes the famous relation $E = mc^2$. Since c is approximately the speed at which high energy

particles naturally travel, it is convenient to work with units in which $c = 1$. Thus simplifying to;

$$E^2 = p^2 + M^2 \tag{1.29}$$

Solving for M, we have,

$$M = \sqrt{E^2 - p^2} \tag{1.30}$$

Given the measurement of the momentum, p, and energy E, of a particle, we can calculate its *invariant mass* M. If a particle decays, its momentum and the energy are the sum of the momenta and the energies of its decay products. For i number of decay products, each having momentum p_i and energy ε_i the invariant mass can be written as;

$$M = \sqrt{\sum_i (\varepsilon_i)^2 - \sum_i (p_i)^2} \tag{1.31}$$

where

$$\sum_i (\varepsilon_i^2) = E^2 \tag{1.32}$$

and

$$\sum_i (p_i)^2 = p^2 \tag{1.33}$$

The invariant mass distribution is typically a peaked distribution, whose RMS width depends on the measurement resolution σ, while combinatoric background can almost always be described by a low order polynomial. Requiring that the invariant mass be within 2 - 3σ of the nominal mass is therefore, very effective in keeping most of the signal, while rejecting much of the background.

Chapter 2

Charmed Baryon Spectroscopy

The discovery of J/ψ, a narrow meson resonance of mass 3.1 GeV/c^2 [10, 11] in 1974, led the path to a new era of Charm Physics in heavy hadron physics. In the subsequent years, it was successfully interpreted as a bound state of the heavy charm quark and an anti-charm quark with mass, $m_c \sim 1500$ MeV/c^2 and charge, $\pm\frac{2}{3}$. This discovery opened a whole new sector of baryons and mesons carrying various amounts of charm. The first charmed baryon, the Λ_c^+(udc), was discovered in 1975, in a Bubble chamber experiment at BNL [16]. Soon others followed, and ever since, the field of charmed baryon spectroscopy has become one of the most sought after topics in particle physics. With the advent of new powerful accelerators, more charmed mesons and baryons were revealed, giving a big boost to the quark model and hence the spectroscopic study of charmed baryons and charmed mesons followed.

2.1 Quark Model

The newly discovered fourth flavor was assigned an additional quantum number "charm C" ($C = 1$), isospin $T = T_3 = 0$ and hypercharge $Y = \frac{4}{3}$. The c quark is a singlet under the SU(3) flavor symmetry. The group which incorporates all the four quarks u, d, s, c under one framework is the SU(4) group, while SU(3) remains a subgroup of the SU(4). Like SU(3), the fundamental representations of the SU(4) are, $[\mathbf{4}]$ for quarks and $[\overline{\mathbf{4}}]$ for anti-quarks.

The heavy hadrons composed of charm and bottom quarks are quite different from the light flavored hadrons composed of u, d, and s quarks. This behavior led to the notion of the Heavy Quark Effective Theory (HQET) [17]. In nature we have six quarks, grouped into *light* and *heavy* sectors. The *light* sector comprises u, d, and s quarks with masses less than the scale parameter $\Lambda_{QCD} \cong 400$ MeV, whereas the *heavy* sector comprises c, b, and t quarks with masses much greater than Λ_{QCD}. In the realm of HQET, the QCD Lagrangian is expanded in powers of $1/m_Q$ and the leading terms in the expansion can be interpreted using a concept, that the heavy quark at the center is being surrounded by the light quark cloud, and the light quark cloud interacts with the heavy center via gluons. Gluons neither have flavor nor can they distinguish between flavor, hence the light quarks, also known as *light degrees of freedom* (light quark and gluons), do not see the flavor of the heavy quark. The heavy nature of the charm or bottom quark at the center, decouples the spins of light quarks from the center. In the heavy quark mass limit, a bottom baryon at rest is identical to a charm baryon at rest. The different *light degrees of freedom*, all look the same, regardless of the flavor and the spin orientation of the heavy quark. Therefore, there are two heavy quark symmetries; one is the flavor symmetry and the

second is spin symmetry. Under the SU(4) flavor symmetry hadrons are classified as $\mathbf{4} \otimes \overline{\mathbf{4}}$ mesons ($q\bar{q}$) and $\mathbf{4} \otimes \mathbf{4} \otimes \mathbf{4}$ baryons (qqq).

In mesons we have two quarks, each with spin 1/2. From elementary quantum mechanics, the two spin half particles can have either spin 1, or spin 0 depending on whether the two quarks are aligned parallel or anti-parallel to each other, i.e.;

$$\mathbf{S} = \frac{1}{2} \otimes \frac{1}{2} = 1 \oplus 0,$$

whereas for baryons, the configuration of the three quarks are somewhat different,

$$\mathbf{S} = (\frac{1}{2} \otimes \frac{1}{2}) \otimes \frac{1}{2} = (0 \oplus 1) \otimes \frac{1}{2} = \frac{1}{2} \oplus \frac{3}{2}.$$

Angular momentum falls under the O(3) group. The hadrons can exist in orbital or radial (*e.g.*, $\chi_{b1}(1P)$, $\chi_{b1}(2P)$or $\Upsilon(3S), \Upsilon(4S)$) excitations [5]. Using a constituent quark model picture the underlying SU(4)⊗O(3) symmetry gives rise to a spectrum of charm mesons and charm baryons. The five quark flavors that are more or less stable (i.e. which at least hadronize before decaying) may form hundreds of different meson and baryon particle states which can be distinguished by their flavor content, the spin alignment of the constituent quarks, and the degree of their orbital or radial excitation. They can be classified in terms of the symmetries in which the quarks combine their flavor, spin, color and spatial states, such that the wavefunction of the resulting hadronic system satisfies appropriate symmetries itself. The wavefunction of a baryon is antisymmetric, changing sign under interchange of any two of its three fermionic quark constituents. The latter requirement significantly restricts the number of different baryons that may arise from quark constituents of given flavor. We will discuss the ground state charmed baryon spectroscopy with a brief introduction to charmed mesons.

2.2 Charmed Mesons

The SU(4) representation [**4**] (*u, d, s, c*) decomposes under SU(3) as the SU(3) triplet [**3**] (*u, d, s*) and the SU(3) singlet [**1**] (*c*). For mesons, we write [18],

$$[\mathbf{4}] \otimes [\overline{\mathbf{4}}] \rightarrow ([\mathbf{3}] \oplus [\mathbf{1}]^{1}) \otimes ([\overline{\mathbf{3}}] \oplus [\mathbf{1}]^{-1})$$

where,

[**3**] and [$\overline{\mathbf{3}}$] are the SU(3) triplets,

$[\mathbf{1}]^{1}$ is the SU(3) singlet with $C = 1$,

$[\mathbf{1}]^{-1}$ is the SU(3) singlet with C = -1.

Expanding to a group theoretic sum, one obtains;

$$[\mathbf{4}] \otimes [\overline{\mathbf{4}}] \rightarrow [\mathbf{8}]^{0} \oplus [\mathbf{1}]^{0} \oplus [\mathbf{3}]^{-1} \oplus [\overline{\mathbf{3}}]^{1} \oplus [\mathbf{1}]^{0}$$

where the superscript represents the charm content. The term $[\mathbf{8}]^{0}$ and $[\mathbf{1}]^{0}$ make up the SU(3) nonet, having K^0, $\overline{K^0}$, K^+, K^-, π^+, π^0, π^-, η and η'. The $[\mathbf{3}]^{-1}$ and $[\overline{\mathbf{3}}]^{1}$ come from the association of the charm quark with the SU(3) triplet representation, $[\mathbf{3}]^{-1}$ states are the D^0 ($c\overline{u}$), D_s^+ ($c\overline{s}$), D^+ ($c\overline{d}$) and $[\overline{\mathbf{3}}]^{1}$ states are the $\overline{D}^0$ ($u\overline{c}$), D_s^- ($s\overline{c}$), D^- ($d\overline{c}$) and the remaining $[\mathbf{1}]^{0}$ state is η_c. Apart from these mesons with *open charm*, there also exist mesons with *hidden charm*, η_c (paracharmonium spin = 0) and J/Ψ (orthocharmonium spin = 1) bound state of c and $\overline{c}$. For the diquark system the total spin angular momentum can have two possible values, spin 0 or spin 1 and they are classified as *pseudoscalar mesons* ($J^{PC} = 0^{-1}$) and *vector mesons* ($J^{PC} = 1^{-1}$), as shown in Fig. 2.1.

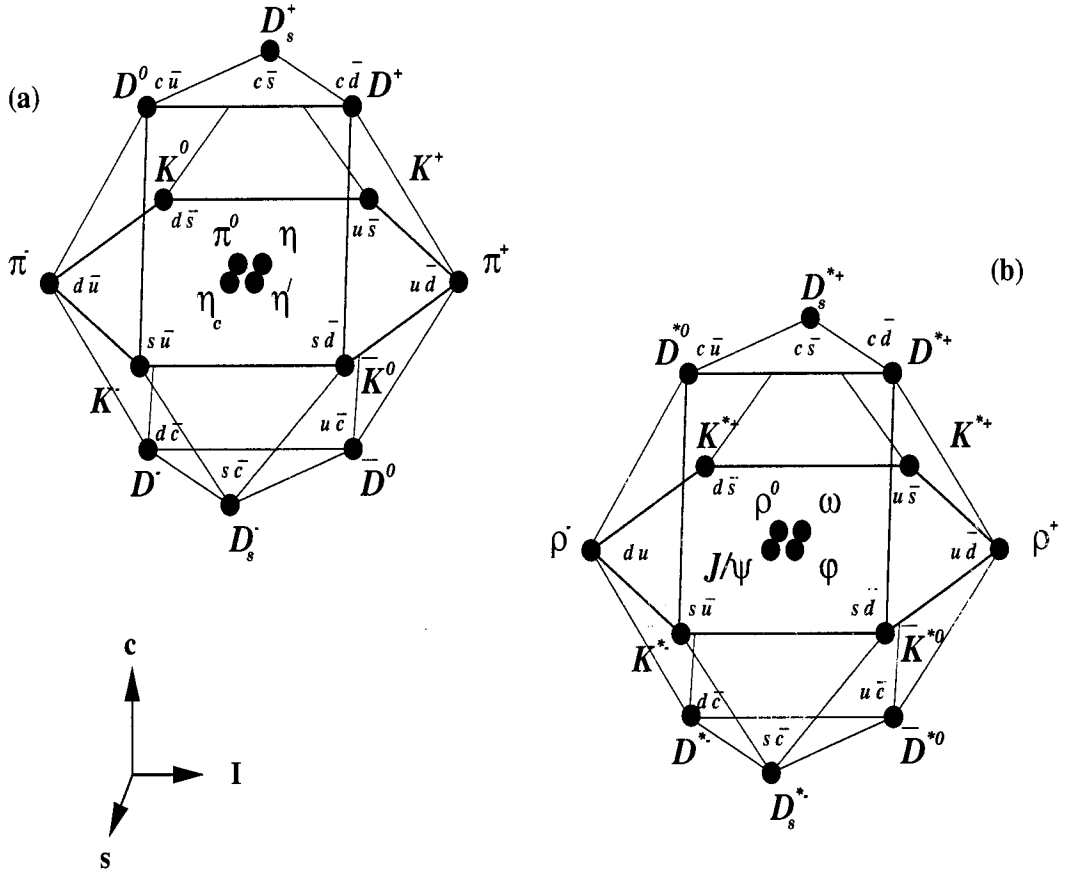

Figure 2.1: *SU(4) 16-plets for the (a) pseudoscalar and (b) vector mesons composed of u, d, s, and c quarks. The nonets of the light mesons occupy the central plane, to which $c\bar{c}$ states have been added. The neutral mesons at the centers of these planes are mixtures of $u\bar{u}$, $d\bar{d}$, $s\bar{s}$, and $c\bar{c}$ states [5].*

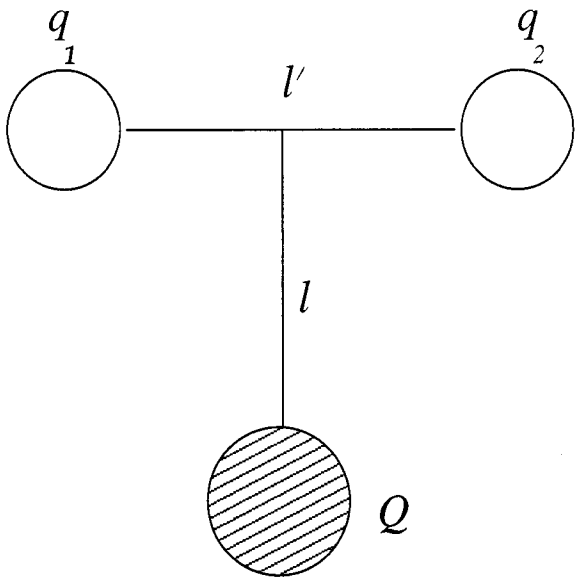

Figure 2.2: *Charmed baryon bound state structure.*

2.3 Charmed Baryons

According to the Heavy Quark Effective Theory (HQET) picture of the quark model, the baryons are the bound states Qqq formed from a heavy quark Q and a light diquark system as shown in Fig. 2.2. In case of singly-charmed baryons, the Q is replaced by a c quark.

The spin-parity quantum numbers j_l^P of the *light degrees of freedom* are determined from the spin and orbital degrees of freedom of the light quarks in the diquark system. The spin of the diquark can either be 0 or 1. The total orbital angular momentum is the sum of the two angular degrees of freedom l' and l, where l' describes the orbital excitations of the light quarks in the diquark system, and l is the orbital excitation of the light diquark relative to the central heavy quark. The light diquark system can have total angular momentum $j_l = 0, 1, 2...$ and parity $P = \pm 1$. Each combination of j_l^P diquark system, corresponds to a degenerate heavy baryon dou-

blet with $J^P = (j_l \pm \frac{1}{2})^P$. The only exception is $j_l = 0$, because when spin half of the charm quark couples with $j_l = 0$, it gives a singlet. In case of S-Wave or ground state, $l = 0$ and $l' = 0$. The P-Wave or excited state baryons, have either $l = 1$ and $l' = 0$ or $l = 0$ and $l' = 1$. With three spin half quarks, the total angular momentum of a baryon could be either 1/2 or 3/2 or 5/2.....

The total wavefunction of any hadron is a product of different independent components [19],

$$|\Psi\rangle = |\chi\rangle|\psi_F\rangle|\psi_C\rangle|\psi_L\rangle|\psi_R\rangle \tag{2.1}$$

where χ denotes the spin wavefunction, ψ_F represents the flavor part of the wavefunction, ψ_C represents the color part of the wavefunction, ψ_L denotes the angular part and ψ_R represents the radial part of the spatial wavefunction. The total wavefunction for fermions has to be anti-symmetric, following Pauli's Exclusion principle. In the case of baryons, the spin part $|\chi\rangle_{S,M_A,M_S}$ could be fully-symmetric or mixed-antisymmetric or mixed-antisymmetric. The flavor part $|\psi_F\rangle_{S,M_S,M_A,A}$, can be fully-symmetric or mixed-symmetric or mixed-antisymmetric or even fully-antisymmetric. As mentioned in the previous chapter, the color part $|\psi_C\rangle$ is always anti-symmetric. The angular part of the spatial wavefunction has a symmetry of $(-1)^{l'}$ or $(-1)^l$ so it can be symmetric or antisymmetric, depending on the baryon parity. For all ground state baryons, which have $l = l' = 0$, it is symmetric. The radial part $|\psi_R\rangle_S$, is generally symmetric under the interchange of quarks, because of the spherical symmetry.

2.3.1 S-Wave Baryons

Under the SU(4) symmetry of charmed baryons we can classify the various representations by expanding;

$$[\mathbf{4}] \otimes [\mathbf{4}] \otimes [\mathbf{4}] \rightarrow [\mathbf{20}]'_{\mathbf{S}} \oplus [\mathbf{20}]_{\mathbf{M_S}} \oplus [\mathbf{20}]_{\mathbf{M_A}} \oplus [\overline{\mathbf{4}}]_{\mathbf{A}}$$

Both the $[\mathbf{20}]_{\mathbf{M_S}}$ and $[\mathbf{20}]_{\mathbf{M_A}}$ representations are merged into one $[\mathbf{20}]_{\mathbf{M}}$ structure and both the $J^P = \frac{1}{2}^+$ baryons are represented in this $[\mathbf{20}]_{\mathbf{M}}$ structure. In the $[\mathbf{20}]'_{\mathbf{S}}$ structure are the $J^P = \frac{3}{2}^+$ baryons. The fully-antisymmetric $[\overline{\mathbf{4}}]_{\mathbf{A}}$ is not allowed in the S-Wave SU(4) representation, since there is no corresponding fully-antisymmetric baryon spin structure (recall that for baryon spin in SU(2): $[\mathbf{2}] \otimes [\mathbf{2}] \otimes [\mathbf{2}] \rightarrow [\mathbf{4}]_{\mathbf{S}} \oplus [\mathbf{2}]_{\mathbf{M_S}} \oplus [\mathbf{2}]_{\mathbf{M_A}}$). We can further decompose the two SU(4) representations and get

$$[\mathbf{20}]_{\mathbf{M}} \rightarrow \ [\mathbf{8}]^{\mathbf{0}} \oplus ([\overline{\mathbf{3}}]^{\mathbf{1}} \oplus [\mathbf{6}]^{\mathbf{1}}) \oplus [\mathbf{3}]^{\mathbf{2}}$$

$$[\mathbf{20}]'_{\mathbf{S}} \rightarrow [\mathbf{10}]^{*\mathbf{0}} \oplus [\mathbf{6}]^{*\mathbf{1}} \oplus [\mathbf{3}]^{*\mathbf{2}} \oplus [\mathbf{1}]^{*\mathbf{3}}$$

These representations are shown in Fig. 2.3. The two light quarks can form a diquark pair of $J^P = \{0^+\}$ (fully-antisymmetric with respect to the interchange of the diquark flavor and spin), or a $J^P = \{1^+\}$ (fully-symmetric with respect to the interchange of the diquark flavor and spin). The 0^+ diquark state can then combine with a $J^P = \frac{1}{2}^+$ third quark to form $J^P = \frac{1}{2}^+$. In case when the third quark is either a u or d, we have $[\mathbf{8}]^{\mathbf{0}}$ representation corresponding to the SU(3) octet, while in case of c-quark we have mixed-antisymmetric $[\overline{\mathbf{3}}]^{\mathbf{1}}$ representation corresponding to Λ_c^+, Ξ_c^+, and Ξ_c^0. Similarly, the 1^+ diquark state can combine with a $J^P = \frac{1}{2}^+$ third quark to form $J^P = \frac{1}{2}^+$ and $J^P = \frac{3}{2}^+$ states. In case when the third quark is either a u or d, we obtain a $[\mathbf{10}]^{*\mathbf{0}}$ representation corresponding to the SU(3) decuplet.

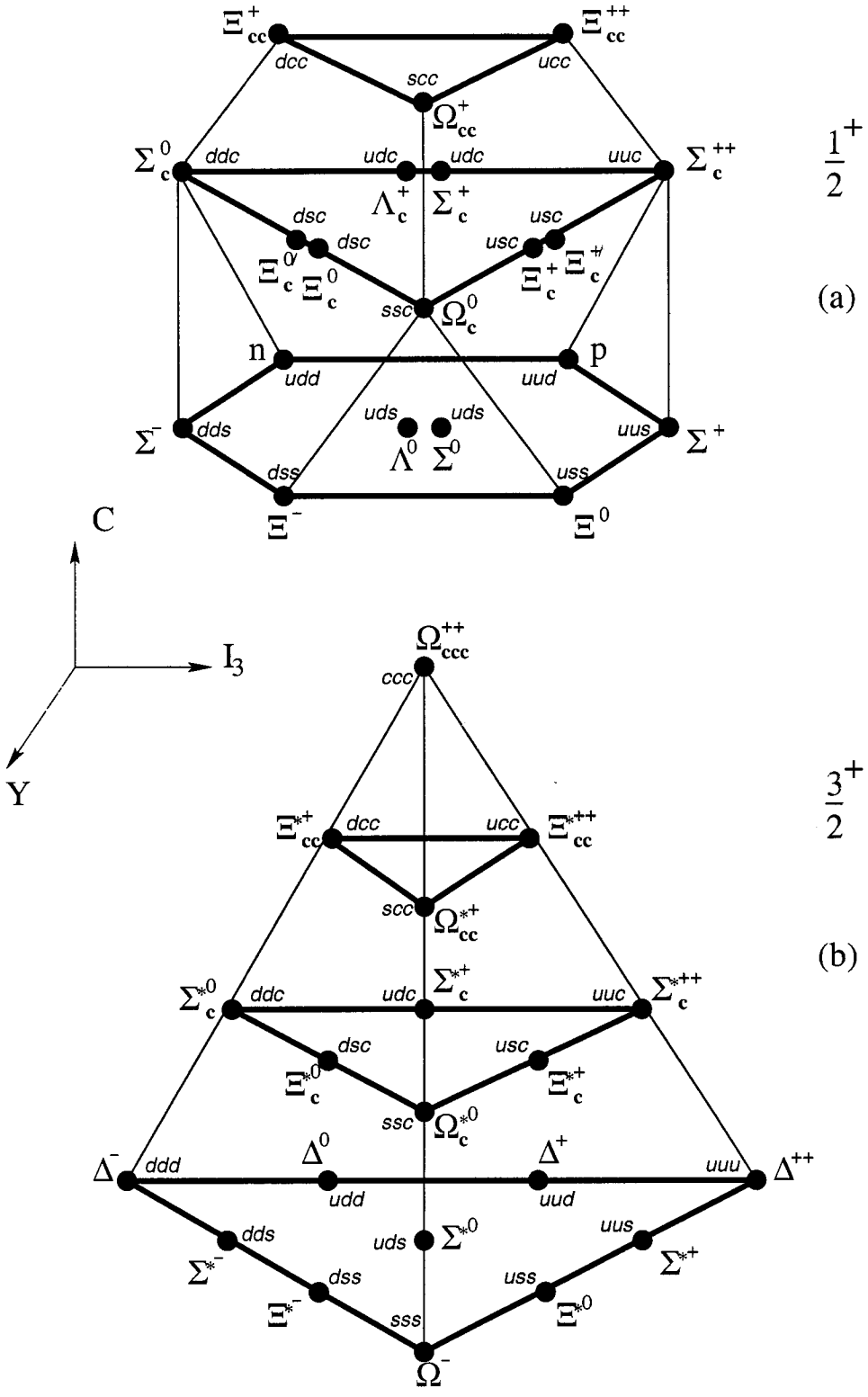

Figure 2.3: *Charmed baryon SU(4)* $J^P = \frac{1}{2}^+$ *and* $J^P = \frac{3}{2}^+$ *20-plets [5].*

For the case of c-quark we have two choices; firstly, it can form the $J^P = \frac{1}{2}^+$ mixed-symmetric $[\mathbf{6}]^1$ representation corresponding to Σ_c^+, Σ_c^0, Σ_c^{++}, $\Xi_c^{+\prime}$, $\Xi_c^{0\prime}$ and Ω_c^0. In the other case, it forms the $J^P = \frac{3}{2}^+$ fully-symmetric $[\mathbf{6}]^{*\mathbf{1}}$ representation corresponding to Σ_c^{*+}, Σ_c^{*0}, Σ_c^{*++}, Ξ_c^{*+}, Ξ_c^{*0}, and Ω_c^{*0} respectively. Altogether there are 15 ground state singly-charmed baryons.

The S-Wave doubly-charmed baryons can be formed by assuming a diquark (QQ), which can only form, $J^P = \{1^+\}$ (fully-symmetric under the interchange of flavor and spin for the two heavy charm quarks) and then adding a light q quark, in two ways; firstly, in one case it forms the $J^P = \frac{1}{2}^+$ mixed-symmetric $[\mathbf{3}]^{\mathbf{2}}$ representation corresponding to Ξ_{cc}^{++}, Ξ_{cc}^{+}, Ω_{cc}^{+} states. In the other case it forms the $J^P = \frac{3}{2}^+$ fully-symmetric $[\mathbf{3}]^{*\mathbf{2}}$ representation corresponding to Ξ_{cc}^{*++}, Ξ_{cc}^{*+}, and Ω_{cc}^{*+} states. Altogether there are 6 ground state doubly-charmed baryons.

The S-Wave triply-charmed baryons can be formed by assuming a $J^P = \{1^+\}$ (fully-symmetric under the interchange of any two charm quark flavor and spin) heavy diquark (QQ) and then adding the third Q quark, which then can only be in $J^P = \frac{3}{2}^+$ fully-symmetric $[\mathbf{1}]^{*\mathbf{3}}$ representation corresponding to the Ω_{ccc}^{++} state. Table 2.1 shows a full list of ground state $\frac{1}{2}^+$ and $\frac{3}{2}^+$ charmed baryons.

Table 2.1: A List of Ground-State $\frac{1}{2}^+$ and $\frac{3}{2}^+$ Charmed Baryons [5]

Notation	Quark Content	J^P	Flavor SU(3)	(I, I_z)	S	C	Observed Mass (MeV)
Λ_c^+	$c[ud]$	$\frac{1}{2}^+$	$\bar{3}$	(0,0)	0	1	2284.9±0.6
Ξ_c^+	$c[su]$	$\frac{1}{2}^+$	$\bar{3}$	(1/2,1/2)	-1	1	2468.0±0.4
Ξ_c^0	$c[sd]$	$\frac{1}{2}^+$	$\bar{3}$	(1/2,-1/2)	-1	1	2471.0±0.6
Σ_c^{++}	$c\{uu\}$	$\frac{1}{2}^+$	6	(1,1)	0	1	2452.5±0.6
Σ_c^+	$c\{ud\}$	$\frac{1}{2}^+$	6	(1,0)	0	1	2451.3±0.9
Σ_c^0	$c\{dd\}$	$\frac{1}{2}^+$	6	(1,-1)	0	1	2452.2±0.6
$\Xi_c^{+\prime}$	$c\{su\}$	$\frac{1}{2}^+$	6	(1/2,1/2)	-1	1	2575.8±3.1
$\Xi_c^{0\prime}$	$c\{sd\}$	$\frac{1}{2}^+$	6	(1/2,-1/2)	-1	1	2578.0±2.9
Ω_c^0	$c\{ss\}$	$\frac{1}{2}^+$	6	(0,0)	-2	1	2697.5±2.6
Ξ_{cc}^{++}	$c\{cu\}$	$\frac{1}{2}^+$	6	(1/2,1/2)	0	2	Not seen
Ξ_{cc}^+	$c\{cd\}$	$\frac{1}{2}^+$	6	(1/2,-1/2)	0	2	3519±1
Ω_{cc}^+	$c\{cs\}$	$\frac{1}{2}^+$	6	(0,0)	-1	2	Not seen

Notation	Quark Content	J^P	Flavor SU(3)	(I, I_z)	S	C	Observed Mass (MeV)
Σ_c^{*++}	$\{cuu\}$	$\frac{3}{2}^+$	6*	(1,1)	0	1	2519.4±1.5
Σ_c^{*+}	$\{cud\}$	$\frac{3}{2}^+$	6*	(1,0)	0	1	2515.9±2.4
Σ_c^{*0}	$\{cdd\}$	$\frac{3}{2}^+$	6*	(1,-1)	0	1	2517.5±1.4
Ξ_c^{*+}	$\{csu\}$	$\frac{3}{2}^+$	6*	(1/2,1/2)	-1	1	2646.6±1.5
Ξ_c^{*0}	$\{csd\}$	$\frac{3}{2}^+$	6*	(1/2,-1/2)	-1	1	2646.2±1.2
Ω_c^{*0}	$\{css\}$	$\frac{3}{2}^+$	6*	(0,0)	-2	1	Not seen
Ξ_{cc}^{*++}	$\{ccu\}$	$\frac{3}{2}^+$	6*	(1/2,1/2)	0	2	Not seen
Ξ_{cc}^{*+}	$\{ccd\}$	$\frac{3}{2}^+$	6*	(1/2,-1/2)	0	2	Not seen
Ω_{cc}^{*+}	$\{ccs\}$	$\frac{3}{2}^+$	6*	(0,0)	-1	2	Not seen
Ω_{ccc}^{++}	$\{ccc\}$	$\frac{3}{2}^+$	6*	(0,0)	0	3	Not seen

Since $l = 0$ and $l' = 0$, we have only spin combinations for the three quarks with no angular momentum contribution. The intermediate stages of spin combinations are given below;

J^P of (q_1q_2) : $\frac{1}{2}^+ \otimes \frac{1}{2}^+ \rightarrow (0^+ \oplus 1^+)$

J^P of $c(q_1q_2)$: $(0^+ \oplus 1^+) \otimes \frac{1}{2}^+ \rightarrow (0^+ \otimes \frac{1}{2}^+) \oplus (1^+ \otimes \frac{1}{2}^+) \rightarrow (\frac{1}{2}^+) \oplus (\frac{1}{2}^+ \oplus \frac{3}{2}^+)$

The Λ_c^+ ($c[ud]$) state is an isospin singlet (I = 0) and hence antisymmetric. The total orbital angular momentum for the Λ_c^+ is L = 0, therefore it is symmetric in ψ_L, as the color wavefunction is antisymmetric. In order for the entire wavefunction to be antisymmetric, the spin configuration of the diquark should be antisymmetric, i.e; spin = 0. The iospin I = 1 partners of the Λ_c^+ are the Σ_c states. Since the flavor (isospin) part is symmetric this implies that the spin of the diquark $\{q_1q_2\}$ in the Σ_c states should be 1. The spin 1/2 of the charm quark makes the Σ_c system a doublet in 'spin space'; $J_P = 1/2^+$ (Σ_c) and $J_P = 3/2^+$ (Σ_c^*). Both the Σ_c and Σ_c^* states decay into Λ_c^+ (being the lightest) via pion transition.

The Ξ_c system, *csu* and *csd*, contains a strange quark in association with an up or down quark in the diquark system. The wavefunction can now be symmetric $\{sq\}$ or antisymmetric $[sq]$. If the diquark is in antisymmetric configuration with spin = 0, then we get the Ξ_c^0 and Ξ_c^+ states. If the diquark is in symmetric configuration with spin = 1, then the pair couples with the third charm quark spin and results in the Ξ_c' ($J^P = \frac{1}{2}^+$) and Ξ_c^* ($J^P = \frac{3}{2}^+$) states. Ξ_c' is below the pion transition threshold, therefore decays via photon (electromagnetic) transition into the Ξ_c state, while the Ξ_c^* is massive enough to decay into a pion and Ξ_c ground state.

The charmed baryons with quark content *css*, can have only symmetric configuration in the diquark system $\{ss\}$. The diquark with spin 1 couples with the heavy charm quark resulting in two states; Ω_c^0 with $J^P = \frac{1}{2}^+$ and Ω_c^* with $J^P = \frac{3}{2}^+$. The

Ω_c^* is expected below the pion transition threshold, therefore it decays electromagnetically to the Ω_c^0 ground state. Fig. 2.4 shows the predicted masses and decay mechanisms of the S-Wave singly-charmed baryons.

Table 2.2: List of S-Wave Singly-Charmed Baryons : $(l = 0 \ \& \ l' = 0)$ [5]

$c(q_1q_2)$ $SU(4)$	J^P of (q_1q_2)	J^P of (cq_1q_2)	cud	cuu	cdd	csu	csd	css
$c[q_1q_2]$ $\overline{3}_{(M_A)}$	$[0^+]$	$[\frac{1}{2}^+]$ $2_{(M_A)}$	$\Lambda_c^+(2285)$	NONE	NONE	$\Xi_c^+(2468)$	$\Xi^0(2471)$	NONE
$c\{q_1q_2\}$ $6_{(M_S)}$	$\{1^+\}$	$\{\frac{1}{2}^+\}$ $2_{(M_S)}$	$\Sigma_c^+(2455)$	$\Sigma_c^{++}(2455)$	$\Sigma_c^0(2455)$	$\Xi_c^{+\prime}(2576)$	$\Xi_c^{0\prime}(2578)$	$\Omega_c^0(2697)$
$\{c\{q_1q_2\}\}$ $6^*_{(S)}$	$\{1^+\}$	$\{\frac{3}{2}^+\}$ $4_{(S)}$	$\Sigma_c^{*+}(2520)$	$\Sigma_c^{*++}(2520)$	$\Sigma_c^{*0}(2520)$	$\Xi_c^{*+}(2645)$	$\Xi_c^{*0}(2645)$	Ω_c^{*0}

We have seen so far that according to the Quark Model in the SU(4) sector, there are fifteen ground-state (S-Wave) singly-charmed baryons. There are nine $J^P = \frac{1}{2}^+$ states (three of type $\overline{\mathbf{3}}_{\mathbf{M_A}}$ and six of type $\mathbf{6}_{\mathbf{M_S}}$ representations) and six $J^P = \frac{3}{2}^+$ states (six of type $\mathbf{6}^*_{\mathbf{S}}$ representation). Table 2.2 shows the list of all S-Wave singly-charmed baryons.

2.3.2 P-Wave Charmed Baryons

The lowest lying P-Wave charm baryons have total angular momentum, $L = 1$. The total orbital state of the light diquark system can be characterized by two angular degrees of freedom, which are basically two independent relative momenta $l' = \frac{1}{2}(p_1 - p_2)$ and $l = \frac{1}{2}(p_1 + p_2 - 2p_3)$, that are determined by the two light diquarks (q_1 and q_2) momenta p_1 and p_2 and the heavy quark (Q) momentum p_3. Incorporating the orbitally excited charmed baryons in SU(4) Quark Model, we find sixty-three orbitally-excited (P-Wave) singly-charmed baryons. There are twenty

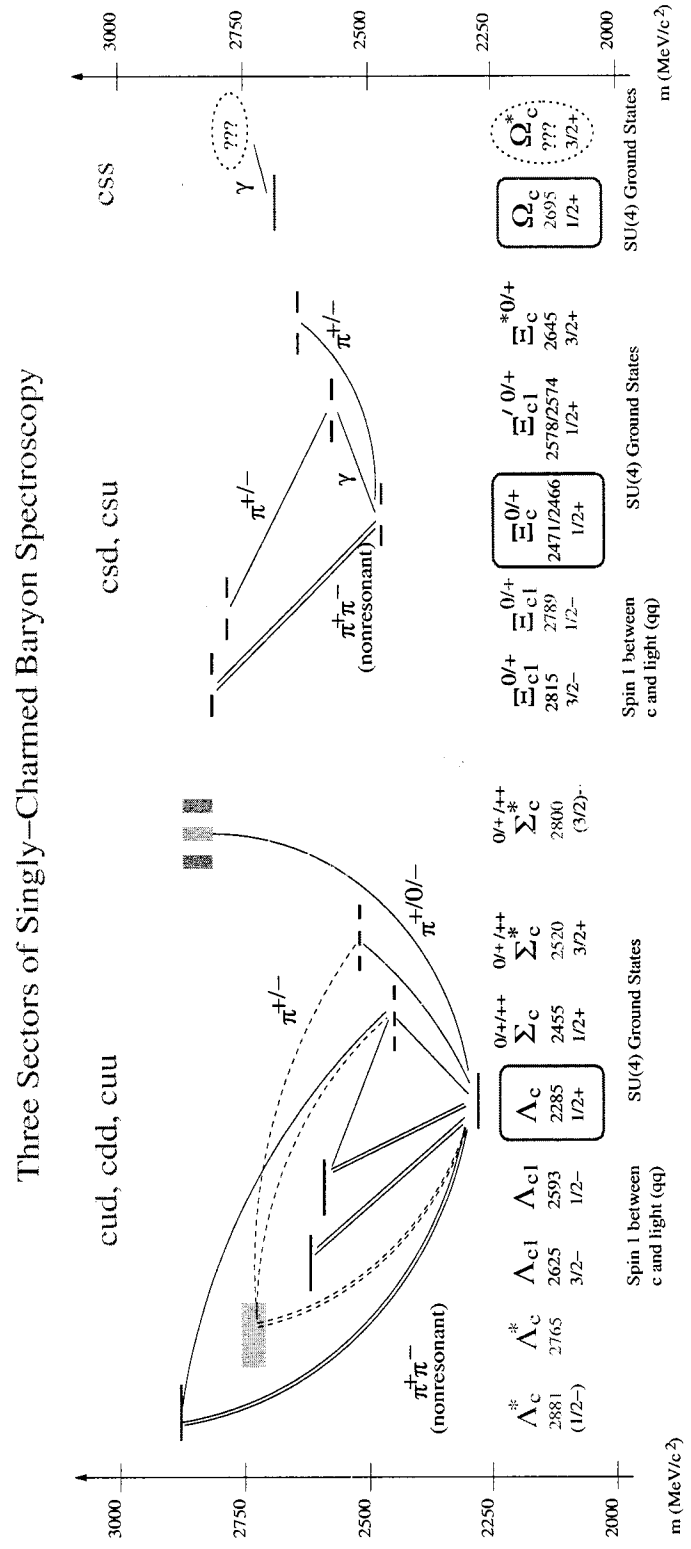

Figure 2.4: *Estimated masses of S-Wave and P-Wave singly-charmed baryons and their decay mechanisms.*

seven $J^P = \frac{1}{2}^-$ states (three of type $[\overline{\mathbf{3}}]_{\mathbf{A}}$, twelve of type $[\mathbf{6}]_{\mathbf{M_S}}$, six of type $[\mathbf{6}]_{\mathbf{S}}$, and six of type $[\overline{\mathbf{3}}]_{\mathbf{M_A}}$ representations), similarly twenty seven $J^P = \frac{3}{2}^-$ states (also, three of type $[\overline{\mathbf{3}}]_{\mathbf{A}}$, twelve of type $[\mathbf{6}]_{\mathbf{M_S}}$, six of type $[\mathbf{6}]_{\mathbf{S}}$, and six of type $[\overline{\mathbf{3}}]_{\mathbf{M_A}}$ representations), and nine $J^P = \frac{5}{2}^-$ states (six of type $[\mathbf{6}]_{\mathbf{M_S}}$ and three of type $[\overline{\mathbf{3}}]_{\mathbf{M_A}}$. Table 2.3 shows the list of P-Wave singly-charmed baryons both with ($l = 1$ & $l' = 0$) and ($l = 0$ & $l' = 1$) (notations used are merely for systematic naming) in both the cq_1q_2 and cqq sectors. Of all the 63 $L = 1$ orbitally excited singly-charmed baryons, 42 are of the type cq_1q_2 and 21 of the type cqq, respectively. In terms of spin and angular momentum we get the following combinations;

$$J^P \text{ of } (q_1q_2) : (\tfrac{1}{2}^+ \otimes \tfrac{1}{2}^+)\otimes 1^- \rightarrow (0^+ \oplus 1^+)\otimes 1^- \rightarrow (0^+\otimes 1^-)\oplus(1^+\otimes 1^-)$$
$$\rightarrow (1^-)\oplus(0^{-}\oplus 1^-\oplus 2^-)$$

$$J^P \text{ of } c(q_1q_2) : \{(1^{-})\oplus(0^{-}\oplus 1^-\oplus 2^-)\} \otimes \tfrac{1}{2}^+$$
$$\rightarrow \{(1^- \otimes \tfrac{1}{2}^+)\} \oplus \{(0^{-} \otimes \tfrac{1}{2}^+) \oplus (1^- \otimes \tfrac{1}{2}^+) \oplus (2^- \otimes \tfrac{1}{2}^+)\}$$
$$\rightarrow \{(\tfrac{1}{2}^- \oplus \tfrac{3}{2}^-)\} \oplus \{(\tfrac{1}{2}^-) \oplus (\tfrac{1}{2}^{-} \oplus \tfrac{3}{2}^-) \oplus (\tfrac{3}{2}^- \oplus \tfrac{5}{2}^-)\}$$

The lowest lying P-Wave ($l = 1$ and $l' = 0$) charmed baryons, have the SU(4) $[\overline{\mathbf{4}}]$ or $[\overline{\mathbf{3}}]$ representation, if we consider only $C = 1$. After the diquark couples with the one unit of angular momentum, we get a $J^P = \{1^-\}$, and a $J^P = \{0^-\}$ state, then another $J^P = \{1^-\}$ and a $J^P = \{2^-\}$ state; the first 1^- state then splits by its hyperfine interaction with the heavy charm quark, to produce two fermionic states, $J^P = \frac{1}{2}^-$ and $J^P = \frac{3}{2}^-$, and similarly the 0^-, 1^- and 2^- states also collectively split by their hyperfine interaction with the heavy charm quark, to produce five fermionic states of $J^P = \frac{1}{2}^-$, $\frac{1}{2}^-$ and $\frac{3}{2}^-$, $\frac{3}{2}^-$ and $\frac{5}{2}^-$; thus altogether seven states. Among these seven states, at the diquark level, the first two of the states are fully-antisymmetric under the interchange of flavor and spin of the light-quarks q_1 and q_2, whereas the next five states are fully-symmetric under the interchange of flavor and spin of the q_1

Table 2.3: List of P-Wave Singly-Charmed Baryons: ($l = 1$ & $l' = 0$) and ($l = 0$ & $l' = 1$) [2]

$c(q_1q_2)$ $SU(4)$	J^P of (q_1q_2)	J^P of (cq_1q_2)	cud	cuu	cdd	csu	csd	css
$[c[q_1q_2]]$ $\overline{3}_{(A)}$	$[1^-]$	$[\frac{1}{2}^-]$ $2_{(M_A)}$	$\Lambda_{c1}^{**+}(2593)$	NONE	NONE	$\Xi_{c1}^{**+}(2774)$	$\Xi_{c1}^{**0}(2772)$	NONE
$[c[q_1q_2]]$ $\overline{3}_{(A)}$	$[1^-]$	$[\frac{3}{2}^-]$ $2_{(M_A)}$	$\Lambda_{c1}^{**+}(2625)$	NONE	NONE	$\Xi_{c1}^{**+}(2816)$	$\Xi_{c1}^{**0}(2820)$	NONE
$c\{q_1q_2\}$ $6_{(M_S)}$	$\{0^-\}$	$\{\frac{1}{2}^-\}$ $4_{(S)}$	Σ_{c0}^{**+}	Σ_{c0}^{**++}	Σ_{c0}^{**0}	$\Xi_{c0}^{**+\prime}$	$\Xi_{c0}^{**0\prime}$	Ω_{c0}^{**0}
$c\{q_1q_2\}$ $6_{(M_S)}$	$\{1^-\}$	$\{\frac{1}{2}^-\}$ $2_{(M_S)}$	Σ_{c1}^{**+}	Σ_{c1}^{**++}	Σ_{c1}^{**0}	$\Xi_{c1}^{**+\prime}$	$\Xi_{c1}^{**0\prime}$	Ω_{c1}^{**0}
$c\{q_1q_2\}$ $6_{(M_S)}$	$\{1^-\}$	$\{\frac{3}{2}^-\}$ $2_{(M_S)}$	Σ_{c1}^{**+}	Σ_{c1}^{**++}	Σ_{c1}^{**0}	$\Xi_{c1}^{**+\prime}$	$\Xi_{c1}^{**0\prime}$	Ω_{c1}^{**0}
$c\{q_1q_2\}$ $6_{(M_S)}$	$\{2^-\}$	$\{\frac{3}{2}^-\}$ $4_{(S)}$	Σ_{c2}^{**+}	Σ_{c2}^{**++}	Σ_{c2}^{**0}	$\Xi_{c2}^{**+\prime}$	$\Xi_{c2}^{**0\prime}$	Ω_{c2}^{**0}
$c\{q_1q_2\}$ $6_{(M_S)}$	$\{2^-\}$	$\{\frac{5}{2}^-\}$ $4_{(S)}$	Σ_{c2}^{**+}	Σ_{c2}^{**++}	Σ_{c2}^{**0}	$\Xi_{c2}^{**+\prime}$	$\Xi_{c2}^{**0\prime}$	Ω_{c2}^{**0}
$c(q_1q_2)$ $SU(4)$	J^P of (q_1q_2)	J^P of (cq_1q_2)	cud	cuu	cdd	csu	csd	css
$\{c\{q_1q_2\}\}$ $6_{(S)}$	$[1^-]$	$[\frac{1}{2}^-]$ $2_{(M_A)}$	$\Sigma_{c'1}^{**+}$	$\Sigma_{c'1}^{**++}$	$\Sigma_{c'1}^{**0}$	$\Xi_{c'1}^{**+\prime}$	$\Xi_{c'1}^{**0\prime}$	$\Omega_{c'1}^{**0}$
$\{c\{q_1q_2\}\}$ $6_{(S)}$	$[1^-]$	$[\frac{3}{2}^-]$ $2_{(M_A)}$	$\Sigma_{c'1}^{**+}$	$\Sigma_{c'1}^{**++}$	$\Sigma_{c'1}^{**0}$	$\Xi_{c'1}^{**+\prime}$	$\Xi_{c'1}^{**0\prime}$	$\Omega_{c'1}^{**0}$
$c[q_1q_2]$ $\overline{3}_{(M_A)}$	$\{0^-\}$	$\{\frac{1}{2}^-\}$ $4_{(S)}$	$\Lambda_{c'0}^{**+}$	NONE	NONE	$\Xi_{c'0}^{**+}$	$\Xi_{c'0}^{**0}$	NONE
$c[q_1q_2]$ $\overline{3}_{(M_A)}$	$\{1^-\}$	$\{\frac{1}{2}^-\}$ $2_{(M_S)}$	$\Lambda_{c'1}^{**+}$	NONE	NONE	$\Xi_{c'1}^{**+}$	$\Xi_{c'1}^{**0}$	NONE
$c[q_1q_2]$ $\overline{3}_{(M_A)}$	$\{1^-\}$	$\{\frac{3}{2}^-\}$ $2_{(M_S)}$	$\Lambda_{c'1}^{**+}$	NONE	NONE	$\Xi_{c'1}^{**+}$	$\Xi_{c'1}^{**0}$	NONE
$c[q_1q_2]$ $\overline{3}_{(M_A)}$	$\{2^-\}$	$\{\frac{3}{2}^-\}$ $4_{(S)}$	$\Lambda_{c'2}^{**+}$	NONE	NONE	$\Xi_{c'2}^{**+}$	$\Xi_{c'2}^{**0}$	NONE
$c[q_1q_2]$ $\overline{3}_{(M_A)}$	$\{2^-\}$	$\{\frac{5}{2}^-\}$ $4_{(S)}$	$\Lambda_{c'2}^{**+}$	NONE	NONE	$\Xi_{c'2}^{**+}$	$\Xi_{c'2}^{**0}$	NONE

and q_2 quarks. Similarly, as discussed earlier we could also have ($l = 0$ and $l' = 1$), giving another seven states. Altogether we have fourteen states, although the spin of the diquark states now act in the opposite manner (i.e. those that were fully-antisymmetric are now fully-symmetric and vice versa). Here the corresponding five of the states, are fully-antisymmetric under the interchange of flavor and spin of q_1 and q_2, whereas the other two are fully-symmetric under the interchange of flavor and spin of the q_1 and q_2 quarks. One set of the seven states are of the Λ_c^+, Ξ_c^+, and Ξ_c^0 type and the other set of seven are of the Σ_c^+, $\Xi_c^{+\prime}$, and $\Xi_c^{0\prime}$ type if we are in the cq_1q_2 sector where q_1q_2 could either be a ud, su, or sd. It is essential to mention that very likely there may be a small mixing between the like J^P states of the $L = 1$ orbitally excited charmed baryons.

For the other three $C = 1$ charmed baryons, we have only seven states which are fully-symmetric under the interchange of the two light quarks. These states correspond to the $L = 1$ either ($l = 1$ and $l' = 0$) or ($l = 0$ and $l' = 1$) cases of Σ_c^0, Σ_c^{++}, and Ω_c^0. As we see here, apart from the angular momentum coupling factors, the dynamics of the light quark system is completely decoupled from the heavy quark. The estimated masses and decay mechanisms for some of the P-Wave charmed baryons are shown in Fig. 2.4. The hyperfine splitting of all S and P-Wave singly-charmed baryons is shown in Fig. 2.5 [2].

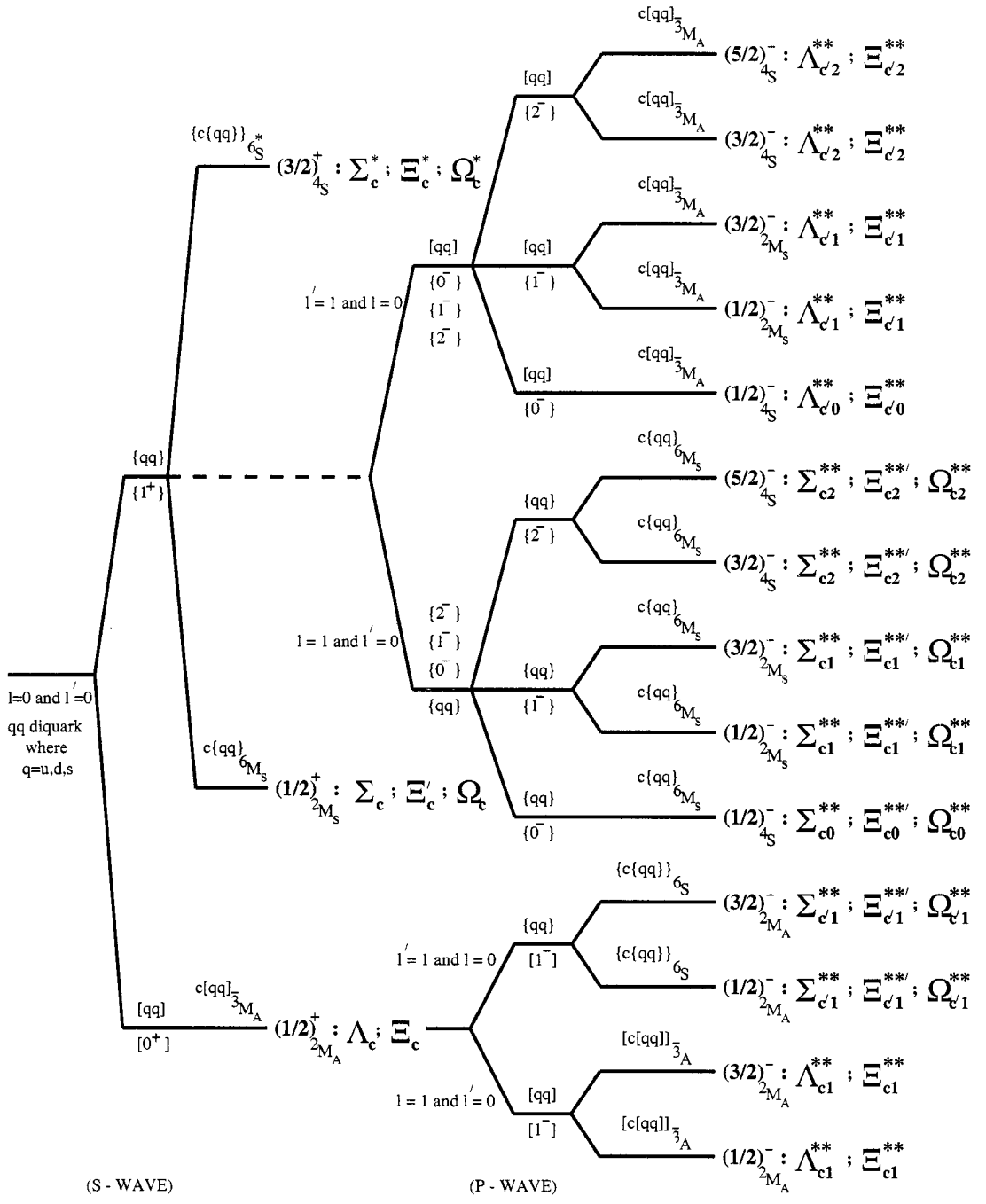

Figure 2.5: *Chromomagnetic hyperfine splitting of all S and P-Wave singly-charmed baryons.*

Chapter 3

History and Status of Σ_C

The Σ_c and Σ_c^* baryons are described in the standard model as members of the $J^P = \frac{1}{2}^+$ and the $J^P = \frac{3}{2}^+$ multiplets, respectively, each consisting of one charm and two light valence quarks. Depending on the flavor of the light constituent quarks, the Σ_c and Σ_c^* baryons have charges 0, +, or ++ (charge conjugation is implied throughout). The ground state $\Sigma_c(2455)$ and spin excited $\Sigma_c(2520)$ have been observed in different experiments and are quite well established. The first Σ_c state to be observed was the Σ_c^{++} baryon decaying into $\Lambda_c^+\pi^+$ in 1975, with a reported mass of 2426 ± 12 MeV/c^2. It had been produced in νp interactions at the BNL 7 feet cryogenic bubble chamber [16].

Discovery of the Σ_c^+ baryon was reported by the BEBC TST Neutrino Collaboration [20], which employed a bubble chamber equipped with a track sensitive target, irradiated by a wide band neutrino beam. The mass splittings and branching fractions were subsequently measured by ARGUS [21], CLEO II [22, 23] and FOCUS [24]. The first observation of Σ_c^{*++} production, with a mass of $2.530 \pm 0.005 \pm 0.005$ MeV/c^2 was reported in neutrino interactions on bubble chamber SKAT [25].

Recently, an isotriplet of a new orbital excited state $\Sigma_c(2800)$ has been reported by Belle Collaboration [26]. In this thesis we are trying to confirm some of their discoveries and measure the mass differences and widths of $\Sigma_c^0(2800)$ and $\Sigma_c^{++}(2800)$ in *BABAR*.

3.1 Decay Mechanism of Σ_c's

The Σ_c^{++}, Σ_c^+ and Σ_c^0 baryons consist of *cuu*, *cud* and *cdd* quark combinations respectively. They form an isospin doublet with isospin I = 1. As given in chapter 2, in case of S-Wave baryons, the diquark with $J^P = \{1^+\}$ combines with a charm quark of spin 1/2 and makes the Σ_c system a doublet in 'spin space', $J_P = 1/2^+$ (Σ_c) and $J_P = 3/2^+$ (Σ_c^*). Both the Σ_c and Σ_c^* states decay into Λ_c^+ (being the lightest charmed baryon) via pion transition.

For the case of P-Wave singly charmed baryons, there are three orbitally excited partners for Σ_c's. In first case a diquark with $J^P = \{1^-\}$ combines with a c quark to form $\Sigma_{c1}^{**}\{\frac{3}{2}^-\}$, in second case, the diquark with $J^P = \{2^-\}$ combines with c quark to form $\Sigma_{c2}^{**}\{\frac{3}{2}^-\}$ and $\Sigma_{c2}^{**}\{\frac{5}{2}^-\}$. These $\Sigma_{c2}^{**}\{\frac{3}{2}^-\}$ and $\Sigma_{c2}^{**}\{\frac{5}{2}^-\}$ can decay into Λ_c and a π via a P-wave and D-wave decay, respectively. The π charge depends on the charge of the Σ_c. The decay mechanisms for the three charges of Σ_c are shown in Fig.2.4.

3.2 Theoretical Models and Mass Predictions

Since the discovery of charm quark in 1974, many theorist have tried to calculate the masses of heavy baryons containing charm or beauty. In this regard, different

models have been developed to understand the nature of heavy quarks. The basic Quark model has also been modified to incorporate different kind of assumptions concerning particle velocities etc. We will briefly mention some of the models used for the prediction of Σ_c masses.

In 1975 Chiaki Itoh *et al.* [27] used a simple Non-Relativistic Quark model to discuss electromagnetic mass differences of charmed baryons. Later in 1979, they studied the effect of one gluon exchange and extended their study to Semirelativistic Quark Model. In 1988, the model was used to predict the mass difference (Σ_c^{++} - Σ_c^0) to be 1.08 MeV/c^2 and (Σ_c^+ - Σ_c^0) to be -0.35 MeV/c^2. Similarly the prediction for the mass difference (Σ_c^{*++} - Σ_c^{*0}) was -0.29 MeV/c^2 and (Σ_c^{*+} - Σ_c^{*0}) was -1.21 MeV/c^2. To estimate the baryon masses rather than the mass differences, in 1989, they calculated the expectation values of the Hamiltonian; $m =< \mathcal{H} >$. The space part of wave functions were taken to be the solutions of the three-body harmonic oscillators [28], modified by the forces due to Fermi-Breit terms, which may reduce the quark distances. The stronger the attractive force is between the quarks, the closer the quarks may be. They found the parameters which reproduce all the well-known experimental values of the ground-state baryons within $\pm$9 MeV/c^2. They computed the masses to be 2454.85 MeV for Σ_c^{++}, 2452.24 MeV/c^2 for Σ_c^+ and 2452.12 MeV/c^2 for Σ_c^0. For the excited states, the predicted masses were 2531.9 MeV for Σ_c^{*++}, 2529.8 MeV for Σ_c^{*+} and 2530.2 MeV for Σ_c^{*0}.

Another attempt was made by Copley, Isgur and Karl in 1979 [29]. They employed a quark model based on QCD to predict masses of ground state and excited baryons containing one charmed quark. They predicted a mass of 2.44 GeV/c^2 for $\Sigma_c(\frac{1}{2}^+)$, 2.51 GeV/c^2 for $\Sigma_c(\frac{3}{2}^+)$, 2.76 GeV/c^2 for $\Sigma_c(\frac{1}{2}^-)$, 2.77 GeV/c^2 for $\Sigma_c(\frac{3}{2}^-)$, 2.80 GeV/c^2 for $\Sigma_c(\frac{5}{2}^-)$, and 3.01 GeV/c^2 for $\Sigma_c(\frac{5}{2}^+)$ and $\Sigma_c(\frac{7}{2}^+)$.

Over some past years it has become widely recognized that the fundamental theory of strong interactions QCD, simplifies enormously in the presence of a very heavy quark. Nature has divided its six quarks into heavy and light quark sectors. The "heavy" c, b and t quarks are much heavier than the QCD scale $\Lambda_{QCD} \simeq$ 400 MeV [30], whereas the "light" u, d and s quarks are lighter than Λ_{QCD}, i.e. one has;

$$m_c, m_b, m_t >> \Lambda_{QCD} >> m_u, m_d, m_s.$$

The quark contribution to the QCD Lagrangian;

$$L_{quarks} \approx \overline{q}(iD_{uds} - m_q)q + \overline{Q}(iD_{cbt} - m_Q)Q$$

separates into two parts, the first contribution comes from light quarks (q = u, d and s), whereas the second one is due to heavy quarks (Q = c, b and t). In the heavy quark sector, then it makes sense to first consider QCD in the limit where the heavy quark masses become very large and then, in the second stage, to consider power corrections to this limit in terms of a systematic $1/m_Q$ expansion. Likewise, one can first study the light quark sector in the zero mass limit, i.e.; in the chiral symmetry limit, and then add corrections to the chiral limit at a later stage.

Each of the two approaches exhibit a distinct symmetry. The light-quark sector has an approximate $SU(3)_L \times SU(3)_R$ flavor chiral symmetry, as the current quark masses are all very small on the typical hadron energy scale. The symmetry is spontaneously broken to the usual vector $SU(3)$, and the chiral symmetry is reflected in the presence of eight bosons: the pions, kaons and η.

On the other hand, in the limit of infinite quark masses, the dynamics of a heavy quark in QCD depends only on its velocity and is independent of its mass and spin. Recently this notion has been given a more precise meaning in the *Heavy Quark*

Effective Theory (HQET) [31]. It provides a systematic expansion of QCD in terms of inverse powers of the heavy quark mass. The leading terms in this expansion give rise to a new spin and flavor symmetry, termed Heavy Quark Symmetry. The heavy quark at the center is surrounded by a cloud corresponding to a light diquark system. The only communication between the cloud and the center is via gluons. But since the gluons are flavor-blind, the light cloud does not know anything about the flavor at the center. Thus one concludes that, in heavy mass limit, a bottom baryon is identical to a charm baryon at rest, regardless of the spin orientation of the heavy quarks. This is known as the Heavy Quark Symmetry (HQS). More precisely, this new symmetry implies that the excitation spectrum of heavy mesons and baryons are independent of the heavy-quark species and heavy-quark spins. The theory describing the chiral symmetry was developed by Yan *et al.* [31].

In 1995, Martin Savage [32] made use of chiral perturbation theory and heavy quark symmetry. He predicted the mass of $\Sigma_c^* \sim 2518\,\mathrm{MeV}$.

The majority of the theorists nowadays use a custom made sum rule in addition to their basic formulation and often use the PDG charmed baryon masses (rather than their own, thus avoiding additional discrepancy) in their mass generating scheme when predicting the masses of the undiscovered states. The net result so far is indeed rather remarkable. Some of the predictions for the mass and isopspin splittings among the Σ_c and Σ_c^* baryons are given in Tables 3.1 and 3.2.

Table 3.1: Predictions for Isospin mass Splittings

Reference	Year	Theoretical Models	Σ_c Splitting ΔM (MeV/c^2)	Σ_c^* Splitting ΔM (MeV/c^2)
[33]	1977	Quark Model	Σ_c^{++}- Σ_c^{+}= 2.6 Σ_c^{+}- Σ_c^{0}= 0.8	Σ_c^{*++}- Σ_c^{*+}= 1.7 Σ_c^{*+}- Σ_c^{*0}= 0.1
[34]	1987	Chiral Bag	Σ_c^{++}- Σ_c^{0}= 3.0 Σ_c^{++}- Σ_c^{+}= 3.5	Σ_c^{*++}- Σ_c^{*0}= 2.7 Σ_c^{*++}- Σ_c^{*+}= 3.3
[35]	1987	Rel-Quark†	Σ_c^{++}- Σ_c^{0}= 1.4 Σ_c^{+}- Σ_c^{0}= 0.2	Σ_c^{*++}- Σ_c^{*0}= 0.1 Σ_c^{*+}- Σ_c^{*0}= 0.8
[36]	1987	Rel-Quark†	Σ_c^{++}- Σ_c^{0}= 1.4 Σ_c^{+}- Σ_c^{0}= 0.2	Σ_c^{*++}- Σ_c^{*0}= 0.1 Σ_c^{*+}- Σ_c^{*0}= 0.8
[37]	1993	Constituent Quark	Σ_c^{++}- Σ_c^{0}= 0.84 Σ_c^{++}+ Σ_c^{0}- $2\Sigma_c^{+}$= 1.64	Σ_c^{*++}- Σ_c^{*0}= 1.0 ± 0.52 Σ_c^{*++}+ Σ_c^{*0}- $2\Sigma_c^{*+}$= 1.64 ± 0.21

† Relativistic Quark

Table 3.2: Predictions of Σ_c and Σ_c^* masses.

Reference	Year	Theoretical Models	$[\Sigma_c]$ M (MeV/c^2)	$[\Sigma_c^*]$ M (MeV/c^2)
[29]	1979	Hyperfine Splitting	2440	2510
[28]	1989	Semi-Relativistic Quark	Σ_c^{++}= 2454.85 Σ_c^{+}= 2452.24 Σ_c^{0}= 2452.12	Σ_c^{*++}= 2531.9 Σ_c^{*+}= 2529.8 Σ_c^{*0}= 2530.2
[38]	1991	Potential	2450	2510
[37]	1993	Constituent Quark		2494 ± 16
[39]	1993	HQET	2455	2522
[32]	1995	Chiral-Perturbation		2518
[40]	1995	Constituent Quark	2453	2520
[41]	1995	Constituent Quark		2523
[42]	1996	Sum Rules	2453	2530
[43]	1996	Quark		2514
[44]	1996	HQET	2380	
[45]	1996	HQET		2532.5 ± 5.3
[46]	1996	Chiral Quark	2455	2494
[47]	2000	Semi-Rel Quark§	Σ_c^{++}= 2452.2 Σ_c^{+}= 2449.4 Σ_c^{0}= 2449.3	Σ_c^{*++}= 2526.5 Σ_c^{*+}= 2524.3 Σ_c^{*0}= 2524.8
[48]	2002	Lattice NRQCD	2452	2538
[49]	2005	HQS	2469	2548
[50]	2005	Rel-Quark†	2439	2518

† Relativistic Quark § Semi-Realtivistic Quark

In 1997, Pirjol and Yan [51] studied the strong interactions of the orbitally excited baryons with one heavy quark in the framework of Heavy Hadron Chiral Perturbation Theory. The interaction Lagrangian contains unknown couplings which describe the couplings of these states among themselves and with the ground state heavy baryons. They derived sum rules which constrain those unknown couplings and relate them to the couplings of s-wave baryons. Using a spin-3/2 baryon as a target, they found a sum rule expressing the deviation from the quark model prediction, for pion couplings to s-wave states in terms of couplings of the p-wave states. In the constituent quark model also, these couplings are related and can be expressed in terms of only six reduced matrix elements. They determined some of the unknown couplings in the chiral Lagrangian and two of the six quark model reduced matrix elements using CLEO data on Σ_c^* and $\Lambda_{c1}^{**}\{\frac{1}{2},\frac{3}{2}\}$ strong decays, where Λ_{c1}^{**} corresponds to $J^P = \{1^-\}$ for the light diquark pair. They predicted the widths for s-wave $\Sigma_c\{\frac{1}{2}\}$ and p-wave multiplets having $J^P = \{0^-, 1^-, 2^-\}$ for light degrees of freedom, which correspond to $\Sigma_{c0}\{\frac{1}{2}\}$, $\Sigma_{c1}\{\frac{1}{2},\frac{3}{2}\}$ and $\Sigma_{c2}\{\frac{3}{2},\frac{5}{2}\}$ respectively. In particular, they obtained

$$\Gamma\left(\Sigma_{c0}^{++}\right) \simeq 0.676^{+0.975}_{-0.385}\,\text{GeV} \tag{3.1}$$

The expected dominant decay mode for Σ_{c1} is into a Λ_c and a pion.. Their decay widths are given as;

$$\Gamma\left(\Sigma_{c1}\left(\frac{1}{2}\right)\right) \simeq 106.4^{+153.5}_{-60.7}\,\text{MeV} \tag{3.2}$$

and

$$\Gamma\left(\Sigma_{c1}\left(\frac{3}{2}\right)\right) \simeq 94.7^{+136.6}_{-54.0}\,\text{MeV} \tag{3.3}$$

The Σ_{c2} baryons have only D-Wave couplings and their dominant decay mode is

expected to be two-body decay to $\Lambda_c\pi$ given by;

$$\Gamma\left(\Sigma_{c2}^{++}\left(\frac{3}{2},\frac{5}{2}\right)\rightarrow\Lambda_c^{+}\pi^{+}\right)\simeq\ 12\,\mathrm{MeV} \tag{3.4}$$

where they used, $M_{\Sigma_{c2}} = 2800\,\mathrm{MeV}$. In addition to this decay mode, the Σ_{c2} baryons can also decay to $\Sigma_c{}^{(*)}\pi$. Adding together the contribution of all possible final states they obtained;

$$\Gamma\left(\Sigma_{c2}^{++}\left(\frac{3}{2}\right)\rightarrow\Sigma_c{}^{(*)}\pi\right)\simeq\ 3.16\,\mathrm{MeV} \tag{3.5}$$

$$\Gamma\left(\Sigma_{c2}^{++}\left(\frac{5}{2}\right)\rightarrow\Sigma_c{}^{(*)}\pi\right)\simeq\ 2.20\,\mathrm{MeV} \tag{3.6}$$

It was mentioned that even a small mixing of $\Sigma_{c2}\{\frac{3}{2}\}$ with the broader $\Sigma_{c1}\{\frac{3}{2}\}$ could enhance its decay width.

In the same year Glozman and Riska [46], gave a prediction of excited charm baryons in the Chiral Quark model. They showed that the spectra of the heavy flavor hyperons can be obtained by describing the fine structure interaction between the quarks in terms of the schematic chiral field flavor-spin interaction that is mediated by the $SU(3)_F$ octet of light psuedoscalar mesons. They predicted the masses for negative parity states $\Sigma_{c2}\{\frac{3}{2}^{-}\}$ and $\Sigma_{c2}\{\frac{5}{2}^{-}\}$ to be 2654 MeV.

Chiladze and Falk [52] predicted the Σ_{c2} states decaying to $\Lambda_c\pi$ through emission of a D-wave π to be narrow. It is due to a $\mid p_\pi \mid^5$ suppression in the D-wave decay widths, given as $\Gamma \approx 1\,\mathrm{MeV} \times \left(\frac{E_\pi - m_\pi}{100\,\mathrm{MeV}}\right)^{5/2}$, where p, E, and m are the momentum, energy and mass of the pion. But they also noted that the $\Sigma_{c2}\{\frac{3}{2}^{-}\}$ doublets could be broadened by mixing with the $\Sigma_{c1}\{\frac{3}{2}^{-}\}$ states.

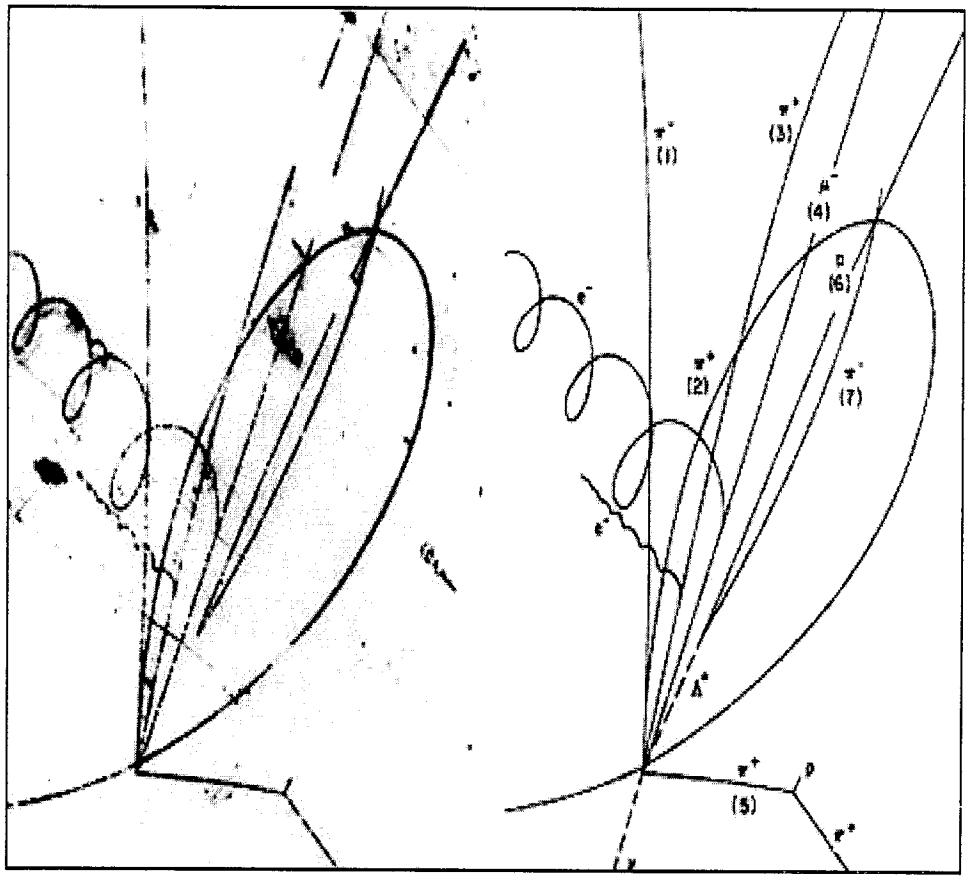

Figure 3.1: *View of the event recorded at Brookhaven National Laboratory, which was interpreted as the first evidence of* Σ_c^{++}.

3.3 Experimental Results

Measurements of the masses for Σ_c and Σ_c^* can be used to check models that predict the isospin mass splitting between these states and measurements of their widths can be compared to check the predictions of Heavy Quark Symmetry [51].

The first member of the doublet (Σ_c and Σ_c^*) to be observed experimentally was Σ_c^{++}. In an exposure of the Brookhaven National Laboratory 7-feet cryogenic bubble chamber to a broad-band neutrino beam, an event shown in Fig. 3.1 was observed.

It was interpreted as;

$$\nu p \rightarrow \mu^- \Lambda \pi^+ \pi^+ \pi^- \tag{3.7}$$

Later in 1979, Fermi National Accelerator Laboratory (FNAL) confirmed the existence of Σ_c^{++} and obtained a measurement of its mass and production rate [53]. They reported the mass difference (Σ_c^{++} - Λ_c^+) to be 168 ± 3 MeV/c^2. The ARGUS collaboration in 1988 observed both Σ_c^{++} and Σ_c^0 [21]. They measured the momentum spectrum and found it to be similar to that of Λ_c^+ with a Petersen function parameter of 0.29 ± 0.06. CLEO measured the mass differences for the two Σ_c's from continuum [22] and also from B decays [23]. Most recently the masses and Widths of the Σ_c^{++} and Σ_c^0 baryons have been measured by Focus [24] experiment at Fermilab. The measurements by the different experiments are summarized in the Table 3.3. The

Table 3.3: Measurements of Mass Differences, (Σ_c^{++}- Λ_c^+) and (Σ_c^0-Λ_c^+).

Experiment	Σ_c^{++}- Λ_c^+	Σ_c^0- Λ_c^+	Σ_c^{++}- Σ_c^0
ARGUS [21]	168.20 ± 0.50	167.00 ± 0.50	+1.20 ± 0.70 ± 0.30
CLEO II [22]	168.20 ± 0.30 ± 0.20	167.10 ± 0.30 ± 0.20	+1.10 ± 0.40 ± 0.10
E791 [54]	167.76 ± 0.29 ± 0.15	167.38 ± 0.29 ± 0.15	+0 .38 ± 0.40 ± 0.15
FOCUS [24]	167.35 ± 0.19 ± 0.12	167.38 ± 0.21 ± 0.13	-0. 03 ± 0.28 ± 0.11

first measurements of intrinsic width for Σ_c^{++} and Σ_c^0 were done by CLEO II.V [55]. They found the $\Gamma(\Sigma_c^{++}) = 2.3 \pm 0.2 \pm 0.3$ MeV and $\Gamma(\Sigma_c^0) = 2.5 \pm 0.2 \pm 0.3$ MeV. Their mass difference distributions are shown in Fig. 3.2.

The Σ_c^+ baryon was discovered by the BEBC TST Neutrino Collaboration [20]. An event with the decay chain $\Sigma_c^+ \rightarrow \Lambda_c^+ \pi^0$, where $\Lambda_c^+ \rightarrow pK^-\pi^+$was observed in an exposure of BEBC (Big European Bubble Chamber), which was equipped with large hydrogen filled TST (Track Sensitive Target), irradiated by a wide band of neutrino

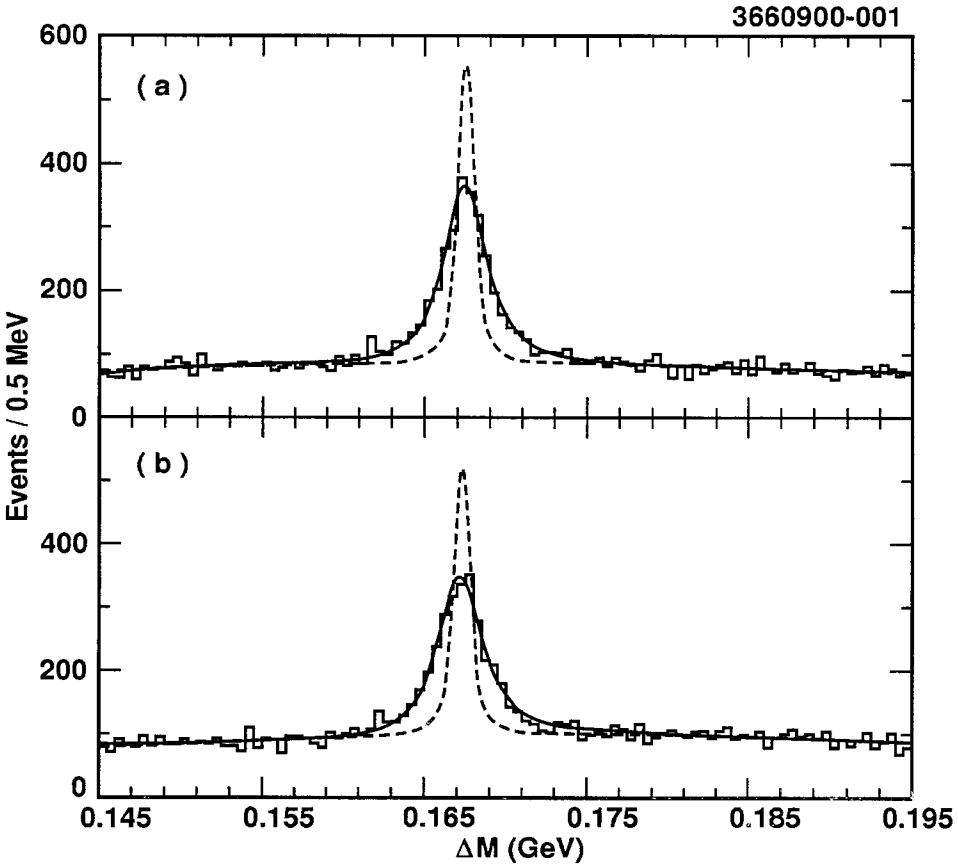

Figure 3.2: *Mass difference distribution (a) $M(\Lambda_c^+\pi^+ - \Lambda_c^+)$ and (b) $M(\Lambda_c^+\pi^- - \Lambda_c^+)$ as seen by CLEO II.V.*

beam at CERN. The mass difference (Σ_c^+- Λ_c^+) was measured to be 168 ± 3 MeV/c^2. Later, the CLEO collaboration contributed towards more precise measurements in this sector. Their results are summarized in Table 3.4. The most recent mass difference distribution by CLEO II.V [56] is shown in Fig. 3.3.

The excited partners $J_P = 3/2^+$ denoted by Σ_c^* were observed for the first time by CLEOII [57]. Until then, however, the evidence for Σ_c^* baryons was restricted to a cluster of 6 $\Lambda_c\pi^+$ events [25] with an estimated mass difference $M(\Sigma_c^* - \Lambda_c^+)$ of $245\pm5\pm5$ MeV/c^2. Most recently the masses and widths of the Σ_c^{*++} and Σ_c^{*0} baryons

Table 3.4: Measurements of Mass Differences, (Σ_c^+- Λ_c^+) from CLEO.

Experiment	Σ_c^+- Λ_c^+
CLEO II [22]	$168.5 \pm 0.4 \pm 0.2$
CLEO II.V [56]	$166.4 \pm 0.2 \pm 0.3$

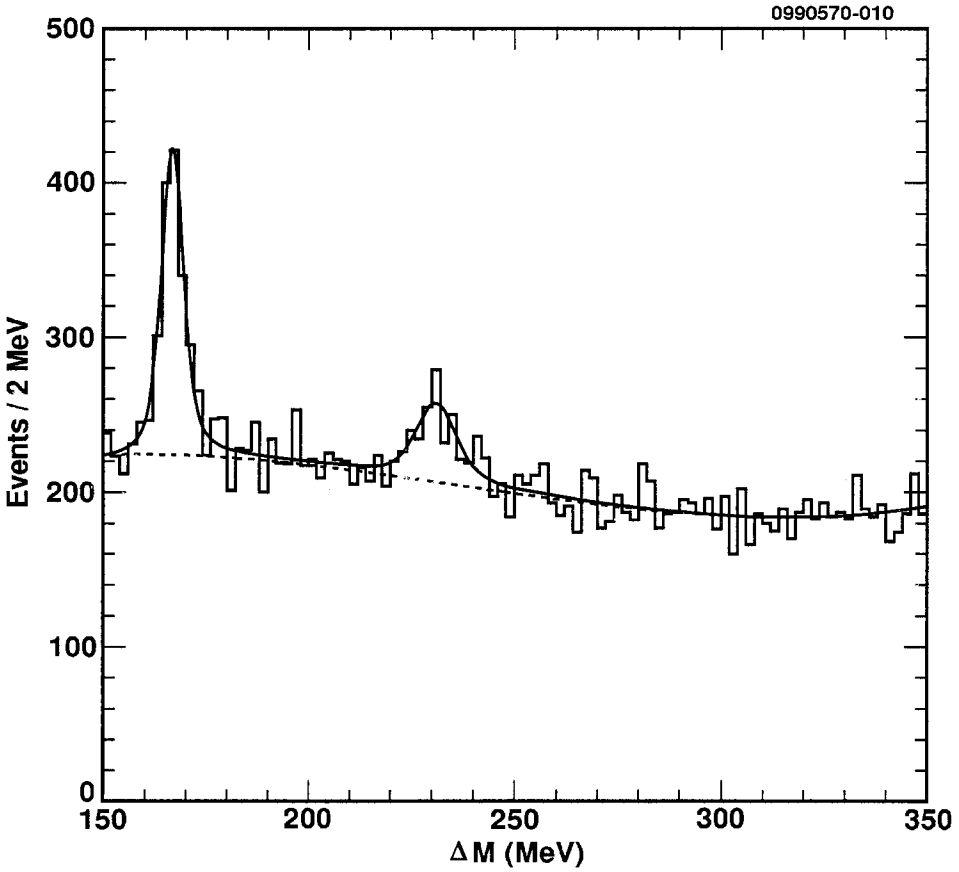

Figure 3.3: *Mass difference distribution* $M(\Lambda_c^+\pi^0 - \Lambda_c^+)$ *as seen by CLEO II.V. The signal is fitted to two p-wave Breit-Wigner functions smeared by gaussian resolution functions and a third-order polynomial background.*

have been measured by CLEO III [58]. As shown in Fig. 3.4, they obtained a signal of 1330 ± 110 events with a width of $\Gamma = 14.4\ ^{+1.6}_{-1.5}$ MeV and mass difference ΔM =

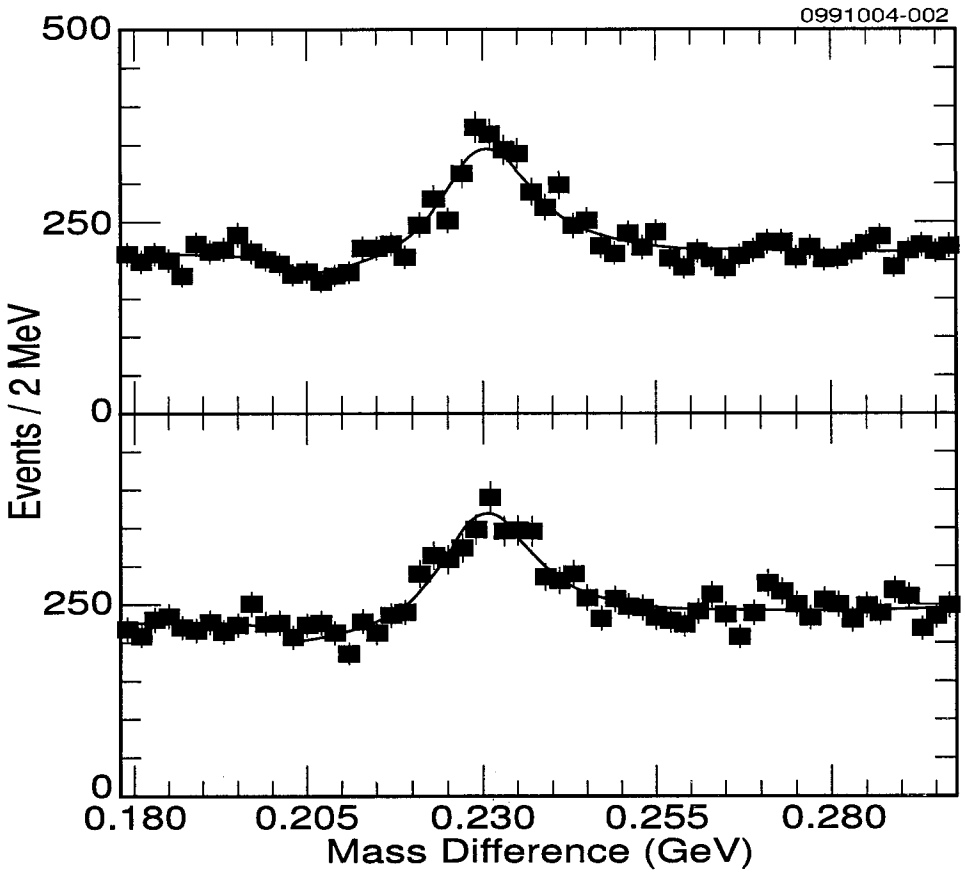

Figure 3.4: *Mass difference distribution* $M(\Lambda_c^+\pi^- - \Lambda_c^+)$ *as seen by CLEO III. The upper plot is for* π^+ *and lower for* π^-.

231.5 ± 0.4 MeV/c^2 for $\Lambda_c^+\pi^+$. For the $\Lambda_c^+\pi^-$, they obtained a signal of 1350 ± 120 events with a width of $\Gamma = 16.6\ ^{+1.9}_{-1.7}$ MeV and mass difference $\Delta M = 231.4 \pm 0.5$ MeV/c^2. The isospin splitting which was expected to be small and negative [59] was measured to be $-0.1 \pm 0.8 \pm 0.3$ MeV. According to Heavy Quark Symmetry [51], the ratio $\Gamma(\Sigma_c^*)/\Gamma(\Sigma_c)$ should equal $(M_{\Sigma_c}/M_{\Sigma_c^*}) \times (p_\pi^3(\Sigma_c^*)/p_\pi^3(\Sigma_c))$, where p_π is the momentum of the π in the parent's rest frame. This quantity is predicted to be equal to 7.5 ± 0.1. Using their measured widths, CLEO calculated $\Gamma(\Sigma_c^{*++})/\Gamma(\Sigma_c^{++}) = 6.5 \pm 1.3$ and $\Gamma(\Sigma_c^{*0})/\Gamma(\Sigma_c^0) = 7.5 \pm 1.7$, in excellent agreement with the expectation.

Also the mass difference (Σ_c^{*+}- Λ_c^+) measured by CLEO II.V [56] was 231.0±1.1±2.0 MeV/c^2.

The Belle Collaboration [26] reported the first observation of the orbital excited state $\Sigma_c(2800)$ in the three charge modes. These results were obtained from a 281 fb^{-1} data sample collected near the $\Upsilon(4S)$ resonance, at the KEKB asymmetric e^+ e^- collider. The results for their search are summarized in the Table below. The mass difference plots for the three charged states are shown in Fig. 3.5.

Table 3.5: Signal yields, mass difference and width for $\Sigma_c(2800)$from Belle.

State	Yield	Mass Diff (Σ_c- Λ_c^+) GeV/c^2	Γ GeV
$\Sigma_c^0(2800)$	$2240\ ^{+790\ +1030}_{-550\ -500}$	$0.5154\ ^{+0.0032\ +0.0021}_{-0.0031\ -0.0060}$	$0.061\ ^{+0.018\ +0.022}_{-0.013\ -0.013}$
$\Sigma_c^+(2800)$	$1540^{+1050\ +1400}_{-570\ -880}$	$0.5054\ ^{+0.0058\ +0.0124}_{-0.0046\ -0.0020}$	$0.062\ ^{+0.037\ +0.052}_{-0.023\ -0.038}$
$\Sigma_c^{++}(2800)$	$2810^{+820\ +710}_{-600\ -490}$	$0.5145\ ^{+0.0034\ +0.0028}_{-0.0031\ -0.0049}$	$0.075\ ^{+0.018\ +0.012}_{-0.013\ -0.011}$

The Λ_c^+candidates were reconstructed in the $pK^-\pi^+$ mode and the signal window around the Λ_c^+ mass was taken to be ±8MeV/c^2(1.6σ). The Λ_c^+ candidates were then combined with a π candidate in the event to form $\Sigma_c(2800)$ candidates. A requirement on the scaled momentum $x_p > 0.7$, where $x_p = \frac{p}{\sqrt{E_{beam}^2 - M^2}}$, was imposed on the $\Lambda_c^+\pi$ pair to reduce the combinatorial background. To further reduce the contribution from low momentum pions it was required that the decay angle θ_{dec} satisfy, $\cos\theta_{dec} > -0.4$. The decay angle θ_{dec} is defined to be the angle between the π momentum measured in the rest-frame of the $\Lambda_c^+\pi$ system, and the boost direction of the $\Lambda_c^+\pi$ system in the CM frame. This requirement was chosen assuming a flat $\cos\theta_{dec}$ distribution.

The lower peaks at a mass difference of 0.42 GeV/c^2 were interpreted as feed-down from the decay $\Lambda_c^+(2880) \rightarrow \Lambda_c^+\pi^+\pi^-$. The $\Lambda_c^+(2880)$ resonance was observed

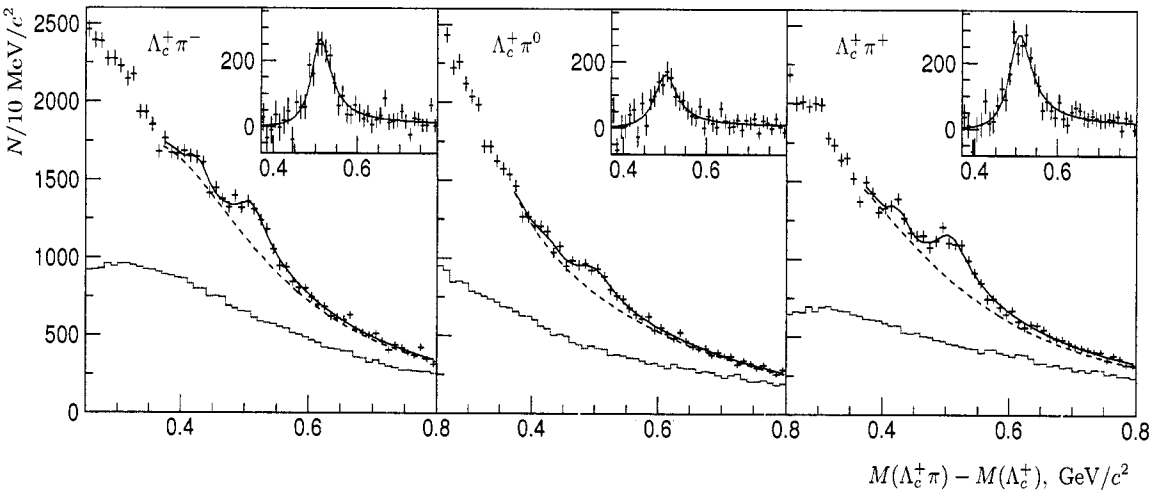

Figure 3.5: *Isotriplet of Excited Charm baryons decaying to $\Lambda_c^+\pi$ as found by Belle. The points with error bars are mass distributions from the Λ_c^+ signal region and the histograms are from normalized sidebands. The insets show the background subtracted distributions in the signal region.*

by CLEO [60] in the $\Lambda_c^+\pi^+\pi^-$ final state and they found that 30% of the decays proceed via an intermediate $\Sigma_c^0(2455)$ or $\Sigma_c^{++}(2455)$. From a MC study Belle found that if $\Lambda_c^+\pi^\pm$ pairs are produced from intermediate $\Sigma_c^{++}(2455)$ or $\Sigma_c^0(2455)$, then the mass difference plot for the $\Lambda_c^+\pi^\mp$ spectrum is peaked around 0.43 GeV/c^2. For the $\Lambda_c^+\pi^0$ final state, a feed-down from the decay $\Lambda_c^+(2880) \rightarrow \Lambda_c^+\pi^0\pi^0$ was expected. Since the reconstruction efficiency is quite low for the π^0's, the shape and normalization for the $\Lambda_c^+(2880) \rightarrow \Lambda_c^+\pi^0\pi^0$was determined using the following relation

$$B(\Lambda_c^+(2880) \rightarrow \Lambda_c^+\pi^0\pi^0) = 0.5 * B(\Lambda_c^+(2880) \rightarrow \Lambda_c^+\pi^+\pi^-)$$

The $\Sigma_c(2800)$ states were identified as Σ_{c2} baryons, where the subscript 2 denotes the total angular momentum of the light quark system. The background was parameterized by an inverse third order polynomial.

They calculated the product $\sigma(e^+e^- \rightarrow \Sigma_c^0(2800)X).\mathcal{B}(\Sigma_c(2800) \rightarrow \Lambda_c^+\pi)$ to be

$$(2.04\ ^{+0.72}_{-0.50}\ ^{+0.97}_{-0.52} \pm 0.53)\ pb \quad for \quad \Sigma_c^0(2800),$$

$$(2.6\ ^{+1.8}_{-1.0}\ ^{+2.4}_{-1.5} \pm 0.7)\ pb \quad for \quad \Sigma_c^+(2800)$$

and

$$(2.36\ ^{+0.69}_{-0.50}\ ^{+0.64}_{-0.47} \pm 0.61)\ pb \quad for \quad \Sigma_c^{++}(2800).$$

The first uncertainty here is statistical, the second is systematic and the third is due to the uncertainty in $\Lambda_c^+ \rightarrow pK^-\pi^+$ branching fraction.

Chapter 4

The *BABAR* Experiment

The *BABAR* experiment at the Stanford Linear Accelerator Center was launched in December 1993. The primary goal of this asymmetric B Factory is the systematic study of CP violation in the B meson system. Asymmetric beam energies facilitate the measurement of time dependent CP violating asymmetries in the decay of neutral B mesons. The high integrated luminosity and the excellent reconstruction efficiency needed for this purpose, however, makes the *BABAR* experiment interesting for a wide range of physics studies such as charm, bottom(non-CP physics), tau and two-photon. The PEP-II is an asymmetric e^+e^- collider, whose two beams are tuned to collide at the mass of the $\Upsilon(4S)$ resonance ($\sqrt{s} = 10.58$ GeV), which is just above the production threshold for $B\overline{B}$ pairs. This is optimal because the $\Upsilon(4S) \rightarrow B\overline{B}$ branching fraction is almost 100%. However, an $\Upsilon(4S)$ is only produced in approximately 20% of hadronic events, with a cross section of 1.05 nb. The remaining 80% of events are made up of light quark continuum events, where the colliding electrons produce a $q\bar{q}$ pair (with q being a u, d, s or c quark), which has a cross-section of 3.3 nb, or of τ events whose cross-section is 0.9 nb.

Taking advantage of the large sample of charm baryons provided by the high luminosities of PEP-II, we are going to study the charmed baryons Σ_c's in this thesis. The data sample used for this analysis is given in Section 4.3. First we give a brief description of PEP-II and the *BABAR* detector. A detailed description of the *BABAR* detector and PEP-II can be found in [61, 62, 63].

4.1 PEP-II

The PEP-II* B factory is a two ring asymmetric e^+e^- collider designed to operate at a luminosity of 3×10^{33} $\mathrm{cm}^{-2}\mathrm{s}^{-1}$ and above, at a center-of-mass energy of 10.58 GeV, the mass of the $\Upsilon(4S)$ resonance. Electron and positron beams are accelerated along a 2 mile long linear accelerator until they reach their target energies of 9.0 GeV and 3.1 GeV respectively. They are then fed into the storage rings until they are collided head-on. The unequal beams boost the $\Upsilon(4S)$ in the laboratory frame with $\beta_\gamma = 0.56$. The reason for choosing e^+e^- was its higher signal-to-background ratio compared to hadronic systems, clean B meson events with low multiplicity ($\sim$ 11), which allows for reconstruction of final states with photons and π^0's, and low interaction rates (so that the detector is not flooded with data during its dead-time).

A schematic representation of the acceleration and the storage system is shown in Fig. 4.1. An electron gun creates electron bunches which are then accelerated to about 1 GeV and then fed into a damping ring, which is used to "cool" the bunches. Which means the bunches are condensed so that they have higher density. Electrons are then accelerated again in the linear portion of the Linac. Of the two bunches generated every 1/120th of a second, one of the bunches is diverted and smashed

*PEP is an acronym for Positron Electron Project

Table 4.1: Production cross-section at the $\Upsilon(4S)$ resonance [61].

$e^+e^- \rightarrow$	Cross-section (nb)
$b\bar{b}$	1.05
$c\bar{c}$	1.30
$s\bar{s}$	0.35
$u\bar{u}$	1.35
$d\bar{d}$	0.35
$\tau^+\tau^-$	0.94
$\mu^+\mu^-$	1.16
e^+e^-	40

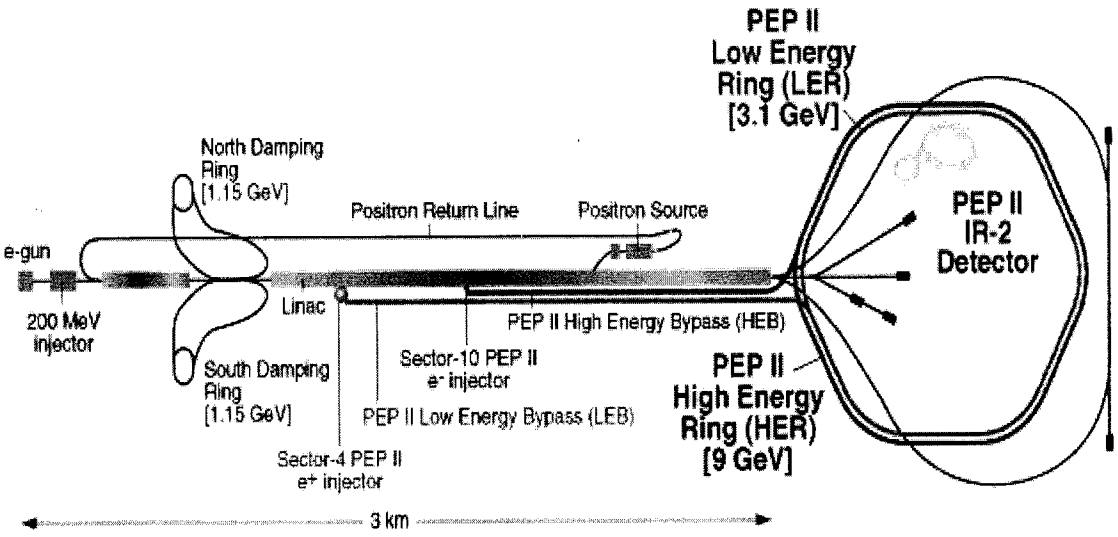

Figure 4.1: *A schematic representation of the acceleration and the storage system at PEP-II.*

into a target once it has reached 30 GeV. These high energy collisions create many particles, of which positrons are captured (at an energy of 10 MeV). The positrons are returned to the region near the electron gun, where they are accelerated and then fed into damping rings. Following that, the positrons are accelerated concurrently

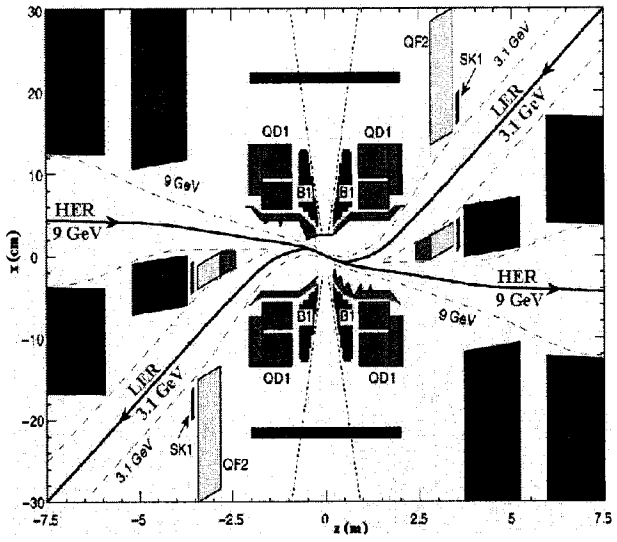

Figure 4.2: *A plan view of the interaction region(IR). The vertical scale is exaggerated. The dashed lines indicate the beam stay-clear region and the detector acceptance cutoff at 300 mrad.*

with the electrons. The electrons are accelerated in the High Energy Ring (HER) to 9.0 GeV and positrons are accelerated in the Low Energy Ring (LER) to 3.1 GeV. At these energies, the particles are diverted into bypass tunnels, which feed the particles into PEP-II, which is the storage system. Collisions occur at the interaction region (IR), shown in Fig. 4.2, where *BABAR* is sitting to watch the outcome.

The bunches must be brought into focus for collisions just before the interaction point (IP), and separated directly afterwards to avoid secondary collisions and spurious collisions between out of phase bunches. Focusing the beams requires the use of the quadrupoles labeled QD and QF. The ones used for focusing HER are QD4 and QF5, whilst QF2 is responsible for focusing the LER. These are iron magnets which are placed outside the field of the *BABAR* solenoid. The QD1 quadrupole is the final focus for both the HER and the LER and is a permanent magnet located

within the solenoid. A strong dipole (B1) in close proximity (±21 cm away) is necessary to bring together and separate the beams by causing horizontal displacement. Both QD1 and B1 are permanent magnets while QF2, QD4 and QF5 are standard iron electro-magnets. The IR is within the beryllium beam pipe which has an outer radius of 27.9mm and is water cooled. This beam-pipe, with the permanent magnets and the silicon vertex tracker, is enclosed within a 4.5m long support tube.

High machine backgrounds cause significant problems due to high occupancies within the subsystems of the *BABAR* detector. This can cause dead-time inside the detector, resulting in a loss of data, and also radiation damage to the subdetectors. It is imperative that these background are kept to an absolute minimum. There are three sources of this background: luminosity background, synchrotron radiation and particles lost due to interactions with the beam-pipe or residual gas molecules within the beam-pipe.

Luminosity backgrounds are caused by radiative Bhabha scattering which results in energy-degraded electrons and positrons hitting the beam pipe which surrounds the IR or other PEP-II components and consequently spraying the detector with electromagnetic shower debris. This is an unavoidable source of background and increases along with luminosity. Backgrounds due to collisions with gas molecules in the beam-pipe are reduced by having a strong vacuum within the beam-pipe near IP. Focusing and separating the asymmetric beams within the IR generates a great amount of synchrotron radiation, which is the greatest source of machine background. Various components within the IR are designed to channel and absorb synchrotron photons so that they never enter the detector, and copper masks are used to prevent interaction with the beam-pipe.

The impressive luminosity of $9.213 \times 10^{33}\,\mathrm{cm}^{-2}\mathrm{s}^{-1}$ was achieved by using a trickle

mode (a mode of operation which increases the production of $B\overline{B}$ pairs by up to 50%, with this technique the *BABAR* can keep taking data virtually uninterrupted while the Linac injects the electrons and positrons into the PEP-II storage rings). Within five years of its operation PEP-II has not only achieved its design luminosity but has also surpassed it by about 60%.

4.2 *BABAR* Detector

The *BABAR* detector is an asymmetric detector, offset in z from the beam-beam interaction point by 0.37m in order to provide the best coverage of the boosted $\Upsilon(4S)$ decays. Therefore, the y-axis lies vertically upwards and the x-axis points horizontally away from the center of the PEP-II rings. The polar (θ) and azimuth (ϕ) angles are defined in the traditional way, relative to the z-axis. The detector shown in Fig. 4.3 and 4.4, consists of five sub-detectors and a magnet.

The silicon vertex tracker (SVT) is closest to the beam pipe and is designed to measure positions of charged particles accurately, which allows precise determination of decay vertices. It is surrounded by a cylindrical wire chamber, the drift chamber (DCH), which provides momentum measurements for charged particles as well as a measurement of the energy loss dE/dx, which aids in particle identification. The detector of internally reflected Cerenkov light (DIRC) surrounds the DCH and is a particle identification device designed to distinguish charged hadrons such as kaons, pions and protons. The electromagnetic showers of electrons and photons are detected by the CsI crystals of electromagnetic calorimeter (EMC). These four sub-detectors are surrounded by a superconducting solenoid providing a field of 1.5T. The steel flux return of the magnet is segmented into layers and is instrumented

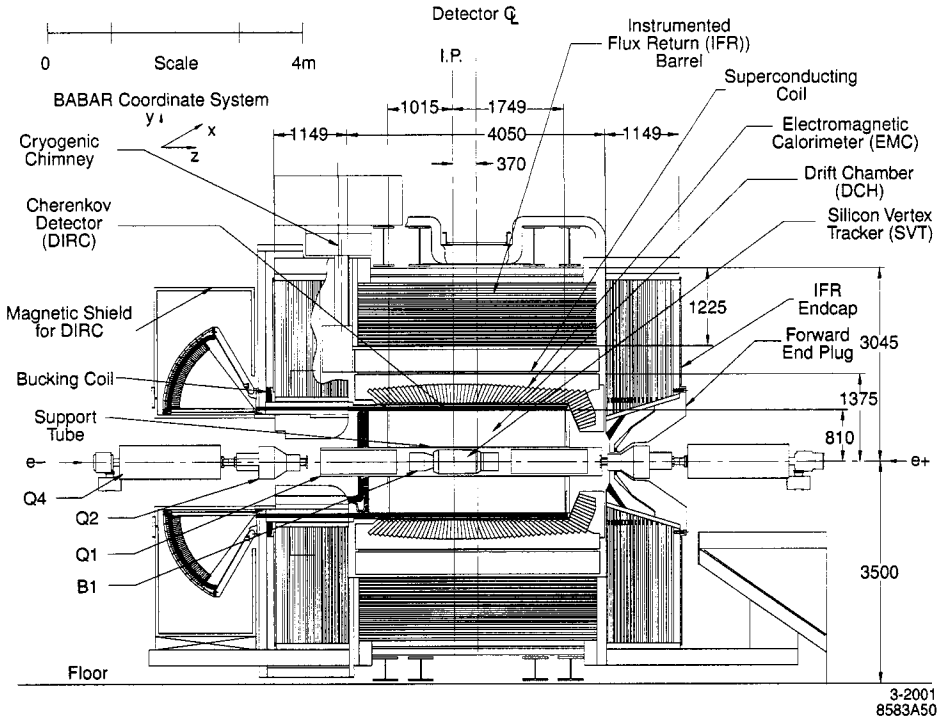

Figure 4.3: *BABAR detector: longitudinal view.*

for muon and neutral hadron detection. This system is known as instrumented flux return (IFR). The detector acceptance is $17^o < \theta_{lab} < 150^o$ in the laboratory frame ($-0.95 < \cos\ \theta_{CM} < 0.87$).

4.2.1 The Silicon Vertex Tracker (SVT)

Silicon vertex tracker (SVT) measures the angles and positions of charged particles just outside the beam pipe. Tracks that have a sufficiently low momentum do not reach the DCH and hence SVT provides stand-alone tracking information for particles with transverse momentum, p_t, less than 120 MeV/c. SVT is the only one solely responsible for measuring decay vertices near the interaction region, with a required resolution of less than 80 μm in the z direction and around 100 μm in the plane perpendicular to the beam line. It should cover as much of the solid

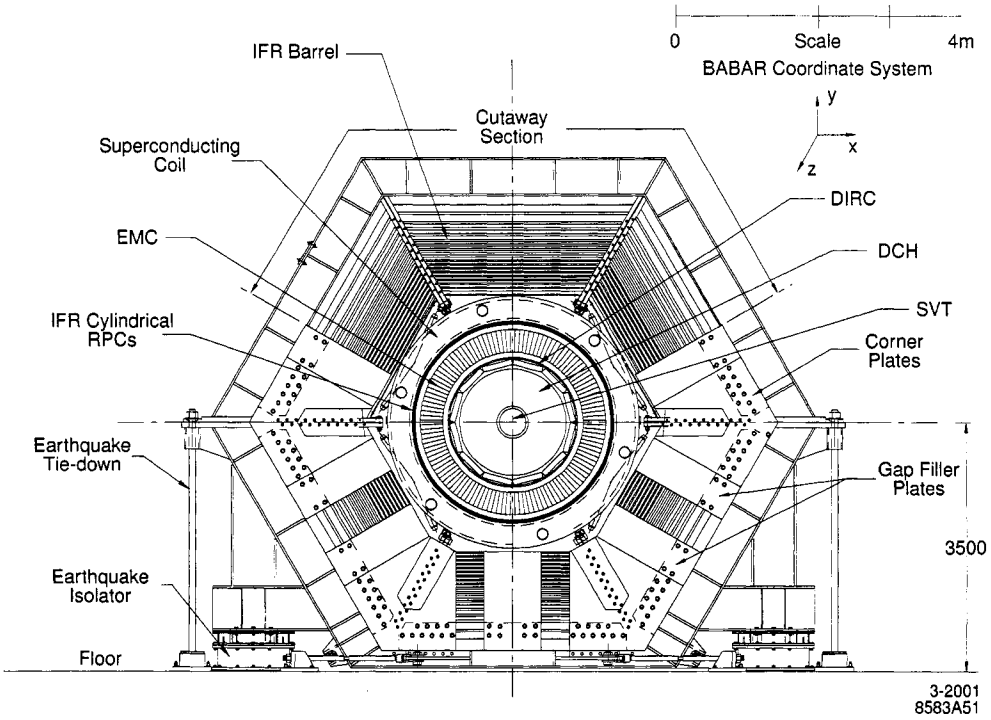

Figure 4.4: *BABAR detector: cut-away end view.*

angle as possible (the presence of the PEP-II magnets prevent total coverage) and also contain as little material as possible to minimize Bremsstrahlung and multiple scattering which will affect subsequent measurements by the other sub-detectors. The SVT also contributes to Particle Identification (PID), particularly for particles with momenta below 700 MeV/c, using measurements of ionization loss dE/dx.

The SVT is designed with five layers of double sided silicon strip sensors as shown in Figs. 4.5 and 4.6. The three inner layers perform the impact parameter measurements and are positioned very close to the beam pipe (3-5 cm from IP), to minimize the affect of multiple scattering on subsequent measurements by the other sub-detectors. The remaining two layers are further away and perform low p_t tracking and form the link between the SVT and the DCH information. The five layers are organized in 6, 6, 6, 16 and 18 modules respectively, with inner layers

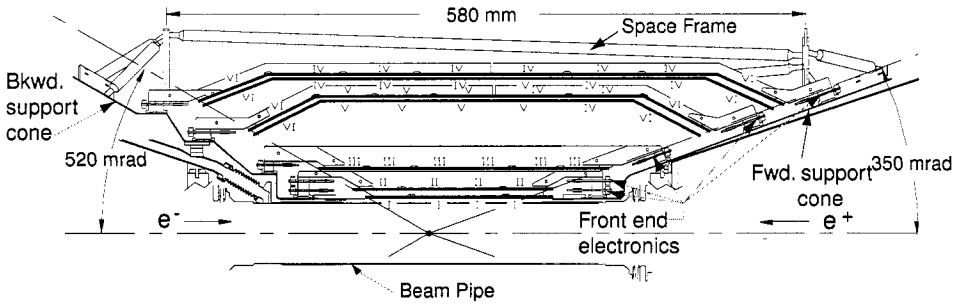

Figure 4.5: *The SVT detector: longitudinal view.*

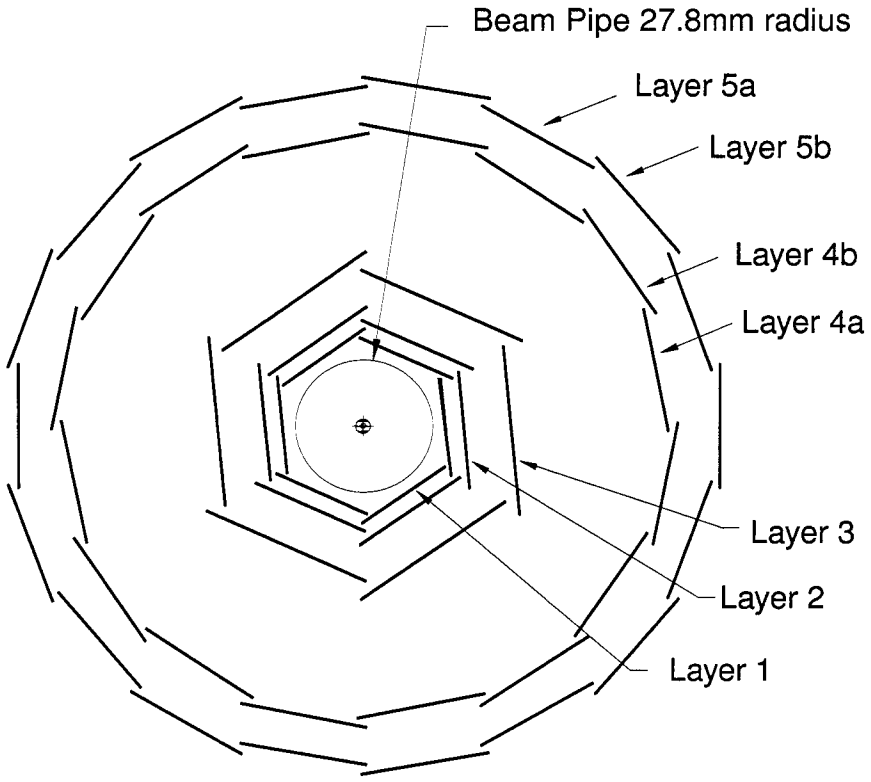

Figure 4.6: *The SVT detector: transverse view.*

tilted slightly to give overlap between adjacent modules. The arched design of the two outer layers is intended to reduce the amount of material required to cover the

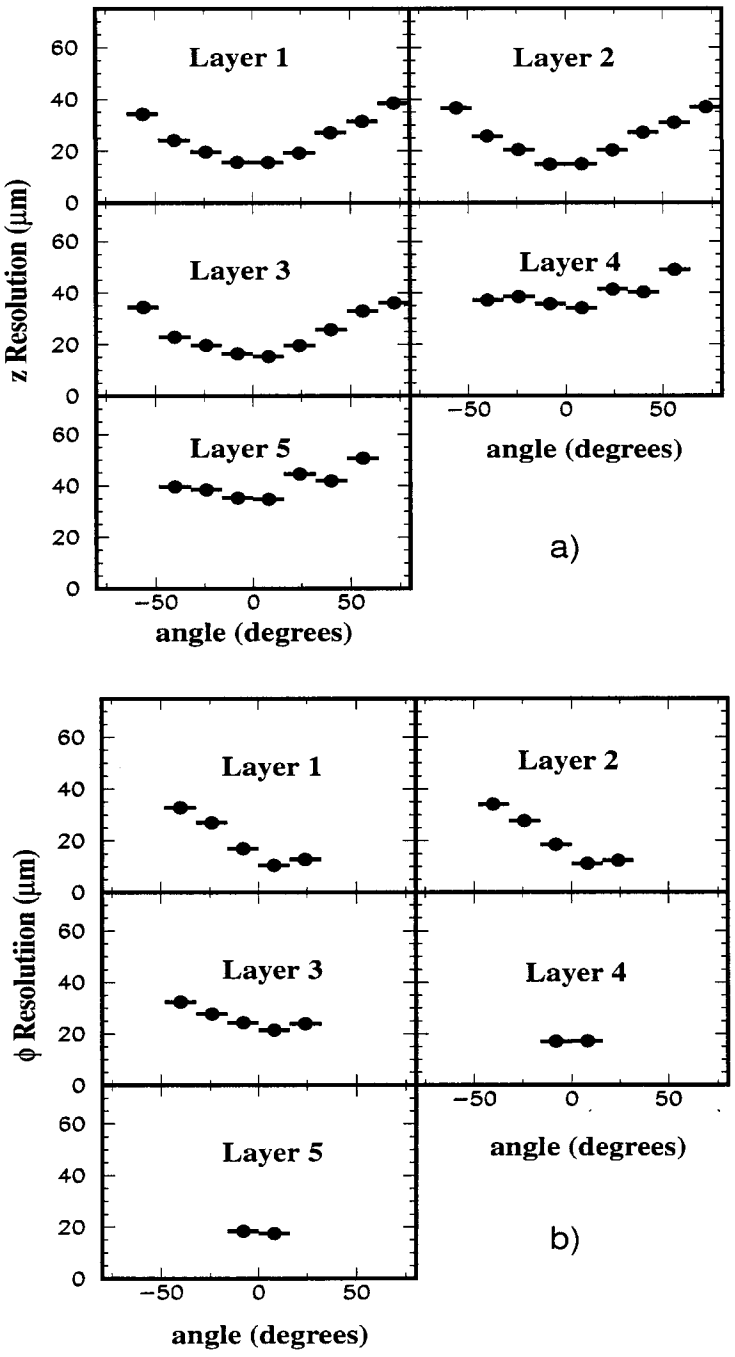

Figure 4.7: *SVT hit resolution in z (a) and ϕ (b) coordinate as a of function track incident angle. There are fewer points in the ϕ resolution plots for the outer two layers because the range of incident angles subtended is much smaller.*

solid angle.

The silicon strips on each side of a sensor are positioned orthogonally to each other, with ϕ measuring strips parallel to the beam and the z measuring strips oriented transversely to the beam axis. Each layer is constructed with flat, square silicon wafers so that, there is no uncovered region in ϕ and that there is maximum tracking acceptance in θ. Fig. 4.7 shows both z and ϕ single-hit resolutions for each

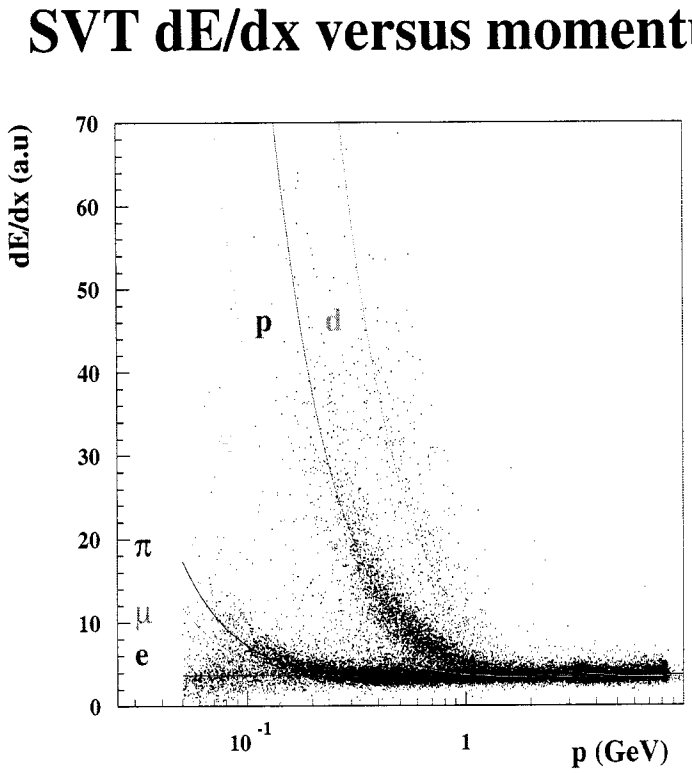

Figure 4.8: *Distribution of SVT dE/dx as a function of track momentum.*

The modules are electrically divided into two half-modules, which are read out at the ends. There are approximately 150,000 readout channels. An electrical pulse is created within a strip when a charged particle traverses the silicon. These are carried to the Front End Electronics (FEE), where the quantity measured is the time for which a pulse is over a threshold (TOT). This is related logarithmically to the charge, and gives a better signal to noise ratio than measuring the charge or pulse height. Clusters are formed by grouping adjacent strips which have consistent timing information. It is possible for clusters that are separated by one strip to be merged together. Clusters are then passed to an algorithm with pattern recognition abilities, which then interprets the data. The position of hits are expressed in terms of the position of the silicon sensors within the SVT.

4.2.2 Drift Chamber (DCH)

Drift chamber is the second subsystem from the beam pipe which yields spatial and ionization loss measurements for higher momentum charged particles. It gives tracking information for particles with $0.1 < p_t < 5.0$ GeV/c that travel further than SVT, taking up to 40 measurements of spatial coordinates per track. For the low momemtum particles, it provides particle identification by measurements of ionisation loss, dE/dx, and is the sole provider of particle identification in the extreme forward and backward directions. Particle identification information is particularly important for the tracks with $p_t < 700$ MeV/c and therefore do not reach the principal PID detector, the DIRC. The reconstruction of decay and interaction vertices outside of the SVT volume, for instance the K_s^0 decays, relies solely on the DCH. These features allow the reconstruction of exclusive B and D mesons decays with minimal background. It provides high efficiency precision reconstruction

of charged track momentum and supplements the measurement of angles, impact parameter (with respect to the IP) and dE/dx provided by the SVT.

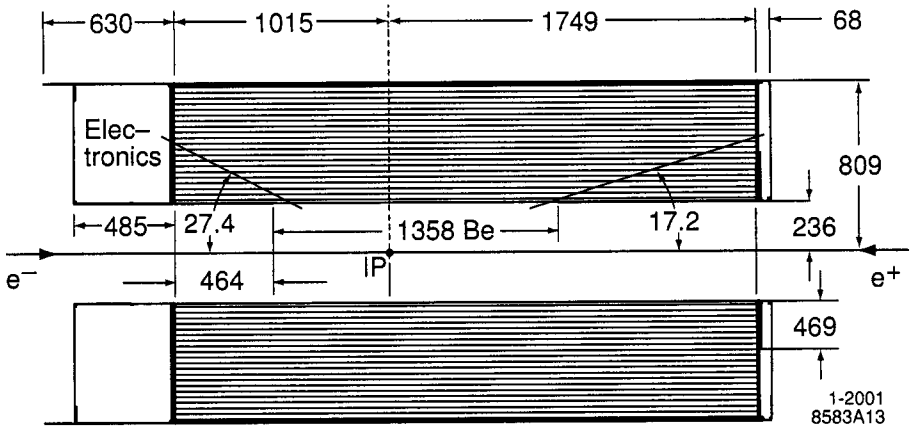

Figure 4.9: *The DCH detector: longitudinal section (all measurements are in mm).*

The DCH features a 2.8m long cylinder which is placed asymmetrically around the IP to provide the forward region with more detector acceptance. The design is shown in Fig. 4.9. It is comprised of 40 radial layers of small hexagonal drift cells. The chamber has an inner radius of 23.6cm and an outer radius of 80.9cm. Multiple scattering is reduced by using low mass wires (some of which are positioned at small angles to the beam axis, to obtain longitudinal information) and by filling the cylinder with helium-based gas mixture (containing helium and isobutane in a 4:1 ratio). Together, the amount of gas and wires form 0.28% of a radiation length for a particle traversing the detector. The endplates of the chamber are constructed using aluminium. The backward plate is 24mm thick, which serves to reduce the amount of material in front of the endcap of the calorimeter.

The 40 cylindrical layers, with a total of 7,104 drift cells, are grouped into 10 superlayers each consisting of four drift cells. Each cell is approximately 1.2cm

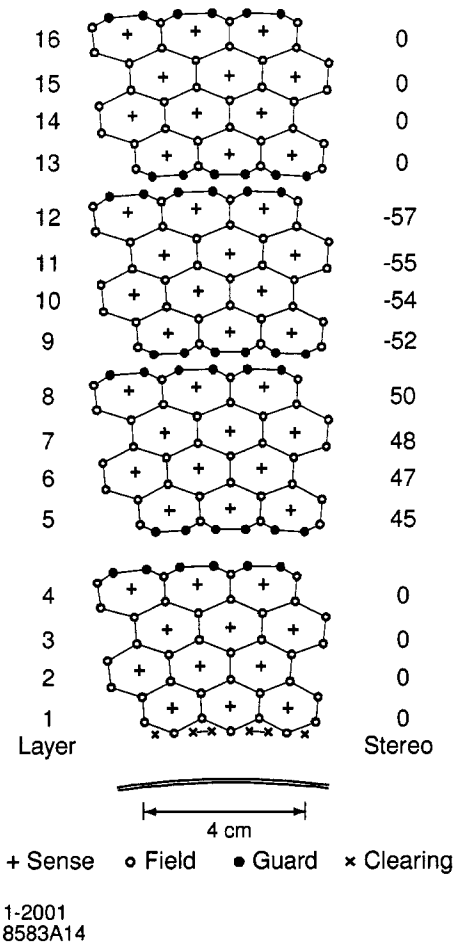

Figure 4.10: *DCH cell layout for the innermost superlayers. Lines have been added between field wires to aid in visualization of the cell boundaries. The right hand column shows the stereo angles of the layers in mrad. The guard wires match the gain in the boundary cells to the gains in the inner layers, and the clearing wires remove charges from the photon conversion in the material of the wall.*

by 1.9cm along the radial and azimuthal directions, respectively, and consists of one sense wire surrounded by six field-shaping wires. The field wires are at ground potential, but a high voltage is applied to the sense wires creating a field with almost circular symmetry over a large portion of the cell. Fig. 4.10 shows the arrangement

of individual field, sense and guard wires into drift cells in the inner four DCH superlayers. Sense wires are currently operated at a nominal voltage of 1930 V and field-shaping wires at 340 V. Passing charged particles ionize the gas and the resultant electrons are accelerated towards the sense wire. An avalanche of charge is created, acting as an amplification of the ionization close to the sense wire for the detector. Longitudinal position information is obtained by placing the wires in 24 of the 40 layers (the "stereo" layers) at slight angles with respect to the z-axis. The superlayers each have one of the three stereo angles. There are axial (A), positive and negative (U,V) stereo layers in the order AUVAUVAUVA. The stereo angles range between ±45mrad in the innermost layers, and to ±76mrad in the outer layers. This structure helps the fast local segment finder which is required by the trigger.

The total amount of charge collected in the DCH by a traversing charged particle is proportional to the energy loss. The measurements are then corrected for effects (such as changes in gas pressure and temperature, differences in cell geometry, etc.) that tend to bias or degrade the accuracy of the measurement. Fig. 4.11 shows DCH dE/dx distribution as a function of both momentum and particle species and the overlaid curves show the corresponding Bethe-Bloch predictions [64]. Fig. 4.12 shows the degree of separation in dE/dx for kaon and pion candidates in a few momentum ranges. The zero of the horizontal axis is the expected dE/dx value for a kaon averaged over all momenta accessible at *BABAR*. It can be seen from this Figure that only relatively soft kaon and pion tracks, below $\approx$ 700 MeV/c (top plot), can be distinguished by the use of dE/dx alone. Information from the DIRC is required to differentiate the various charged hadron species above this threshold value. Also only DCH by itself, has difficulty separating pions from electrons and

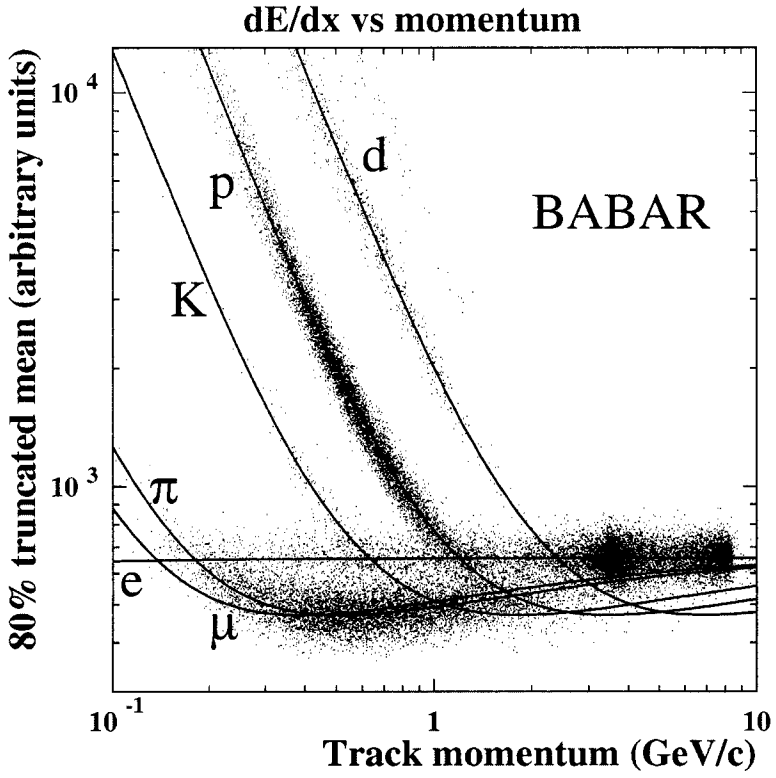

Figure 4.11: *Measurement of specific energy loss ionization (dE/dx) in the DCH as a function of track momenta. The data include large samples of beam background triggers, as evident from the high rate of protons. The curves show the Bethe-Bloch corresponding predictions.*

muons.

4.2.3 Detector of Internally Reflected Cerenkov Light (DIRC)

The DIRC, acronym for Detector of Internally Reflected Cerenkov Light is a unique Cerenkov based detector dedicated to charged particle identification (PID). It was specifically designed to provide excellent discrimination of kaons and pions from the

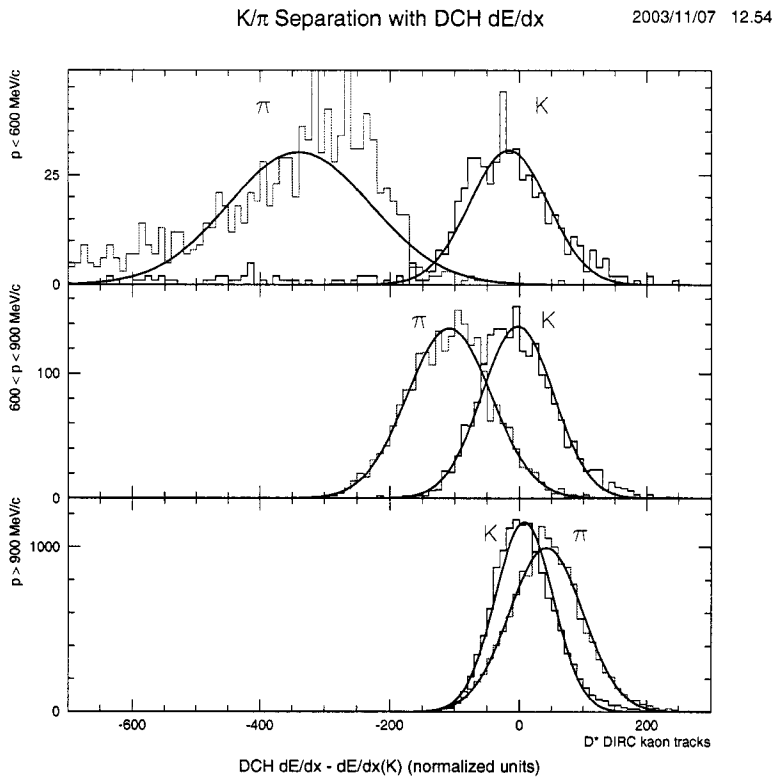

Figure 4.12: *Distribution of DCH dE/dx for high-purity kaons and pions obtained from control samples, showing kaon/pion separation in three different momentum regions: $p < 600$ MeV/c (top), $600 < p < 900$ MeV/c (middle), $p > 900$ MeV/c (bottom).*

turn-on threshold of ≈ 0.7 GeV/c up to ≈ 4.2 GeV/c at large dip angles (the angle between the track momentum vector and the x-y plane) in the laboratory frame.

The DIRC is premised upon the detection of Cerenkov photons trapped in its radiator due to total internal reflection. Cerenkov light is produced when particles with velocity $\beta > 1/n$ traverse a material of refractive index n. The radiation produced has a characteristic Cerenkov angle given by $\cos\theta_c = 1/n\beta$. The radiator is

constructed from long quartz bars of synthetic fused silica, which have $n = 1.472$. The bars are 17mm thick and their rectangular cross-section is 35mm wide in ϕ, and 4.9m long. They are grouped into sets of 12 and are contained in bar boxes. An air gap is maintained between the bars in theses boxes to ensure optical isolation as shown in the longitudinal view of the DIRC in Fig. 4.13. There are 12 bar boxes giving a total of 144 silica bars. The DIRC extends through the solenoid flux in the

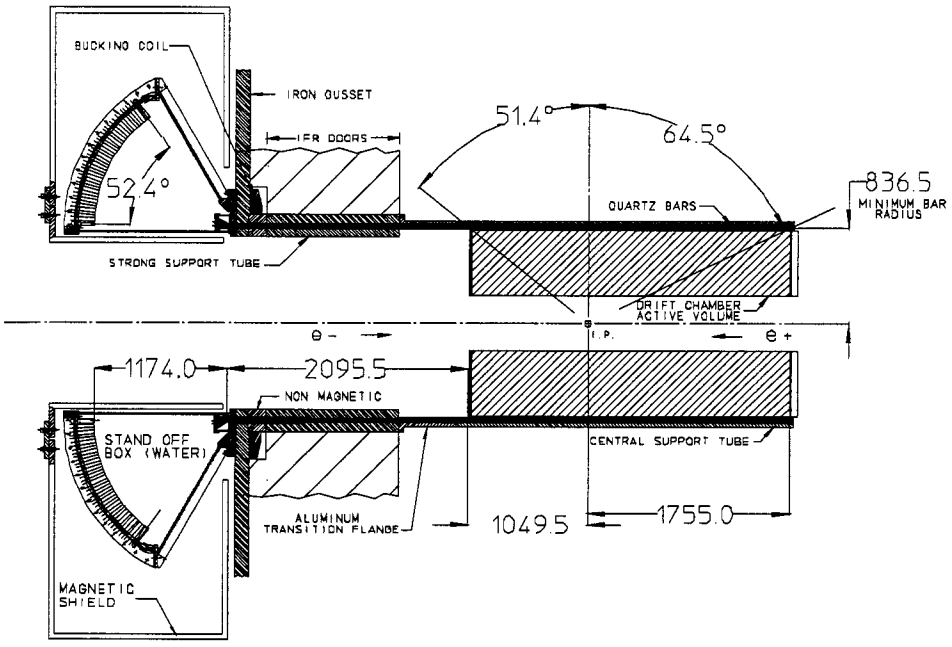

Figure 4.13: *The DIRC: longitudinal view (all dimensions are in mm).*

backwards direction, transporting the Cerenkov radiation, outside of the tracking and magnetic sensors using successive total internal reflections, to an array of nearly 11,000 photomultiplier tubes (PMTs) arrayed on a roughly toroidal surface about 1.2 m from the bar ends. A mirror, perpendicular to the bar axis, is placed at the forward end of the bars to reflect the forward travelling photons to the backward end of the bars where the instrumentation is situated. At the instrumented end

of the bar, is a fused silica wedge which reflects photons at large angles to reduce the size of the detection system needed. The DIRC detection system consists of a standoff box (SOB) filled with 6000 liters of purified water, which is chosen as it is inexpensive and has a refractive index almost equal to that of silica and hence reduces the internal reflection at the bar/box interface.

The observed space-time coordinates of the PMT signals are used to recon-

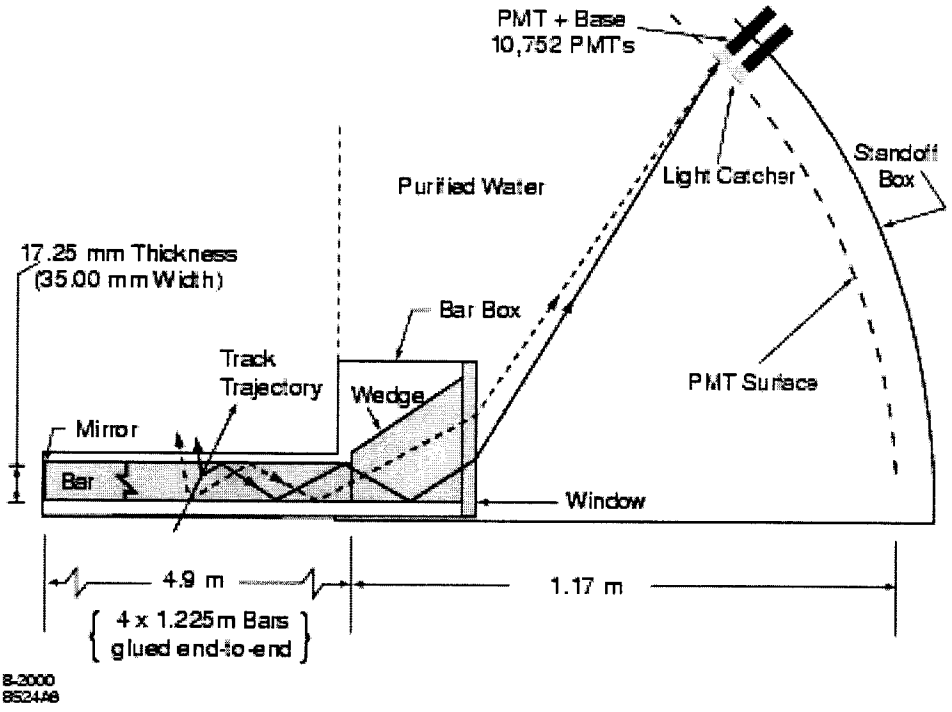

Figure 4.14: *Schematic of the DIRC fused silica radiator bar and standoff box imaging region.*

struct the Cerenkov angle θ_c, the azimuthal angle of a Cerenkov photon with respect to the track direction ϕ_c and the difference Δt between the measured and expected (using track time-of-flight [TOF] information) photon arrival time. These Cerenkov coordinates are then used to reconstruct the emission angle and the arrival time of

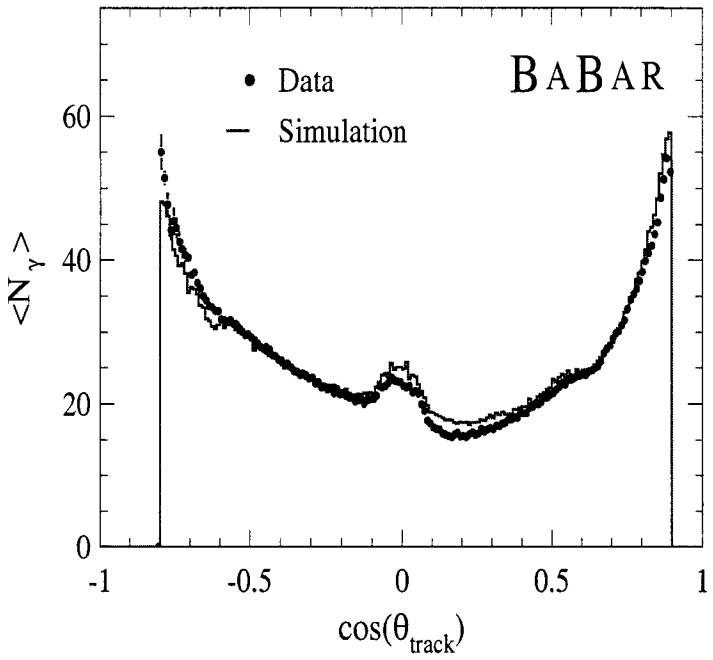

Figure 4.15: *Number of detected photons for reconstructed tracks in di-muon events, plotted as a function of track polar angle.*

Cerenkov photons. The known spatial position of the bar through which the track passed and the PMTs whose signal times lie within ±300ns from the trigger are used to calculate the three-dimensional vector pointing from the center of the bar end to the center of each tube. This vector is then extrapolated into the radiation bar, using Snell's law. Since the track position and angles at the DIRC are known from the charged track reconstruction, the photon propagation angles $\alpha_{x,y,z}$ can be calculated and used to determine θ_c and ϕ_c. The timing information of the PMT signal relative to the track is useful in suppressing photon backgrounds induced by the PEP-II beams, and more importantly, exclude other charged tracks in an event as a possible photon source.

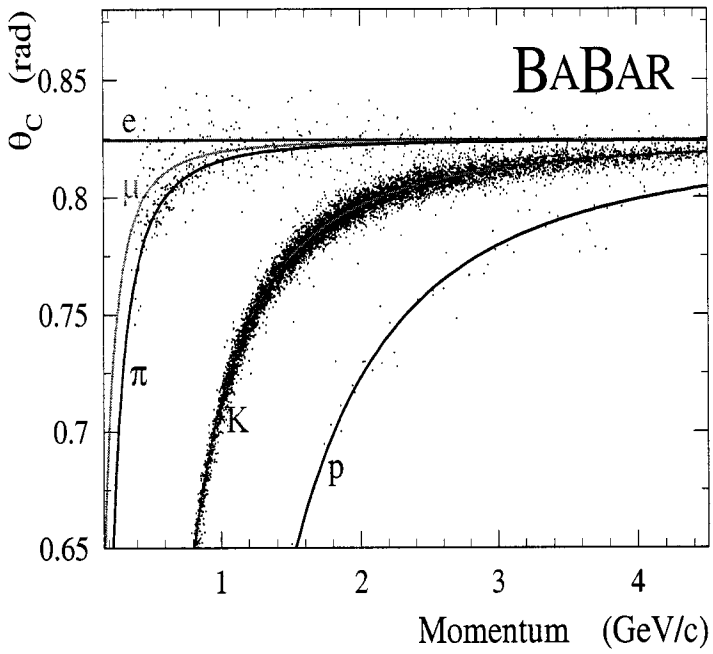

Figure 4.16: *Charged kaon Cerenkov angle as a function of momentum, the data points lying off the "K" curve are due to impurities in the control sample of charged kaons used to make the plot.*

A schematic of the DIRC geometry to illustrate the principles of light production, transportation, and imaging is shown in Fig. 4.14. When a charged particle passes through the radiator bar, a cone of Cerenkov photons is generated. On average, a particle from a *BABAR* event emits about 150 photons per centimeter of quartz traversed. Some of the light exits the quartz, but a portion of it is internally reflected down the length of the quartz bar. On average, 20-50 photons reach the PMTs to form a reconstructible ring. The smaller number generally occurring in the central region of the detector, corresponding to a shorter path length in the quartz radiator and increasing as the track dip angle increases, corresponding to

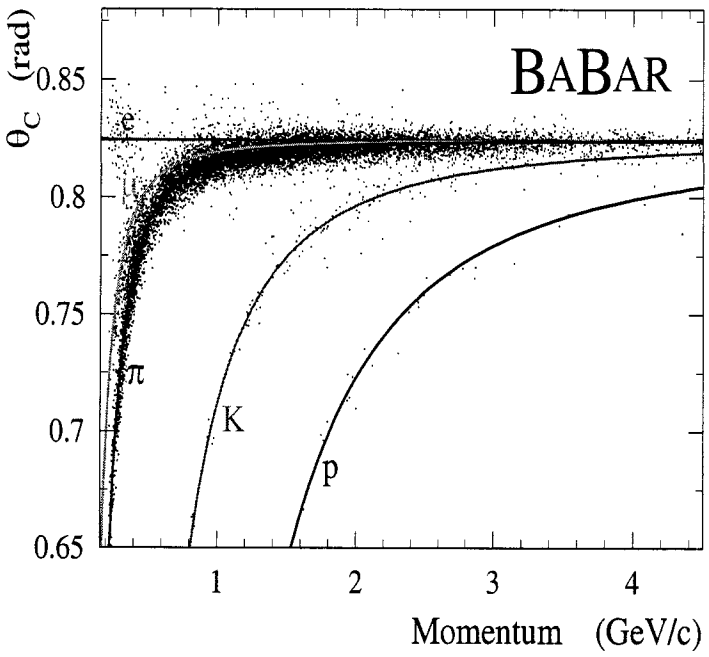

Figure 4.17: *Charged pion Cerenkov angle as a function of momentum, the data points lying off the "π" curve are due to impurities in the control sample of charged pions used to make the plot.*

longer path lengths in the quartz radiator. Fig. 4.15 shows the distribution of the number of signal photons for single muons taken from both simulated and actual di-muon events as a function of polar angle - the excess near $cos(\theta_{track}) = 0$ is due to the existence of both forward- and backward-going Cerenkov photons for tracks which traverse a quartz radiator bar at near-normal incidence. Given the index of refraction, $n \approx 1$, for the medium (nitrogen) surrounding the quartz radiator in the tracking volume, there always are some photons, within the total internal reflection (TIR) limiting angle, and because of the rectangular cross-section of a radiator bar, the magnitude θ_c is preserved during the successive TIRs (modulo a 16-fold reflec-

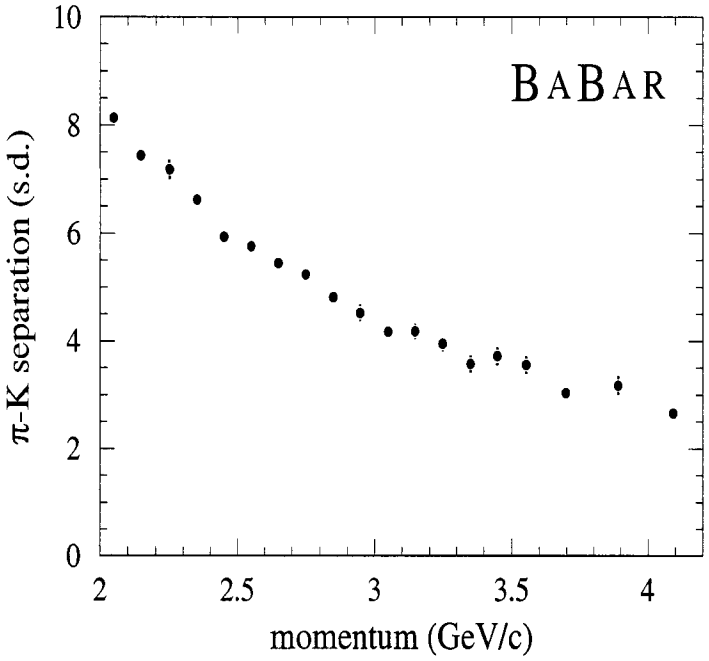

Figure 4.18: *Kaon/pion separation using θ_c, the vertical axis gives the separation in units of θ_c standard deviation.*

tion ambiguity of top/bottom, left/right, forward/backward and wedge /no-wedge reflection)[†]. Therefore in a perfect bar, the portion of the Cerenkov cone that lies within the TIR angle is transported without distortion to the end of the bar. A typical DIRC photon, has a wavelength $\lambda \approx 400$ nm, undergoes ≈ 200 reflections, and has a 10-60ns propagation time along a five meter path through the quartz radiator. The photomultiplier tubes are capable of detecting Cerenkov photons in the visible and near UV-range. The original rings of Cerenkov light are reproduced

[†]Timing information and a requirement to use only physically possible photon propagation paths typically reduces the 16-fold reflection ambiguity down to three, which is then further reduced by the use of a pattern-recognition algorithm.

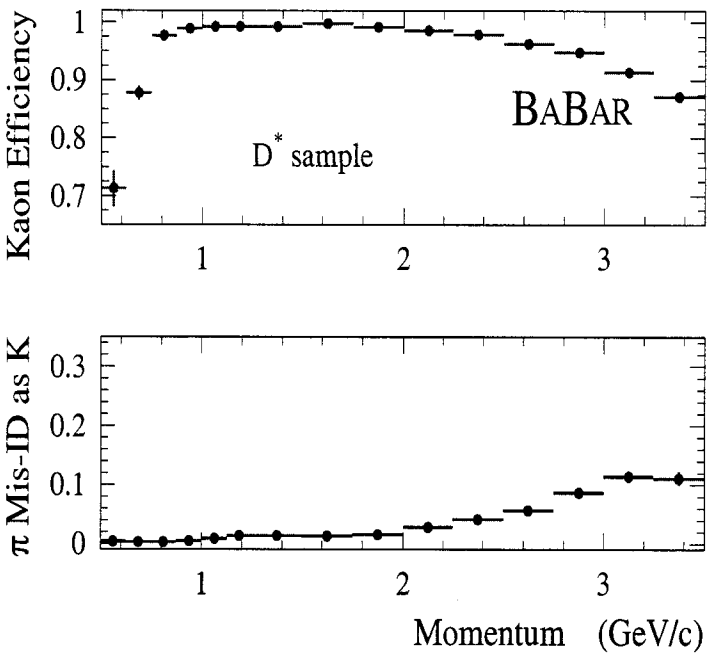

Figure 4.19: *Kaon reconstruction efficiency in DIRC (top); probability to mis-identify a pion as a kaon based on θ_c (bottom).*

using the information about the time and position of the light signals within the bank of photomultipliers. The final photon detection efficiency is about 5%, with the main loss in efficiency being the PMTs which have an efficiency of about 25%.

Figs. 4.16 and 4.17 show the reconstructed Cerenkov angle θ_c for control samples of charged kaons and pions, respectively, as a function of momentum. Based on these θ_c distributions for control samples, we can determine the kaon/pion separation ability of the DIRC as a function of momentum. Fig. 4.18 shows that even at the highest lab momenta accessible at *BABAR*, the DIRC provides around 3σ separation of kaons and pions. In addition to good separation of kaons and pions, the DIRC is also highly efficient, as shown in Fig. 4.19. The plot shows that the reconstruction

efficiency for DIRC rises fairly quickly to its maximum value above the DIRC turn-on threshold of $p > 0.7$ GeV/c, and is well above 90% in general, with a very low probability for pion.

4.2.4 Electromagnetic Calorimeter (EMC)

The electromagnetic calorimeter(EMC) was designed to measure the energy in the electromagnetic showers with excellent efficiency, energy and angular resolution over the energy range of 20 MeV to 9 GeV. 50% of photons from π^0s have energies below 200 MeV and photons from processes $e^+e^- \to e^+e^-\gamma$ and $e^+e^- \to \gamma\gamma$, which are important for calibration and luminosity can reach energies of 9 GeV. Therefore this capability of EMC allows for detection of photons from π^0 and η decays as well as from electromagentic and radiative processes. By identifying electrons and positrons, the EMC contributes to the study of semi-leptonic and rare decays of B and D mesons, and τ leptons. The EMC is a total-absorption calorimeter consisting of a finely segmented array of Thallium doped Cesium Iodide crystals (CsI(Tl)), which scintillate light as charged particles from electromagnetic showers pass through. The material is chosen for its high light yield, short radiation length and small Moliére radius (radius of spread of electromagnetic showers). It provides the necessary energy and angular resolution while allowing shower containment in a short distance. The transverse length of the crystals was chosen to be comparable with the Moliére radius so that a particle traversing the detector will leave energy in several crystals. The EMC is arranged into a cylindrical barrel containing 5760 crystals and a conical forward endcap which contains 820 crystals. This gives complete coverage in azimuthal angle with 90% solid angle coverage in the CM system. The crystals in the barrel are arranged within 48 rings of 120 crystals and

the end-cap has 8 rings of differing size. The length of the crystal increases from 29.6cm in the most backward rings to 32.4cm in the most forward rings, to limit the effects of shower leakage from the more highly energetic forward-going particles. A longitudinal cross-section is shown in Fig. 4.20. The crystals each, have a tapered trapezoidal cross-section with their axes pointing towards the interaction point (IP). In order to obtain the necessary resolution the material in between the crystals is kept to a minimum. This material, as well as beam related background, is what makes the minimum measurable energy in colliding beam data 20 MeV, even though in CsI(Tl) the intrinsic efficiency for photon detection is 100% down to a few MeV. The crystals are read out with silicon photodiodes mounted directly

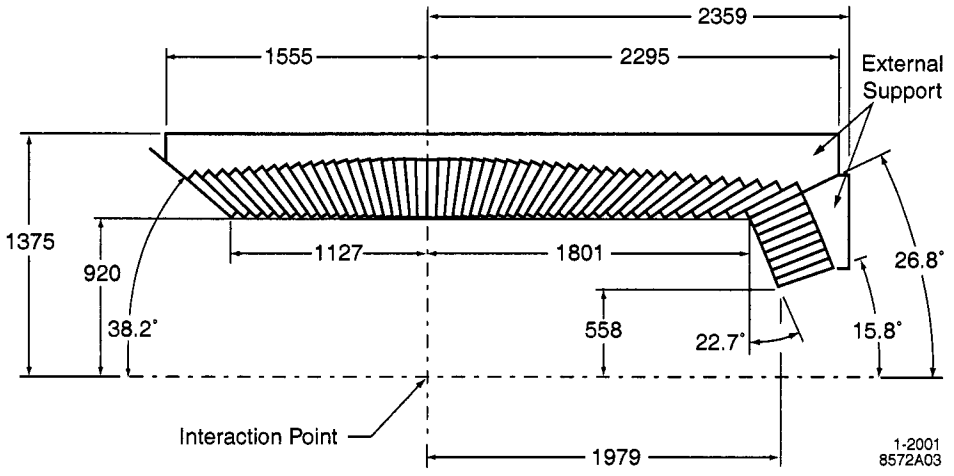

Figure 4.20: *A longitudinal cross-section of the EMC (only top half is shown) indicating the arrangement of the 56 crystal rings. The Detector is axially symmetric around the z-axis. All dimensions are given in mm.*

on the back face of each crystal and each of the diodes is connected to a low-noise preamplifier board mounted directly behind each crystal. Feature extraction algorithms are run to determine the energy and time of the signal peak in the crystal.

To reduce the stored data volume, only the crystals with energy greater than the threshold value of 1 MeV are included. Typical electromagnetic showers spread over many adjacent crystals forming a *cluster* of energy deposits. A cluster is required to register at least one crystal with energy greater than 10 MeV. All surrounding neighbours with energy above 1 MeV and contiguous neighbors (including corners) with at least 3 MeV energy are considered a part of the cluster. The local energy maxima, called *bump*, within each cluster are identified and their energy is determined by an iterative algorithm. The bump is associated with a charged particle track by projecting a track to the inner face of the EMC. The distance between the bump centroid and the track impact point is calculated, and if it is consistent with the angle and momentum of the track, the bump is associated with that charged particle. If it is not possible to associate a cluster with a track projected to the EMC from the DCH, then the cluster is assumed to originate from a neutral particle. On an average, 15.8 clusters are detected per hadronic event, of which 10.2 are not associated with charged particle tracks. EMC is able to separate hadrons from electrons using the electromagnetic shower shapes, energies and track momenta.

The energy resolution of the EMC at low energies is measured directly with the radioactive source, and at high energies it is derived from Bhabha scattering. The empirical parameterization is found to be;

$$\frac{\sigma E}{E} = \frac{(2.32 \pm 0.30)\%}{E(\text{ GeV })^{\frac{1}{4}}} \oplus (1.85 \pm 0.12)\%$$

where E is the photon energy in GeV. The energy dependent term that dominates at low energies, primarily arises from fluctuations in photon statistics but has contributions from electronics noise and beam backgrounds. The constant term dominating above 1 GeV arises from non-uniformity in light collection, leakage or

absorption in the material between or in front of the crystals. The angular resolution is determined primarily by the transverse crystal size and the distance from the interaction point. The measurement based on the analyses of π^0 and η decays to two photons of approximately equal energy results in the energy dependence given by

$$\sigma_\theta = \frac{(3.87 \pm 0.07)}{\sqrt{(E(\text{ GeV }))}} \oplus (0.00 \pm 0.04) \text{ mrad}$$

The π^0 mass resolution, at lower energies, below 2 GeV is dominated by the energy resolution, while at higher energies it is dominated by the angular resolution.

4.2.5 Superconducting Coil

The *BABAR* magnet system consists of a superconducting coil between the EMC and most of the Instrumented Flux Return, creating a magnetic field of 1.5T. Two of the layers for Instrumented Flux Return are placed before the magnet and the rest after it. This magnetic field enables good momentum resolution for charged particles, serves as the hadron absorber for hadron/muon separation, whilst keeping the tracking volume and EMC cost to a minimum. The magnet has an inner radius of 1.4m for the coiled dewar and a cryostat length of 3.85m. The coil and the cryostat together have a total thickness of between 0.25 and 0.4 interaction lengths. This is thin enough to allow neutral hadrons to pass through reasonably well.

4.2.6 Instrumented Flux Return (IFR)

The Instrumented Flux Return (IFR) is the outermost part of the detector. It was designed to detect neutral hadrons and identify muons with high efficiency over a wide range of angles and momenta along with high background rejection for

muons down to momenta below 1 GeV/c. It consists of three parts; barrel, and a forward and backward endcap. All of them are subdivided into sextants. The active detectors are 806 Resistive Plate Chambers (RPC), located in the gaps between the layers of steel. There are 19 RPC layers in the barrel, 18 layers in the endcaps and 2 additional layers of cylindrical RPCs placed between the EMC and the magnet to provide the necessary information, for linking tracks from the EMC to the IFR. The steel is segmented into 18 plates, increasing in thickness from 2cm for the inner plates to 10cm for the outermost plates. The total area of the detector is 2000m^2. The RPCs are built using two bakelite (a phenolic polymer) sheets, each 2mm deep,

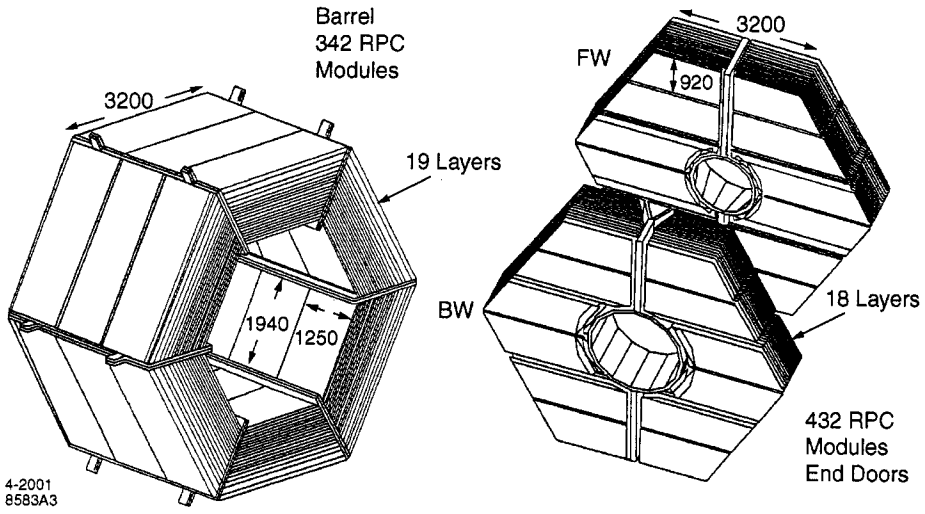

Figure 4.21: *The IFR: Barrel sectors and forward (FW) and backward (BW) endcaps; all dimensions are in mm.*

separated by a 2mm gap, which is filled with a gas mixture. This non-flammable gas mixture is composed of 56.7% Argon, 38.8% Freon-134a, and 4.5% Isobutane. The external surfaces of the sheets are coated with graphite and one is connected

to a 8kV voltage supply whilst the other is grounded, so that an ionizing particle crossing the gas gap will produce a quenched discharge. Orthogonal aluminium readout strips are placed on the modules to measure both z and ϕ for the barrel modules and x and y for the endcap modules.

The IFR is efficient at detecting particles with $p_t > 0.4$ GeV/c. In order to penetrate completely through the detector, a particle must have $p_t > 0.7$ GeV/c. The particle type is determined by using many different information such as the number of interaction lengths passed through by the particle, the matching of tracks to RPC clusters and the distribution of RPCs hit in the IFR layers. The majority of the tracks entering the IFR are muons, though pions may punch through the calorimeter and produce fake muon signals. A muon detection efficiency of close to 90% has been achieved in the momentum range of $1.5 < p < 3.0$ GeV/c with a fake rate of pions of about 6 - 8%. $K_L^0$and other neutral hadrons are identified as clusters that are not associated with a charged track. The inner layers of IFR detect showers resulting from hadrons.

In summer 2005, the RPC's in barrel region were replaced with Limited Streamer Tubes (LST). It was done to improve the muon identification because barrel provides 50% of the muon acceptance and was suffering from inadequate material. The depth of muon/hadron separation was insufficient, which required a highly efficient outer layer and the RPC layer 19 was dying and not accessible. Therefore it was replaced by a mechanically more robust LST.

4.2.7 Trigger (TRG)

The trigger system is designed to select interesting physics events, to be used in either analysis, diagnostic, or calibration studies, while rejecting background events.

The basic background are the Bhabha events (which have a very high rate compared to other physics rates), radiative Bhabha events, beam backgrounds and low mass two-photon events. The *BABAR* trigger system is implemented in two stages. The Level-1 trigger (L1) is hardware based and is followed by the Level-3 trigger (L3) which is software based. The PEP-II bunch crossing rate is around 238MHz (4.2ns bunch spacing). The L1 reduces the event rate to the order of kHz which is the maximum rate allowed by the data acquisition system (DAQ). The L3 further reduces the rate to order of 100Hz which is the upper limit set by storage and reconstruction considerations. Both the levels comprise of a drift chamber trigger (DCT), an electromagnetic trigger (EMT).

The L1 has another subsystem; an instrumented flux return trigger (IFT), which along with DCT and EMT is connected to global level trigger (GLT). The DCT and EMT form the trigger primitives which are summaries of the position and energy of the particles present, while IFT is mainly used to select cosmic ray muons for calibration and diagnostics. There are 3 DCT primitives which correspond to short tracks, long tracks and high p_t tracks. The EMT primitives consist of towers, which are the summed energy of groups of calorimeter crystals. Different energy thresholds are applied to these towers to form 5 EMT primitives. Raw information is used by L1 to form rough tracks and energy clusters and if an event has several tracks in the DCH, especially tracks that are back-to-back, or several clusters in the EMC, it will pass L1. Additionally, if clusters are found in the same azimuthal region as tracks, an event is more likely to pass. Cuts are very loose in L1, resulting in an efficiency greater than 90% for physics events ($>$ 99% for hadronic events). L1 is effective at reducing beam backgrounds by looking at tracks which come from the IP in r and ϕ and also looking at EMT towers. Typical event rates out of L1 are $\sim$ 3-4 kHz,

with a latency of about 12 μs.

The L3 recieves the L1 output and implements improved tracking and clustering procedures which allow for greater rejection of backgrounds. L3 has access to complete event data including timing information, using which it carries out a complete analysis based on simple track cluster topologies and is able to discriminate out-of-time noise and beam backgrounds. The DCT requires one high p_t track or two low p_t tracks originating from the interaction point and for EMT, either a large number of clusters or a large amount of deposited energy throughout the detector is required for acceptance. The trigger lines are prescaled to keep the rate under control, which is especially necessary for processes with high cross-sections, such as Bhabhas which are used for calibration purposes and luminosity measurements. The average event processing time in L3 is 8.5ms. The final output of the trigger system is roughly $\sim$ 200 Hz, the efficiency for selecting events for analysis varies from 90% for $\tau^+\tau^-$ events to 99% for $B\overline{B}$ events. For a luminosity of $2.6\times10^{33}cm^{-2}s^{-1}$, desired physics events (hadrons, $\tau\tau$ and $\mu\mu$) contribute about 16Hz which is approximately 13% of the L3 output. QED and two-photon events contribute around 11% while calibration and diagnostic samples contribute around 40%.

4.3 Data Sample

PEP-II has performed excellently since May 1999 and as of July 31, 2004 a total integrated luminosity of 244.06 fb^{-1} has been recorded by *BABAR* - of this total, 221.38 fb^{-1} have been collected on the $\Upsilon(4S)$ resonance and 22.68 fb^{-1} have been collected $\approx$ 40-50 MeV below the resonance (Fig. 4.22). The peak luminosity for PEP-II was recorded to be 1×10^{34} cm^{-2}s^{-1} on October 9, 2005, which is 3.3 times

higher than the luminosity it was designed to produce. Higher luminosity means generating more collisions per second, which translates into more accurate results and the ability to find physics effects that cannot be seen otherwise. Fig. 4.23 shows the daily recorded luminosity history of the experiment over the entire 1999-2004 running period. The off-resonance data at a lower energy is useful for the B physics

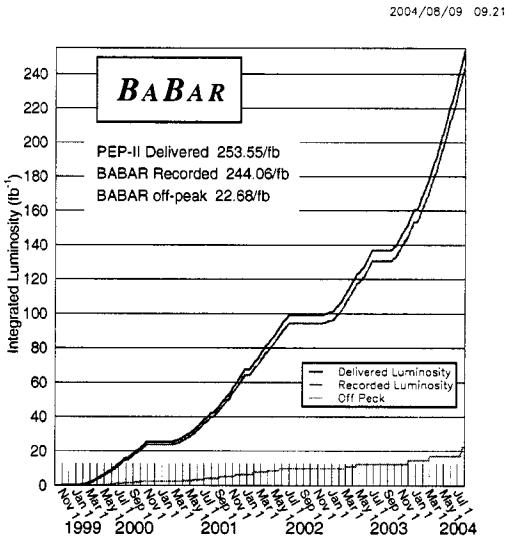

Figure 4.22: *Total integrated luminosity.*

analysis, to characterize backgrounds from continuum events but, for non B-physics, it is an integral part of the total dataset. Charm processes from continuum events are not affected by the presence of the $\Upsilon(4S)$ resonance, and therefore, the on- and off-resonance data are treated identically. The ~ 230 fb^{-1} data sample used in the present analysis (Table 4.3) was collected beginning with the first colliding beams physics runs in 1999 and ending with the July 2005 shutdown of the B-Factory for upgrade and repairs. During that time, the number of B and $\overline{B}$'s produced was estimated to be around 231807371. The Table 4.3 [65] shows the luminosity values for each Run.

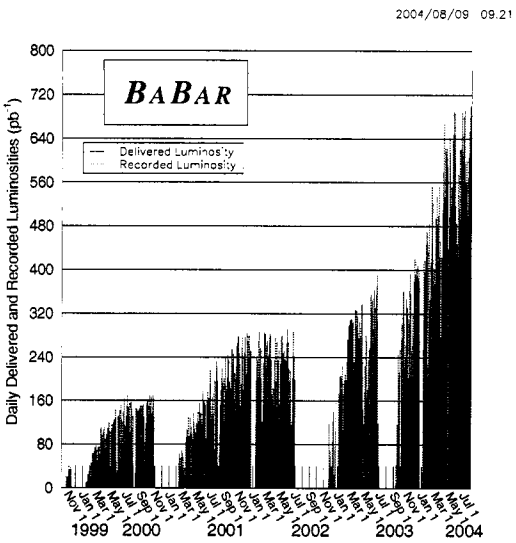

Figure 4.23: *Daily recorded luminosity.*

Table 4.2: Composition of the data sample – the small amount of data from 1999 is include in the value for 2000.

Run No.	Data Year	Integrated Luminosity (fb^{-1})	
		On-Res	Off-Res
1	Oct 22, 1999 - Oct 28, 2000	19.459	2.330
2	Feb 10, 2001 - Jun 30, 2002	60.267	6.934
3	Dec 08, 2002 - Jun 30, 2003	31.061	2.403
4	Sep 2003 - July 31, 2004	99.763	9.937
Total		210.55	21.604

Chapter 5

Particle Tracking and Identification

5.1 Charged Particle Tracking

Charged particle tracking has been studied with large samples of cosmic ray muons, e^+e^-, $\mu^+\mu^-$and $\tau^+\tau^-$ events as well as multi-hadrons. Charged tracks are defined by five parameters and these parameters are measured at the point of closest approach to the z-axis (POCA).

- d_0 : distance of the POCA from the origin of the co-ordinate system in the x-y plane,
- z_0 : distance of the POCA from the origin along the z-axis,
- ϕ_0 : azimuthal angle of the track at POCA,
- λ : dip angle relative to the transverse plane at POCA, and
- $\omega = \frac{1}{p_t}$: curvature of the track.

The sign of ω depends on the charge of the track.

5.1.1 Tracks Reconstruction

Charged particles are reconstructed using data from both tracking system, the SVT and the DCH. The track fitting and finding procedures make use of a Kalman filter algorithm [66], which takes into account the detailed detector material, magnetic field and the information available from the L3 trigger and tracking system. The track reconstruction begins by improving the event start time t_0, obtained from a fit to the parameters d_0, ϕ_0, and t_0 based on the four-hit track segments in the DCH superlayers. Next, tracks are selected by performing helix fits to the hits found by L3 track finding algorithm. While t_0 is further improved by using hits associated with the tracks, a search for additional hits in the DCH which may belong to these tracks is performed. Two more tracking procedures, which are designed to find tracks that do not originate from the interaction point or pass through all ten superlayers of the DCH are applied. These algorithms benefit from a cleaner tracking environment by using tracks segments that have not been assigned to other tracks with a constantly improving t_0. At the end of the third procedure, tracks are again fit using the Kalman filter method.

The resulting tracks are then extrapolated into the SVT. The track segments that are consistent with the expected error in the extrapolation through the intervening material and inhomogeneous magnetic field are added to the reconstructed tracks in the DCH. Among the possible SVT segments, those with the smallest residuals and the largest number of SVT layers are retained and a Kalman fit is performed to a full set of DCH and SVT hits. Any remaining SVT hits are then passed to two complementary stand-alone track finding algorithms. The first one reconstructs

tracks, starting with triplets of space points (matched ϕ and z hits) in layers 1, 3 and 5 of the SVT and adding consistent space points from the other layers. A minimum of four space points are required to form a good track. This algorithm is efficient over a wide range of d_0 and z_0 values. The second algorithm starts with circle trajectories from ϕ hits and then adds z hits to form helices. This one is less sensitive to large combinatorics and to missing z information for some of the SVT modules. Thus the scattered tracks are recovered with an attempt to combine tracks that are only found by one of the two tracking systems.

5.1.2 Tracking Efficiency

The efficiency for reconstructing tracks has been measured as a function of transverse momentum, and polar and azimuthal angles in multi-track events. The tracking efficiency is determined as the ratio of the number of reconstructed DCH tracks to the number of tracks detected in the SVT, with the requirement that they fall within the acceptance of the DCH. Such studies have been performed for multi-hadron events [67]. At the design voltage of 1960V, the efficiency averages (98 $\pm$1)% per track with transverse momentum greater than 200MeV/c and polar angle $\theta > 0.5$ as shown in Fig. 5.1.

5.1.3 Track Parameter Resolutions

The resolution for five track parameters is measured using events with e^+e^- and $\mu^+\mu^-$ pairs. Cosmic rays and multi-hadron events are another source for providing such measurements. The tracks of cosmic ray muons traversing close enough to the interaction point in the DCH and SVT are recorded. The upper and lower

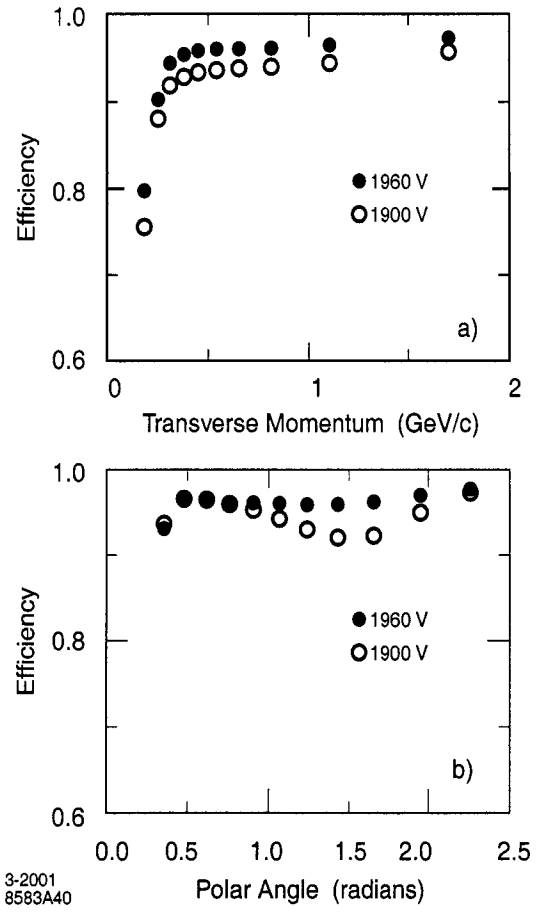

Figure 5.1: *Charged track reconstruction efficiency in the DCH at operating voltages of 1900V (open points) and 1960V (filled points) as a function of transverse momentum (top) and polar angle (bottom). The efficiency is measured in multi-hadron events as the fraction of all tracks detected in the SVT for which the DCH track segment is also reconstructed.*

halves are fit as two separate tracks and the resolution is taken as the difference of the measured parameters for the two track halves. The results of this comparison for the coordinates of the point of closest approach and the angles are given in Fig. 5.2 [67]. The resolutions for single tracks based on full width at half maximum

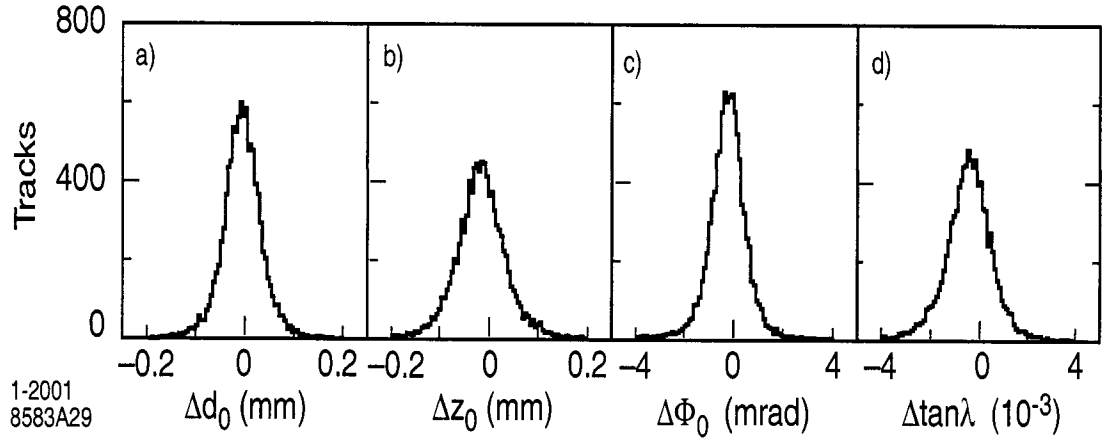

Figure 5.2: *Measurements of the differences between the fitted parameters of the two halves of cosmic ray muon tracks with transverse momenta above 3* GeV/c.

of these distributions are;

$$\sigma_{d_0} = 23\ \mu\text{m}, \qquad \sigma_{\phi_0} = 0.43\ \text{mrad},$$
$$\sigma_{z_0} = 29\ \mu\text{m}, \qquad \sigma_{tan\lambda} = 0.53 \times 10^{-3}.$$

The dependence of the resolution in the coordinates d_0 and z_0 on the transverse momentum p_t is measured in multi-hadron events. The resolution is determined as the width of the distribution of the difference between the measured parameters, d_0 and z_0, and the coordinates of the vertex reconstructed from the remaining tracks in the event. Measurements of the position and angle near IP are dominated by the SVT measurements. The DCH contributes primarily to the p_t measurement.

5.1.4 Track Quality

All reconstructed tracks are categorized into different lists depending on track quality parameters. The lists are provided by Offline Prompt Reconstruction (OPR) according to the following criteria [68]:

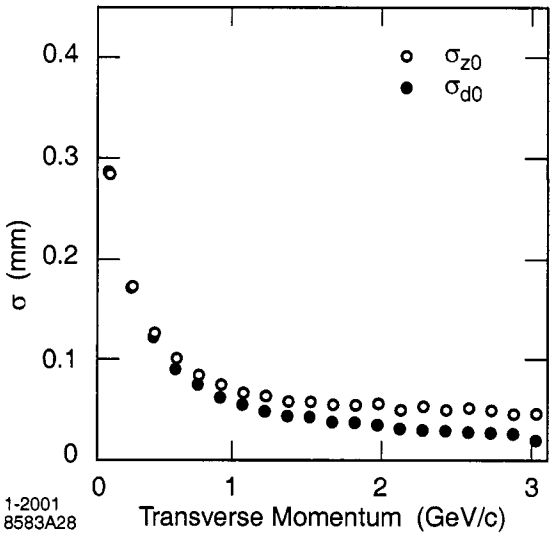

Figure 5.3: *Resolution of the parameters d_0 and z_0 as a function of transverse momentum, measured in multi-hadron events.*

1. `ChargedTracks`:

   Candidates with non-zero charge and with the pion mass hypothesis.

2. `ChargedTracksAcc`:

   Candidates belonging to `ChargedTracks` with

   * $0.41 < \theta < 2.54$

3. `GoodTracksVeryLoose`:

   Candidates belonging to `ChargedTracks` with

   * $0 < p_t < 10\,\mathrm{GeV}/c$;

   * $\mathrm{DOCA}_{xy} < 1.5$ cm*;

   * -10 cm $<\mathrm{DOCA}_z <$ 10 cm.

*DOCA: Distance of closest approach of a track to the beam spot center

4. `GoodTracksLoose`:

   Candidates belonging to `GoodTracksVeryLoose` with

   * $p_t > 0.1$ GeV/c;

   * Minimum DCH Hits: 12.

5. `GoodTracksAccLoose`:

   Candidates belonging to `GoodTracksLoose` with

   * 0.410 rad $< \theta <$ 2.54 rad.

6. `GoodTracksTight`:

   Candidates belonging to `GoodTracksLoose` with

   * Minimum DCH Hits: 20.

   * $\mathrm{DOCA}_{xy} < 1$ cm.

   * -3 cm $<\mathrm{DOCA}_z <$ 3 cm.

5.2 Charged Particle Identification

There are five types of charged particles that are sufficiently long-lived to leave a track in the detector. These are e, μ, π, $K$and p. All *BABAR* detector components contribute in a complementary way to charged particle identification: the SVT and the DCH provide dE/dx measurements; the DIRC is a Cerenkov ring-imaging device which helps to determine the speeds of charged particles; the EMC discriminates electrons, muons and hadrons according to their energy deposit and their shower shape; and the IFR characterizes muons and hadrons according to their different transverse and longitudinal interaction pattern in the segmented iron.

We are using Likelihood based selectors for particles in our analysis. For this selector, the software for particle identification is structured in two stages: first, the information from each detector is analyzed independently to provide a response, in terms of a likelihood and a confidence level, for each charged particle hypothesis, without performing any selection. Then algorithms combining the information from various detectors are applied to perform particle selections.

The LH for track is calculated for each detector for a given charged-particle hypothesis h [69]. These are then normalized to the maximum likelihood of one. For each detector a minimum value called floor value is assigned, which acts to limit a detector's ability to discriminate too strongly against a hypothesis. Any normalized likelihood value below the floor value is set to the floor value. The floor value not only protects against detector malfunctions that might lead to very small likelihood values, but also adds tails to the idealized likelihood functions used to calculate them. All five likelihoods for a given hypothesis are multiplied together along with an apriori likelihood for each hypothesis [69];

$$\mathcal{LH}(h) = \mathcal{LH}_{SVT}(h) \times \mathcal{LH}_{DCH}(h) \times \mathcal{LH}_{DIRC}(h) \times \mathcal{LH}_{EMC}(h) \times \mathcal{LH}_{IFR}(h) \times \mathcal{LH}^{apriori}(h)$$

$$\mathcal{L}(h) = \mathcal{L}^{apriori}(h) \times \prod_{d=SVT}^{IFR} max(\mathcal{L}^{floor}(d), \mathcal{L}^{opr}(d,h))$$

5.2.1 Likelihood Calculations

Both in SVT and DCH, the measured dE/dx is compared against the expected dE/dx from the Bethe-Bloch parameterization. The only difference is that DCH likelihood is based on a Gaussian PDF and the SVT likelihood is based on a Bifurcated Gaussian PDF given as;

$$\exp^{(} \frac{(ln(dE/dx_{meas}) - ln(dE/dx_{th}))^2}{2\sigma\sqrt{5/N}})$$

where $\sigma = \sigma_L$ for $dE/dx_{meas} < dE/dx_{th}$ and $\sigma = \sigma_R$ for $dE/dx_{meas} > dE/dx_{th}$. N is the number of SVT layers. The left-side and right-side standard deviations of the asymmetric Gaussian are fixed parameters. These standard deviations are calculated for five measured dE/dx samples, and they are inflated slightly for tracks with fewer samples to account for a wider spread in the truncated mean.

At least 3 of 5 SVT layers are required to provide dE/dx information, otherwise, SVT likelihood is assumed to be the same for all particle types. To mitigate the effects of Landau fluctuations, only the smallest 60% of the dE/dx values are used to calculate the mean dE/dx for a track. For five samples, the lowest 3 values are used for the average; in case of four samples the 3rd lowest value is given a weight of 40% when averaged with the lowest two values. The expected dE/dx is found from a five-parameter Bethe-Bloch equation, using the momentum of the fit to the considered hypothesis;

$$\frac{dE}{dx} = 4\pi r_e^2 m_e c^2 N_A \frac{Z}{A}\frac{1}{\beta^2}\left[\frac{1}{2}ln\left(\frac{2m_e c^2\gamma^2\beta^2 T_{max}}{I^2} - \frac{\delta}{2}\right)\right]$$

where x is a density-corrected length with units g/cm^2, r_e and m_e are electron's classical radius and mass, c is the speed of light, N_A is Avogadro's number, Z is the charge of incoming particle, A is the atomic number of the absorber, β and γ are the relativistic quantities of the incoming particle, I is the mean excitation energy, δ is density effect correction and T_{max} is maximum transition kinetic energy.
The DCH likelihood is calculated using;

$$\exp^{(}\frac{(dE/dx_{meas} - dE/dx_{th})^2}{2\sigma})$$

where σ is a complicated function of the measured mean, the number of samples, the RMS of the dE/dx values, and the track hypothesis. In order to mitigate the effects of Landau fluctuations, only the smallest 80% of the samples are used. The expected

value of dE/dx for the truncated mean is calculated from Bethe-Bloch equation, using the reconstructed value of the momentum in the DCH for a given hypothesis. The specific energy loss, dE/dx in the DCH is measured in arbitrary units because a direct calibration is tedious and not necessary for analysis. For reference, tracks with momenta between 0.5 and 5.0 GeV have dE/dx values between 400 and 1500 in these arbitrary units. A dE/dx measurement in a cell is used if the track passes through the inner 95% of the cell area, and at least eight usable cell samples are required to calculate a reliable likelihood.

The DIRC likelihood is calculated using the number of photons detected in the Cerenkov ring and the angle of the Cerenkov cone with respect to the track direction as it enters the DIRC. The likelihood is found by multiplying a Poisson distribution for the measured number of photons and Gaussian distribution for the measured Cerenkov angle;

$$\mathcal{L} = \frac{1}{\sqrt{2\pi}\sigma_C} e^{\frac{\theta_C^{exp} - \theta_C^{meas}}{2\sigma_C}} \times \frac{e^{-N^{exp}}(N^{exp})^{N^{obs}}}{N^{obs}!}$$

A calibration table is created using a large number of reconstructed tracks, which gives the expected number of photons N_{exp}. The expected Cerenkov angle, θ_C^{exp}, is determined using the track momentum at the entrance to the DIRC, and the track mass hypothesis, $\cos(\theta_C) = \frac{1}{n\beta}$ and $\beta = \frac{p}{\sqrt{(pc)^2+(mc^2)^2}}$. The measured Cerenkov angle, θ_C^{meas} and its error σ_C, are calculated from fitting the ring of photons observed in the DIRC PMTs.

The shape of the shower in the EMC can be used to discriminate between muons, electrons and hadrons. Muons generally do not shower in the EMC, but rather ionize as they do in the SVT or DCH. They are visible as tracks consisting of very low energy clusters in the EMC. If a particle is fully captured, it will deposit all of its

energy in the calorimeter, which is given as;

$$E_{depos} = (\gamma - 1)mc^2$$

Thus in case of relativistic particles, the deposited energy is equal to the particle's momentum (times the speed of light). Comparison of the energy of a particle to its momentum leads to the identification of electrons and hadrons. Electrons generally have γ of the order of 100, while for hadrons it is of the order 10 or less.

The IFR is mainly used for the identification of muons, since the majority of muons do not interact heavily with any of the other subdetectors. By matching the hits in the IFR to tracks found by the tracking algorithms, it is possible to detect probable muons. Pions, occasionally do not shower in the EMC or in the magnet, so they appear as hits in the IFR. They are however, expected to interact in the iron of IFR and are more likely to be absorbed. They do not travel through all the layers of the IFR and the number of hit-layers and average number of hits per layer can help discriminate pions. Also, pions are expected to shower widely leading to a large number of hits per layer.

5.2.2 Proton Identification

In the proton likelihood selector a particle is selected by comparing its proton likelihood to that of a pion and kaon, with an electron or muon veto applied to some levels. The likelihood selector has four levels; `VeryLoose, Loose, Tight` and `VeryTight`. The ratio cuts are shown in Table 5.1 [69]. In our analysis we select the `VeryLoose` protons. The efficiency for this selection is above 85%, with a pion fake rate of less than 8% and kaon fake rate varying between 0 to 20% for different momentum ranges.

Table 5.1: Selection criteria for the Proton LH Selector

`VeryLoose`	L(P)/L(K) > 4/3 L(P)/L(π) > 0.5
`Loose`	L(P)/L(K) > 3.0 L(P)/L(π) > 0.5 if p> 0.75 reject tight "PidLHElectronSelector" electrons
`Tight`	L(P)/L(K) > 5.0 L(P)/L(π) > 0.75 if p> 0.75 reject tight "PidLHElectronSelector" electrons
`VeryTight`	L(P)/L(K) > 10.0 L(P)/L(π) > 0.96 if p> 0.75 reject tight "PidLHElectronSelector" electrons and reject tight "PidMuonMicroSelector" muons

5.2.3 Kaon Identification

The kaon information from each of the detectors is limited to particular momentum ranges. Measurement of dE/dx information provides kaon separation below 700 MeV/c, and again above 1.5 GeV/c due to the relativistic rise for pions. The DIRC provides π/K separation above 600 GeV/c.

There are four main selection categories for kaon identification: `NotaPion`, `Loose`, `Tight` and `VeryTight`. The corresponding selection criteria are shown in Table 5.2 [69]. In this analysis we are using `NotaPion` kaon selection and later optimize the signal by making different cuts. The efficiency for this selection is above 85%, with a pion and proton fake rate varying between 0 to 20% for different momentum ranges.

Table 5.2: Kaon ID selection criteria. The momentum cuts to include the likelihood from each detector are also shown. L_i is the likelihood for particle type i. The value r_π represents the ratio of likelihood values. It used as the threshold for selecting the kaon at specific momenta.

	`Loose`	`Tight`
SVT	p < 0.6; p > 1.5 (GeV/c)	p < 0.7 (GeV/c)
DCH	p < 0.6; p > 1.5 (GeV/c)	p < 0.7 (GeV/c)
DIRC	p > 0.6 (GeV/c)	p > 0.6 (GeV/c)
Likelihood	L(K)/L(P) $\geq$ 1;L(K)/L(π) > r_π	L(K)/L(P) > 1;L(K)/ L(π) > r_π
Requirements	p < 2.7 (GeV/c) : r_π =1	p > 2.7 (GeV/c) : r_π =1
	p > 2.7 (GeV/c) : r_π =80	p > 2.7 (GeV/c) : r_π =80
	0.5 < p < 0.7 (GeV/c) : r_π =15	0.5 < p < 0.7 (GeV/c) : r_π =15
	`VeryTight`	`NotaPion`
SVT (GeV/c)	p < 0.6; p > 1.5 (GeV/c)	p < 0.5 (GeV/c)
DCH (GeV/c)	p < 0.6; p > 1.5	(GeV/c) p < 0.6 (GeV/c)
DIRC (GeV/c)	p > 0.6 (GeV/c)	p > 0.6 (GeV/c)
Likelihood	L(K)/L(P) > 1;L(K)/L(P) > r_π	Default = true. Reject if:
Requirements	p < 2.5 (GeV/c) : r_π =3	L(P)/L(π) > r_π ; L(K)/L(π) > r_π
	p > 2.5 (GeV/c) : r_π =200	p $\leq$ 0.5 (GeV/c) : r_π = 0.1
	0.4 < p < 0.7 (GeV/c) : r_π =20	p > 0.5 (GeV/c) : r_π =1. 0

5.2.4 Pion Selection

The pions are selected under the criteria given in Table 5.3 [70]. In this analysis we are using `VeryLoose` pion selection and later optimize the signal by making different cuts. The efficiency for this selection is above 92%, with a kaon and proton fake rate varying between 10 and 30% for different momentum ranges.

Table 5.3: Selection criteria for the Pion LH Selector

`VeryLoose`	L(K)/(L(K)+L(π)) < 0.98 L(P)/(L(P)+L(π)) < 0.98
`Loose`	L(K)/(L(K)+L(π)) < 0.82 L(P)/(L(P)+L(π)) < 0.98 reject tight "PidLHElectronSelector" electrons
`Tight`	L(K)/(L(K)+L(π)) < 0.5 L(P)/(L(P)+L(π)) < 0.98 reject tight "PidLHElectronSelector" electrons
`VeryTight`	L(K)/(L(K)+L(π)) < 0.2 L(P)/(L(P)+L(π)) < 0.5 reject tight "PidLHElectronSelector" electrons and reject tight "PidMuonMicroSelector" muons

5.3 Neutral Tracks

Neutral tracks are reconstructed in IFR and EMC. The main task of the EMC is to measure the energies and positions of charged and neutral clusters (primarily photons and electrons but also e.g.; K_L^0 with the best possible resolution and efficiency over the full energy range. In case of neutral tracks the calorimeter utilizes information on the cluster's total energy and its lateral distribution. The results are used to;

- Reconstruct single photons in radiative decays
- Reconstruct π^0's, (even at high energy, when the photon showers overlap)
- Aid in K_L^0 reconstruction and
- Aid in neutrino reconstruction

A cluster is the energy deposit caused by one or more particles interacting in the calorimeter. The reconstruction of clusters starts from a list of crystals with energy above some threshold, nominally 0.5 MeV. A set of adjacent crystals, with the sum of their energies above some threshold, nominally 20 MeV is considered a cluster. An attempt is made to split clusters into bumps. A bump is created from a local maximum within the cluster, such that it represents the fraction of the cluster energy deposit caused by a single particle interaction. In identifying the bumps, care has to be taken to discount so-called split-offs; shower fluctuations that manifest themselves as additional local maxima in a cluster. Neutral electromagnetic multi-bump clusters can be caused by random overlap of multiple photons or by overlapping photon showers from the decay of a high-energy π^0. For genuine multi-bump clusters, the bump parameters can be unfolded by assigning the proper fractions of energy in shared crystal, using the expected exponential lateral shower profile. It should be noted though that merged π^0's, once identified as such, are better reconstructed from the cluster parameters than from the bump parameters of the individual photons. In order to identify charged and neutral particles, an attempt is made to match geometrical clusters to nearby reconstructed charged tracks found in the tracking detectors, as candidate charged-particle clusters. The neutral clusters thus separated out are put into the following lists [68].

1. `CalorNeutral`:

   Candidates which are single EMC bumps but are not matched with any track. Photon mass hypothesis is assigned.

2. `CalorClusterNeutral`:

   Candidates that are multi-bump neutral clusters or single bumps which are not a part of a cluster which is matched with a track.

3. `NeutralHad`:

   Neutral charge candidates with IFR information, but have not been merged with a track or an EMC bump or cluster.

4. `GoodNeutralLooseAcc`:

   Candidates belonging to `CalorNeutral` with

   * $E_\gamma > 30$ MeV;
   * Lateral Moment ≤ 1.1;
   * $0.410 \text{ rad} < \theta < 2.409 \text{ rad}$.

5. `GoodPhotonLoose`:

   Candidates belonging to `CalorNeutral` with

   * $E_\gamma > 30$ MeV;
   * Lateral Moment ≤ 0.8.

6. `GoodPhotonDefault`:

   Candidates belonging to `GoodPhotonLoose` with

   * $E_\gamma > 100$ MeV;

Chapter 6

Monte Carlo Production

Our goal is to study final states decaying to $\Lambda_c^+\pi^+$and $\Lambda_c^+\pi^-$ using the *BABAR* Monte Carlo simulation framework. The Monte Carlo program will simulate the production mechanism:

$$e^+e^- \rightarrow \gamma^* \rightarrow c\bar{c} \rightarrow \Sigma_c X, \Sigma_c^* X, \Sigma_c^{**} X$$

where Σ_c, $\Sigma_c^*$and Σ_c^{**} stand for $J^P = \frac{1}{2}^+, \frac{3}{2}^+, \frac{5}{2}^+$..... charmed baryon states with Isospin = 1. The decay of each intermediate Σ_c state if as, proceeds:

$$\begin{aligned} \Sigma_c^{++}, \Sigma_c^{*++}, \Sigma_c^{**++} &\rightarrow \Lambda_c^+\pi^+ \\ \Sigma_c^0, \Sigma_c^{*0}, \Sigma_c^{**0} &\rightarrow \Lambda_c^+\pi^- \end{aligned}$$

The production and decay take place inside the *BABAR* detector at a center-of-mass energy 10.58 GeV. All tracks produced in the detector are projected out in three dimensions and all possible interactions with the detector layers are appropriately simulated.

6.1 Production and Fragmentation

We start with e^+e^- annihilations to virtual photons (the mass of the intermediate photon is equal to the sum of two beam energies). The charmed baryons of the type Σ_c (for example) are produced from virtual photons coupling to $c\bar{c}$ pairs. The $c\bar{c}$ pair hadronizes into charmed mesons or baryons. Some examples are given below;

$$e^+e^- \rightarrow \gamma^* \rightarrow c\bar{c} \rightarrow c\bar{c}\ u\bar{u} \rightarrow D^0\overline{D^0}$$

$$e^+e^- \rightarrow \gamma^* \rightarrow c\bar{c} \rightarrow c\bar{c}\ d\bar{d} \rightarrow D^+D^-$$

$$e^+e^- \rightarrow \gamma^* \rightarrow c\bar{c} \rightarrow c\bar{c}\ d\bar{d} \rightarrow D_s^+D_s^-$$

where the second $q\bar{q}$ pair is produced by gluons coupling to the c or $\bar{c}$ quark. The lowest order tree diagrams for the above processes are given in Fig. 6.1. Charmed baryons are produced only if we consider $c\bar{c}$ being produced back to back and light quarks and diquarks being "popped" in between them as shown below;

$$\begin{aligned} e^+e^- \rightarrow \gamma^* \rightarrow c\bar{c} &\rightarrow c\bar{c}\ u\bar{u}\ d\bar{d} \\ &\rightarrow cud\ \overline{cud} \\ &\rightarrow \Lambda_c^+\ \overline{\Lambda}_c^- \end{aligned}$$

One needs to produce diquark pairs to obtain baryons and the production process is more complex in general. Quark pairs continue to be produced until all the energy in the center of mass is used up. A more general form of hadronization, as the process is called, is shown in Fig. 6.1. The details of how $c\bar{c}$ ends up as a bunch of mesons and baryons is determined by the implemented JETSET Lund Model. There are parameters in the model which determine the details of the hadronization.

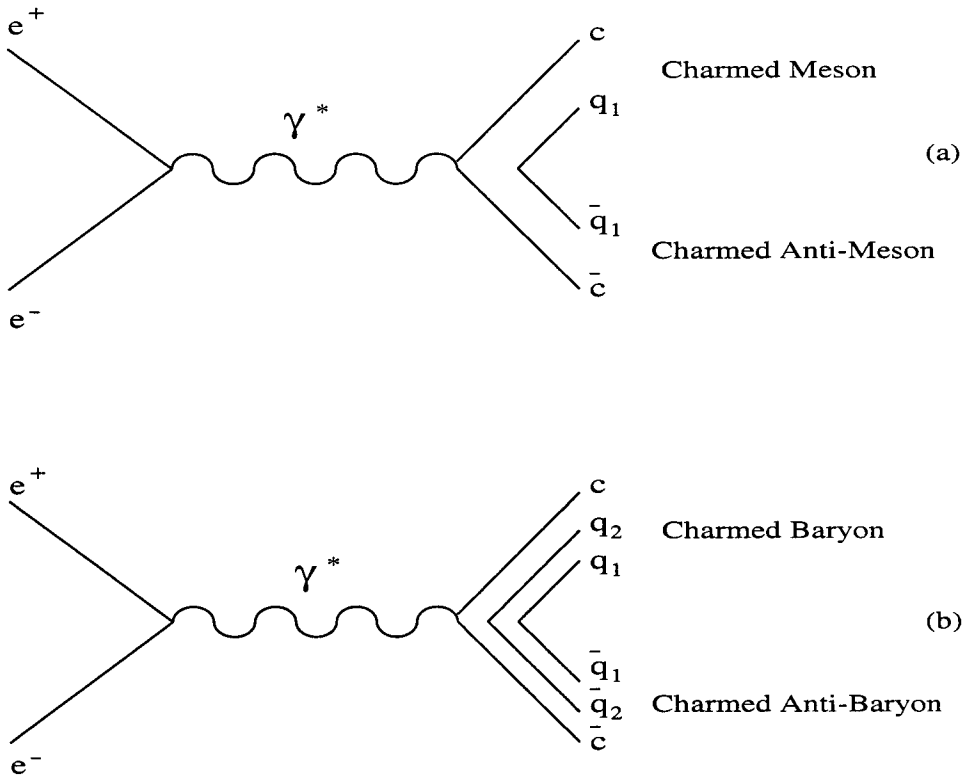

Figure 6.1: *Feynman diagrams of (a) the continuum charmed meson production route via* $e^+e^- \rightarrow c\bar{c} \rightarrow$ Charmed Mesons *and (b), the continuum charmed baryon production route via* $e^+e^- \rightarrow c\bar{c} \rightarrow$ Charmed Baryons.

6.2 JETSET Lund Monte Carlo Model

The *BABAR* MC generator uses JETSET for the production of continuum events. In the signal Monte Carlo for each charge of $\Sigma_c(2800)$ in continuum events at the $\Upsilon(4S)$, the first particle created is the virtual photon γ^* whose further coupling is governed by the parameter JSCONT. The flavor of the primary string is given as an argument to the model and 4 means a $c\bar{c}$. The primary jets are created according to a $1 + cos^2\theta$ distribution, where θ is the angle of the primary jet with respect to the beam line or more precisely, the z-axis. The following code allows γ^* to couple to $c\bar{c}$ 100% of the time.

```
Decay vpho
  1.0  JSCONT 4;
Enddecay
```

In order to generate a particle inclusively using JETSET, we need to go through the following steps.

6.2.1 Defining the Fragmentation Function

The JETSET fragmentation by default is governed by the Lund symmetric fragmentation function given as;

$$f(z) \propto \frac{1}{z} z^{a_\alpha} \left(\frac{1-z}{z}\right)^{a_\beta} \exp\left(-\frac{bm_\perp^2}{z}\right), \tag{6.1}$$

where α and β are the two (di)quarks involved in the fragmentation and z is the momentum of the particle produced, which is $\Sigma_c(2800)$ in our case. For heavier quarks (in *BABAR*'s case, just charm quarks) this equation can be modified to the Bowler fragmentation function given by;

$$f(z) \propto \frac{1}{z^{1+r_Q bm_Q^2}} z^{a_\alpha} \left(\frac{1-z}{z}\right)^{a_\beta} \exp\left(-\frac{bm_\perp^2}{z}\right), \tag{6.2}$$

where Q is the heavy quark. The default value of r_Q used in *BABAR* is $r_Q = 1$.

JETSET also allows usage of Field-Feynman parameterization, Peterson parameterization or a simple power law. For these equations, please see page 231 in the JETSET manual Ref. [71].

JETSET uses the same parameters $a_\alpha = a_\beta = a$ for all quarks and has a optional modification for diquarks. However, as can be seen on page 10 of Ref. [72], that might not be a good enough model of nature. The p^* distributions for D_s^{*+} and D^{*0} look quite different and JETSET is not capable of reproducing that, except through different decay rates of higher resonances. To improve on this, a *BABAR* extension allows to specify the fragmentation function and parameters separately for each charm-anti(di)quark combination, where the anti(di)quark is one half of the pair being produced in the string fragmentation. Note that the fragmentation function for charmed-hadrons with the same quark content, such as D^0 and D^{*0}, will be the same, as the specific hadron type is only determined after the fragmentation. Similarly, if the fragmentation of $D^{(*)+}$ is changed, it will also affect $D^{(*)0}$ due to decays, such as $D^{*+} \to D^0\pi^+$. The twelve different (di)quark combinations with a c quark are listed in Table 6.1. By default all of the combinations use the default JETSET fragmentation (Bowler), but for combination number i, this can be changed by setting `MBBR(i)` > 0. The possible values for i are given in Table 6.2. The actual value of `MBBR(i)` determines which fragmentation function is used.

If a flavor specific fragmentation mode has been selected, one needs to specify the relevant parameters in `PBBR(5 + 5 · i + j)`, where $j = 1 \ldots 5$. Table 6.3 lists the meaning of the five different parameters which can be set. Note that there

Number	(di)quark
1	d
2	u
3	s
4	ud_0
5	sd_0
4	ud_0
5	sd_0
6	su_0
7	dd_1
8	ud_1
9	uu_1
10	sd_1
11	su_1
12	ss_1

Table 6.1: Enumeration of (di)quark combination used in charm fragmentation.

Model number	Fragmentation model
1	Lund symmetric fragmentation
2 (or 3)	non-Lund model (e.g. Peterson)
4 (or 5)	Bowler

Table 6.2: Choice of fragmentation models.

Parameter (j)	Meaning
1	a_α in Lund and Bowler models
2	a_β in Lund and Bowler models
3	b in Lund and Bowler models
4	r_Q in Bowler model
5	c as for `PARJ(54)` in JETSET:
	$0 \leq c \leq 1$: Parameter in Field-Feynman model
	$-1 \leq c < 0$: Use Peterson with $\varepsilon = -c$
	$c > 1$ or $c < -1$: Power law, see JETSET manual

Table 6.3: Fragmentation model parameters.

are no default value for these, so they have to be specified explicitly. It has been checked that changing the fragmentation model only affects the continuum charm production, e.g.; the B decay spectra remain unchanged.

Examples

Using Peterson fragmentation with $\epsilon = 0.003$ for $D_s^{(*)+}$ mesons requires:

```
JetSetPar MBBR(3)=2
JetSetPar PBBR(25)=-0.003
```

Using Bowler with $a_\alpha = 0.3$, $a_\beta = 0.4$, $b = 0.6$ and $r_Q = 0.95$ for $\Lambda_c^{(*)+}$ baryons requires:

```
JetSetPar MBBR(4)=4
JetSetPar PBBR(26)=0.3
JetSetPar PBBR(27)=0.4
JetSetPar PBBR(28)=0.6
JetSetPar PBBR(29)=0.95
```

6.2.2 Particle Transmogrifier

A significant amount of more or less well-known hadrons are not produced in JETSET, in particular there are no $L = 1$ baryons, such as $\Lambda_c(2880)$ or $\Sigma_c(2800)$ by default. To get an approximate signal Monte Carlo, a "Transmogrifier" is used, which takes a fragmentation produced particle and changes its "Lund ID" appropriately in a user defined fraction of events, while leaving particles in decay chains unchanged. To use it, three parameters need to be specified:

- `MBBR(20)`: Absolute value of Lund ID to be changed
- `MBBR(21)`: Absolute value of Lund ID to be changed into
- `PBBR(1)`: Probability that transformation takes place

The idea behind the transformation probability is to make sure that one rarely gets two transformed particles in the same event.

6.3 $\Sigma_c(2800)$ Signal Monte Carlo

The virtual photon is allowed to decay into $c\bar{c}$ which are then fragmented through JETSET. But since $\Sigma_c(2800)$ are not produced in JETSET, we used "Transmogrifier", which was described earlier. To produce Monte Carlo with $\Sigma_c^{++}(2800)$ we "Transmogrify" Σ_c^{++} and add the following in the "`decay.dec`":

```
JetSetPar MBBR(20)=4222
JetSetPar MBBR(21)=14224
JetSetPar PBBR(1)=0.9
```

Similarly for $\Sigma_c^0(2800)$ we "Transmogrify" Σ_c^0 and have the following in file "`decay.dec`":

```
JetSetPar MBBR(20)=4112
JetSetPar MBBR(21)=14114
JetSetPar PBBR(1)=0.9
```

The $\Sigma_c(2800)$ has a wide intrinsic width, which is taken care of by the JETSET. In JETSET, by default, the hadrons are given a mass distribution according to a non-relativistic Breit-Wigner function, namely:

$$P(m)dm \propto \frac{1}{(m-m_0)^2+\frac{\Gamma^2}{4}}. \tag{6.3}$$

Next we use a Petersen function for the fragmentation of quarks instead of the default one. In that case, the generated momentum distribution is of the form [73];

$$f(z) \propto \frac{1}{z\left(1-\frac{1}{z}-\frac{\epsilon_Q}{1-z}\right)^2}, \tag{6.4}$$

We use an $\epsilon = 0.07$, because we are looking at the continuum production of $\Sigma_c(2800)$'s, which have a harder spectrum compared to being produced in B decays.

Using a Filter

The JETSET fragments the quarks, using the specified fragmentation function, into all kinds of possible mesons and baryons. To get a signal Monte Carlo for a particular particle we need to use a filter and take only the events having our particle of interest. The filter defines a particle list, specifying their names as given in the file "`pdt.table`". To filter on events with $\Sigma_c^{++}(2800)$ we have the following in our "`filter.tcl`" file:

```
module enable GefSelectFilter
talkto GefSelectFilter {
```

```
    BooNew MySc2795++ = GefPdtList

    BooObjects MySc2795++ or Sigma_c(2795)++


    BooNew MyantiSc2795++ = GefPdtList

    BooObjects MyantiSc2795++ or anti-Sigma_c(2795)--


    # compose the filter and set it as a before-transformation-to COM


    BooCompose MultiParticleFilter = or MySc2795++ MyantiSc27950++

    beforeFilter set MultiParticleFilter


}
```

Similarly we have a filter for events with $\Sigma_c^0(2800)$.

Chapter 7

Analysis Procedures

Charmed baryons can be produced from either secondary decays of B mesons or directly from e^+e^- annihilations into $c\bar{c}$ jets from the continuum under and below the $\Upsilon(4S)$ resonance.

The goal of this analysis is to search for higher resonances in the $\Lambda_c^+\pi^-$, and $\Lambda_c^+\pi^+$ system. Based on previous results we also expect to see the $J^P = \frac{1}{2}^+$ $\Sigma_c(2425)$ and $J^P = \frac{3}{2}^+$ $\Sigma_c(2455)$. The $\Sigma_c(2455)$ and $\Sigma_c(2520)$ are quite well known from many different experiments. Belle [26] has recently reported the observation of one of their excited partners $\Sigma_c(2800)$, in three charged modes. We present the evidence of these $\Sigma_c(2800)$ in *BABAR* and the measurements of the mass differences, widths and production cross-sections.

We reconstruct all the $\Lambda_c^+\pi^+$and $\Lambda_c^+\pi^-$combinations from data and search for resonances in the corresponding mass distribution plots. We optimize our signal using signal and generic Monte Carlo. The optimized cuts are then applied to the data which is then used to calculate the mass difference, width and the momentum spectrum.

7.1 Fitting Techniques

The $\Sigma_c(2800)$'s have a wide natural width which is parameterized by a Breit-Wigner function. The shape of a resonance of nominal mass m_0 and nominal width Γ_0 is given by a Breit-Wigner:

$$BW = \frac{\Gamma_0}{(x - m_0)^2 + \Gamma_0^2/4} \tag{7.1}$$

The functional form of the signal shape is a convolution of a Breit-Wigner with a Gaussian resolution function, whose width is determined from signal Monte Carlo. We determine the detector mass resolution function by fitting the generated and reconstructed mass difference distribution. The background function is parameterized by a third order polynomial.

7.2 Event Selection

The production of $\Sigma_c(2800)$ from B decays is kinematically allowed and we need to consider this source besides production from the $c\bar{c}$ continuum. The Σ_c baryons produced from secondary decays of B mesons are kinematically limited to $x_p < 0.5$, where $x_p = \frac{p}{p_{max}} = \frac{p}{\sqrt{E^2+M^2}}$ is the scaled momentum varying from 0.0 to 1.0. Here p is the momentum of $\Sigma_c(2800)$ and p_{max} is the maximum momentum it can have. E is the center-of-mass energy and M is the mass. However, charmed baryons produced from the continuum are characterized by x_p distributions which can be fit to the Peterson function [74], which has a hard spectrum, with about 70% of the production above x_p of 0.4. Since we are focusing on continuum production so our analysis is limited to $x_p > 0.45$. We consider production above 0.5 rather than above 0.4 to reduce combinatorial background more effectively.

Since, the analysis presented here involves a Λ_c in combination with a π, we need to first reconstruct all possible Λ_c candidates. The search starts by reconstructing Λ_c^+ in Cabbibo-favored decay mode,

$$\Lambda_c^+ \rightarrow pK^-\pi^+$$

Since this is the dominant decay with a branching fraction $\approx (5.0 \pm 1.3)\%$ and all the particles are observed as charged tracks, it is the cleanest mode for reconstructing Λ_c^+. The Λ_c candidates are then combined with all the pions in the event to reconstruct the Σ_c candidates. The decay mode used for that is,

$$\Sigma_c^0 \rightarrow \Lambda_c^+ \pi^-$$

$$\Sigma_c^{++} \rightarrow \Lambda_c^+ \pi^+$$

The Σ_c candidates are reconstructed in one decay mode only, because the branching fraction $\mathcal{B}(\Sigma_c \rightarrow \Lambda_c \pi) \approx 100\%$ for $\Sigma_c(2455)$ and $\Sigma_c(2520)$ and for $\Sigma_c(2800)$ it is predicted to be the dominant decay mode [51]. All the charge conjugate modes are implied.

7.2.1 Selection of Λ_c^+ Candidates

Λ_c^+ (charge conjugate is implied) candidates are reconstructed by taking combinations of p, K^-, π^+ candidates and performing a constrained vertex fit. Using composition tools we select the `VeryLoose` lists of protons, kaons and pions, as created by the 'Likelihood Selector', explained already in chapter 5. We present below the initial selection criteria for the Λ_c^+ candidates.

- 2.235 GeV/c^2 $<$ Λ_c mass $<$ 2.335 GeV/c^2
- Proton : pLHVeryLoose

- Kaon : KLHVeryLoose
- Pion : piLHVeryLoose

7.2.2 Selection of Σ_c Candidates

Σ_c candidates are formed by combining the already identified Λ_c candidates selected from Λ_c mass band, which is chosen to be $\pm$ 35 MeV/c^2, with the remaining π's in the event and performing a constrained vertex fit. These pion candidates are chosen from the `piLHVeryLoose` list for the 'PidPionLHSelector' (defined in chapter 5).

7.3 Monte Carlo Study

In order to optimize our signals and determine fit parameters for the Σ_c signals in the two decays modes, we use approximately two samples of 143,000 Monte Carlo simulated signal events for each of the two charges. PID optimization and studies of background shape are performed using Monte Carlo samples of $B\overline{B}$, $c\bar{c}$ and $u\bar{u}/d\bar{d}/s\bar{s}$ equivalent to an integrated luminosity of 230 fb^{-1}. The Monte Carlo samples were produced in simulation production frameworks SP5/SP6 and SP8. For optimization purpose we use an x_p cut of > 0.7 for both the signal and background to suppress the combinatorial background. Later we relax this cut to measure the momentum spectrum and production cross-sections.

7.3.1 Σ_c Optimization

We optimize the Σ_c signal by studying the PID cuts for all the tracks, Λ_c mass cuts and Λ_c vertex fit cuts to achieve the best possible values of the signal significance,

$\frac{S^2}{S+B}$. Here S represents the signal yield of Σ_c candidates obtained by integrating the signal fit function (Breit-Wigner fit convoluted with a Gaussian), and B represents the background count within $\pm 15 \mathrm{MeV/c^2}$. We use 320 fb^{-1} of $c\bar{c}$ and then normalize it to a luminosity of 230 fb^{-1} to extract B. The results of MC PID studies for protons, kaons and pions forming the Λ_c are summarized in Tables 7.1 and 7.2. From these tables we conclude that the "PrVeryTight, KVeryLoose" and "PiLoose" combination gives the best signal significance for both Σ_c charges. Based on this selection we use these PID lists for Λ_c candidates.

The next quantity that we study for optimization is the Λ_c mass window. As summarized in Table 7.3, our study finds an optimal selection of Λ_c candidates for a mass window of Λ_c mass $\pm 11 (\approx 1.5\sigma)$. It gives good significance for both the charges. To suppress the background from random combinations of protons, kaons and pions which do not fit to a good Λ_c vertex, we require the χ^2 of the fit to be less than a certain value. The results for vertex cuts are given in Table 7.4. A minimum χ^2 value of < 30 is required to get rid of very poorly formed Λ_c vertices.

Table 7.1: Signal Significance for different PID cuts for Λ_c Selection.

Proton	Kaon	Pion	$\frac{S^2}{S+B}$	
			Σ_c^0	Σ_c^{++}
PVLoose	KVLoose	PiVLoose	2.17	2.79
PVLoose	KVLoose	PiLoose	2.20	2.83
PVLoose	KVLoose	PiTight	2.19	2.80
PVLoose	KVLoose	PiVTight	2.13	2.72
PVLoose	KLoose	PiVLoose	2.21	2.79
PVLoose	KLoose	PiLoose	2.24	2.83
PVLoose	KLoose	PiTight	2.22	2.80
PVLoose	KLoose	PiVTight	2.16	2.71
PVLoose	KTight	PiVLoose	2.26	2.81
PVLoose	KTight	PiLoose	2.29	2.85
PVLoose	KTight	PiTight	2.27	2.82
PVLoose	KTight	PiVTight	2.21	2.73
PVLoose	KVTight	PiVLoose	2.26	2.81
PVLoose	KVTight	PiLoose	2.29	2.85
PVLoose	KVTight	PiTight	2.28	2.82
PVLoose	KVTight	PiVTight	2.21	2.74
PLoose	KVLoose	PiVLoose	3.07	3.67
PLoose	KVLoose	PiLoose	3.12	3.72
PLoose	KVLoose	PiTight	3.09	3.40
PLoose	KVLoose	PiVTight	3.00	3.89
PLoose	KLoose	PiVLoose	3.07	3.60
PLoose	KLoose	PiLoose	3.11	3.65
PLoose	KLoose	PiTight	3.08	3.61
PLoose	KLoose	PiVTight	2.99	3.48
PLoose	KTight	PiVLoose	3.11	3.59
PLoose	KTight	PiLoose	3.15	3.64
PLoose	KTight	PiTight	3.12	3.60
PLoose	KTight	PiVTight	3.03	3.50
PLoose	KVTight	PiVLoose	3.11	3.59
PLoose	KVTight	PiLoose	3.15	3.64
PLoose	KVTight	PiTight	3.12	3.61
PLoose	KVTight	PiVTight	3.03	3.50

Table 7.2: Signal Significance for different PID cuts for Λ_c Selection.

Proton	Kaon	Pion	$\frac{S^2}{S+B}$	
			Σ_c^0	Σ_c^{++}
PTight	KVLoose	PiVLoose	3.63	4.19
PTight	KVLoose	PiLoose	3.67	4.25
PTight	KVLoose	PiTight	3.64	4.20
PTight	KVLoose	PiVTight	3.54	4.08
PTight	KLoose	PiVLoose	3.60	4.08
PTight	KLoose	PiLoose	3.65	4.13
PTight	KLoose	PiTight	3.61	4.09
PTight	KLoose	PiVTight	3.50	3.97
PTight	KTight	PiVLoose	3.66	4.07
PTight	KTight	PiLoose	3.70	4.12
PTight	KTight	PiTight	3.66	4.08
PTight	KTight	PiVTight	3.55	3.96
PTight	KVTight	PiVLoose	3.66	4.07
PTight	KVTight	PiLoose	3.70	4.12
PTight	KVTight	PiTight	3.66	4.08
PTight	KVTight	PiVTight	3.55	3.96
PVTight	KVLoose	PiVLoose	4.11	4.59
PVTight	KVLoose	PiLoose	4.16	4.65
PVTight	KVLoose	PiTight	4.12	4.60
PVTight	KVLoose	PiVTight	3.99	4.46
PVTight	KLoose	PiVLoose	4.06	4.45
PVTight	KLoose	PiLoose	4.11	4.51
PVTight	KLoose	PiTight	4.06	4.46
PVTight	KLoose	PiVTight	3.93	4.32
PVTight	KTight	PiVLoose	4.13	4.43
PVTight	KTight	PiLoose	4.17	4.49
PVTight	KTight	PiTight	4.12	4.44
PVTight	KTight	PiVTight	3.99	4.31
PVTight	KVTight	PiVLoose	4.13	4.43
PVTight	KVTight	PiLoose	4.17	4.49
PVTight	KVTight	PiTight	4.12	4.44
PVTight	KVTight	PiVTight	3.99	4.31

Table 7.3: Λ_c Mass cuts study for Λ_c selection.

Λ_c Mass Window (MeV/c^2)	$\frac{S^2}{S+B}$	
	Σ_c^0	Σ_c^{++}
2.285 ± 5	5.44	6.94
2.285 ± 7	6.24	7.97
2.285 ± 9	6.49	8.24
2.285 ± 10	6.54	8.20
2.285 ± 11	6.55	8.16
2.285 ± 12	6.52	8.07
2.285 ± 13	6.46	7.96
2.285 ± 15	6.34	7.69
2.285 ± 17	6.19	7.44
2.285 ± 19	6.03	7.18
2.285 ± 21	5.88	6.95
2.285 ± 23	5.72	6.71

† PVTight, KVLoose and PiLoose are used for Λ_c.

Table 7.4: Signal significance of Σ_c candidates for different values of χ^2 of the Λ_c vertex fit.

Λ_c χ^2_{vtx}	$\frac{S^2}{S+B}$	
	Σ_c^0	Σ_c^{++}
< 100	7.05	9.09
< 80	7.07	9.13
< 60	7.09	9.16
< 50	7.10	9.15
< 45	7.09	9.17
< 40	7.09	9.18
< 35	7.09	9.18
< 30	7.10	9.17
< 25	7.09	9.16
< 20	7.05	9.14
< 15	6.99	9.09
< 10	6.78	8.83
< 5	5.67	7.52

After optimizing our Λ_c candidates we study PID cuts for the π candidates, which are combined with Λ_c to form Σ_c candidates. The results of these cuts study are shown in Table 7.5. The "PiLoose" selection optimizes our signal significance for both $\Sigma_c^{++}(2800)$ and $\Sigma_c^0(2800)$. Another important cut that we studied is the helicity angle for the π. The helicity angle is defined to be the angle between π momentum measured in the rest frame of $\Lambda_c\pi$ system and the boost direction of the $\Lambda_c\pi$ system. The study for the cosine values of the helicity angle are given in Table 7.6. A $cos\theta_{hel} > -0.7$ is selected to get rid of low momentum pions.
The final selection cuts after optimization are given below;

- $x_p > 0.7$

Table 7.5: Signal significance for different PID selections of π forming the Σ_c candidates.

Pion PID cuts	$\frac{S^2}{S+B}$	
	Σ_c^0	Σ_c^{++}
PiVeryLoose	7.10	9.17
PiLoose	7.15	9.22
PiTight	7.08	8.93
PiVeryTight	6.73	8.37

Table 7.6: Helicity angle cuts for π forming the Σ_c candidates.

cos θ_{hel}	$\frac{S^2}{S+B}$	
	Σ_c^0	Σ_c^{++}
> -1.0	7.15	9.22
> -0.9	10.06	11.72
> -0.8	11.45	12.87
> -0.7	12.14	13.16
> -0.6	12.12	13.09
> -0.5	11.75	12.85
> -0.4	11.32	12.30
> -0.3	10.75	11.77
> -0.2	10.08	11.14

- Λ_c^+ Proton : pLHVeryTight
- Λ_c^+ Kaon : KLHVeryLoose
- Λ_c^+ Pion : piLHLoose
- 2.274 GeV/c^2 $< \Lambda_c$ mass $<$ 2.296 GeV/c^2
- χ^2 of Λ_c Vertex fit < 30

- Σ_c Pion : piLHLoose
- Σ_c Pion cos $\theta_{hel} > -0.7$

Figs. 7.1 and 7.2 show the mass distribution for the signal Monte Carlo after optimization for $\Sigma_c^0(2800)$ and $\Sigma_c^{++}(2800)$, respectively. The corresponding mass distributions for the background before and after the final optimization are shown in Figs. 7.3 and 7.4. We can see that the background level was more than ten times higher before optimization than the one after optimization.

We also did a separate optimization for Λ_c using $\approx 10\%$ of the data. The results of the study are summarized in Appendix A. We got a somewhat different set of cuts from that optimization, and we decided to use the optimized cuts from Monte Carlo.

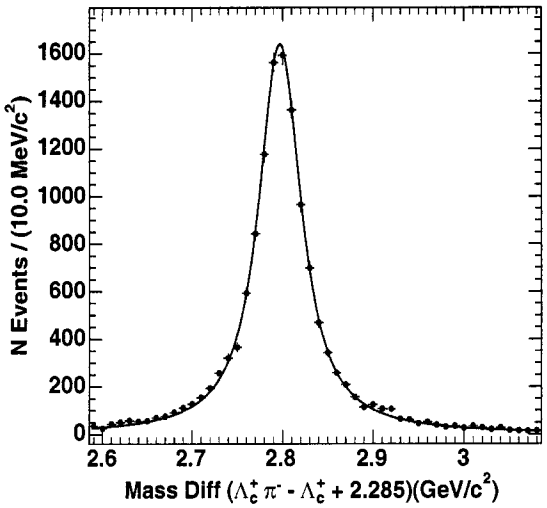

Figure 7.1: *Distribution for the Mass Difference* $(\Lambda_c^+\pi^- - \Lambda_c^+ + 2.285)$ *in signal Monte Carlo after optimization.*

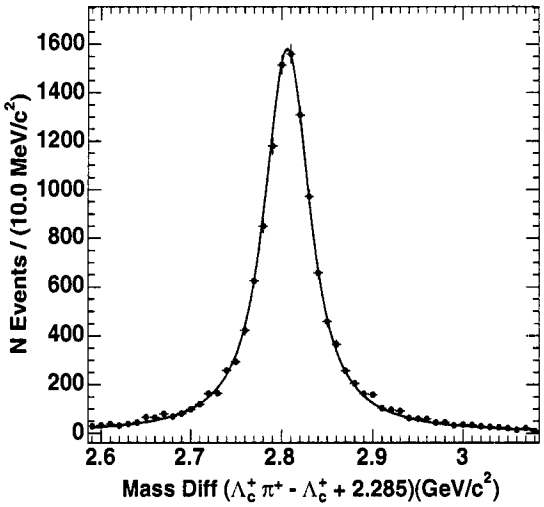

Figure 7.2: *Distribution for the Mass Difference* $(\Lambda_c^+\pi^+ - \Lambda_c^+ + 2.285)$ *in signal Monte Carlo after optimization.*

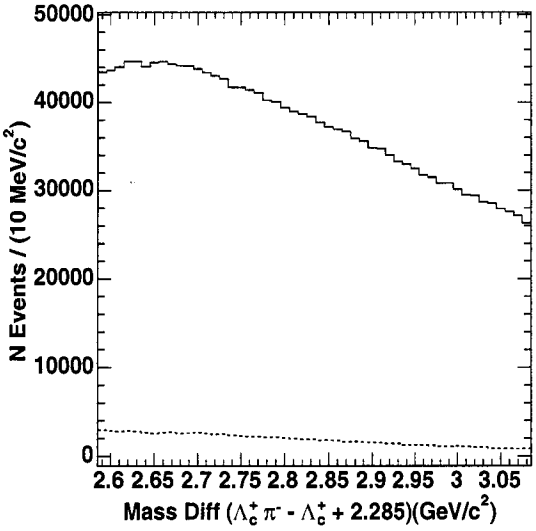

Figure 7.3: *Normalized Background distributions for* $(\Lambda_c^+\pi^- - \Lambda_c^+ + 2.285)$ *in* $c\bar{c}$ *Monte Carlo. The solid and dashed lines show the background level before and after the optimization, respectively.*

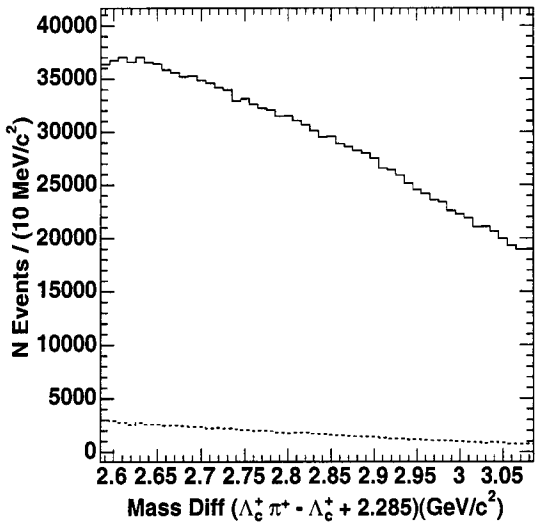

Figure 7.4: *Normalized Background distributions for* $(\Lambda_c^+\pi^+ - \Lambda_c^+ + 2.285)$ *in* $c\bar{c}$ *Monte Carlo. The solid and dashed lines show the background level before and after the optimization, respectively.*

7.3.2 Background from uds and $B\overline{B}$ Monte Carlo

To match the data we need to study the background component coming from $u\bar{u}$, $d\bar{d}$, $s\bar{s}$ and $B\overline{B}$also. For uds, we use 314 fb^{-1} of generic Monte Carlo and then normalize it to our data sample. As expected, we do not see any significant contribution, because it does not contain any heavy quark. The plots are shown in Figs. 7.5 and 7.6. The $B\overline{B}$ generic Monte Carlo is scaled to the number of B's reported in the data. As shown in Figs. 7.7 and 7.8, we just see a small component of flat background with no contribution to the signal.

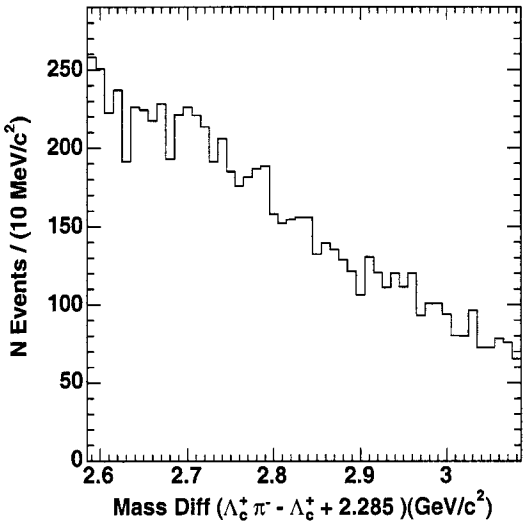

Figure 7.5: *Normalized Mass Difference* $(\Lambda_c^+\pi^- - \Lambda_c^+ + 2.285)$ *distribution in generic uds Monte Carlo.*

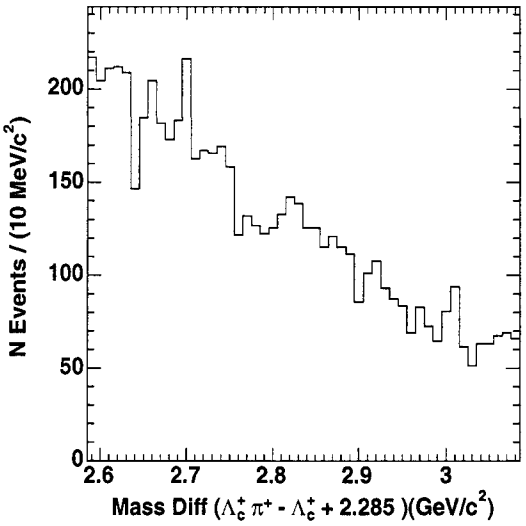

Figure 7.6: *Normalized Mass Difference* $(\Lambda_c^+\pi^+ - \Lambda_c^+ + 2.285)$ *distribution in generic uds Monte Carlo.*

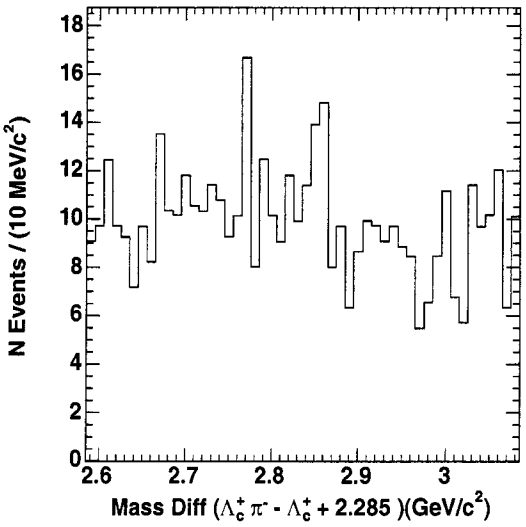

Figure 7.7: *Normalized Mass Difference* $(\Lambda_c^+\pi^- - \Lambda_c^+ + 2.285)$ *distribution in generic* $B\overline{B}$ *Monte Carlo.*

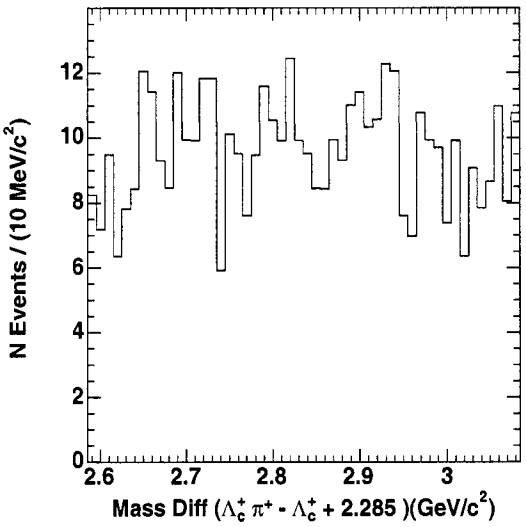

Figure 7.8: *Normalized Mass Difference* $(\Lambda_c^+\pi^+ - \Lambda_c^+ + 2.285)$ *distribution in generic* $B\overline{B}$ *Monte Carlo.*

7.3.3 Efficiency Calculations

The Σ_c detection efficiency is obtained by dividing the signal area by the generated number of Σ_c baryons in the signal Monte Carlo. The signal area is determined by integrating the Breit-Wigner function convoluted with a Gaussian. The efficiency after each selection cut is given in Table 7.7.

To see the momentum dependence of the detection efficiency, we measure the efficiency, using the method described above, for each momentum interval. Errors on efficiency are given by the errors on raw yields for each momentum bin. The efficiency plots, as a function of x_p bins, are shown in Figs. 7.9 and 7.10 for $\Sigma_c^0(2800)$ and $\Sigma_c^{++}(2800)$, respectively. We find that the efficiency is almost constant above our momentum cut of $x_p > 0.7$.

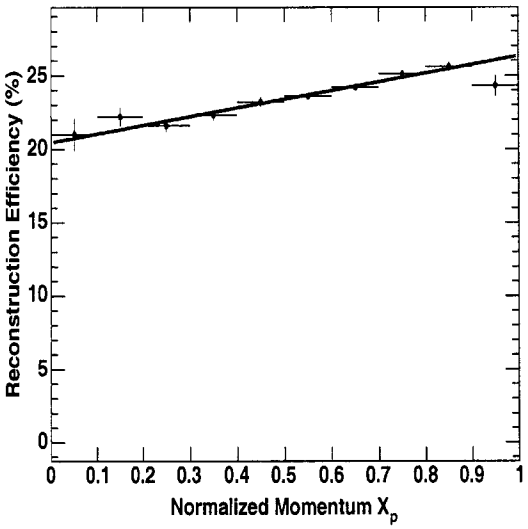

Figure 7.9: *Detection efficiency as a function of x_p for $\Sigma_c^0(2800)$ with a fit to a linear function.*

Table 7.7: Variation in $\Sigma_c(2800)$ detection efficiency with each selection cut.

Pion PID cuts	Efficiency %	
	Σ_c^0	Σ_c^{++}
$x_p > 0.7$	40.9	41.2
Λ_c PrVT, KVL, PiL	34.5	34.5
Λ_c mass $\pm$ 11 MeV/c^2	30.1	30.2
Λ_c $\chi^2_{vtx} < 30$	29.2	29.3
Σ_c : PiLoose	29.0	29.0
Σ_c : πcos $\theta_{hel} > -0.7$	25.5	25.2

7.3.4 Reflection Studies

The mass distribution plots by Belle shown in Fig.3.5 have a peak at a mass difference ($\Lambda_c^+\pi^- - \Lambda_c^+$) of 0.43 GeV/c^2. These were interpreted as feed-down from the

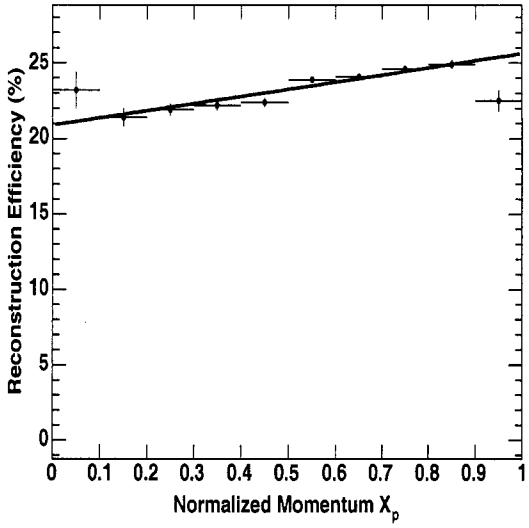

Figure 7.10: *Detection efficiency as a function of x_p for $\Sigma_c^{++}(2800)$ with a fit to a linear function*

decay $\Lambda_c^+(2880) \rightarrow \Lambda_c^+\pi^+\pi^-$, where $\Lambda_c^+(2880)$ decays proceed via an intermediate $\Sigma_c^0(2455)$ or $\Sigma_c^{++}(2455)$. In a MC study Belle found that if $\Lambda_c^+\pi^\pm$ pairs are produced from intermediate $\Sigma_c^{++}(2455)$ or $\Sigma_c^0(2455)$, then the mass difference plot for the $\Lambda_c^+\pi^\mp$ spectrum is peaked around 0.43 GeV/c^2. Expecting the same feed-downs in *BABAR* we use 57k $\Lambda_c^+(2880)$ signal Monte Carlo events for each of the five decay modes, to find the shape of the feed-down. The five decay modes are;

$$\begin{aligned}
\Lambda_c^+(2800) &\rightarrow \Lambda_c^+\pi^+\pi^- \\
&\rightarrow \Sigma_c^0\pi^+ \\
&\rightarrow \Sigma_c^{++}\pi^- \\
&\rightarrow \Sigma_c^{*0}\pi^+ \\
&\rightarrow \Sigma_c^{*++}\pi^-
\end{aligned}$$

where

$$\begin{aligned} \Sigma_c^0 &\rightarrow \Lambda_c^+\pi^- \\ \Sigma_c^{++} &\rightarrow \Lambda_c^+\pi^+ \\ \Lambda_c^+ &\rightarrow pK^-\pi^+ \end{aligned}$$

We found that if we reconstruct $\Lambda_c^+\pi^+$ combinations from the second decay mode involving Σ_c^0 and plot the normalized mass difference $(\Lambda_c^+\pi^+ - \Lambda_c^+ + 2.285\text{GeV/c}^2)$, we see a peak around 2.71 GeV/c^2. Similarly $\Lambda_c^+\pi^-$ combinations from the third decay mode involving Σ_c^{++} give a peak at the same mass value. These plots are shown in Figs. 7.11 and 7.12. All the rest of the decay modes in each case, show no significant signal for both of the $\Lambda_c^+\pi$ combinations. The peaks are fitted with a single Gaussian and a second order polynomial. The fitted mean values are 2.7104 and 2.711 GeV/c^2, and fitted resolutions are 0.01343 and 0.01341 GeV, for $\Lambda_c^+\pi^-$ and $\Lambda_c^+\pi^+$ combinations, respectively.

A separate study is done using data to check for other possible feed downs. For this our reconstructed Σ_c candidates are combined with the γ's in the event. Our results are given in Appendix B. We do not find any significant signal in the $\Sigma_c(2800)$ mass band for γ energies $E_\gamma > 50$ and 100 MeV.

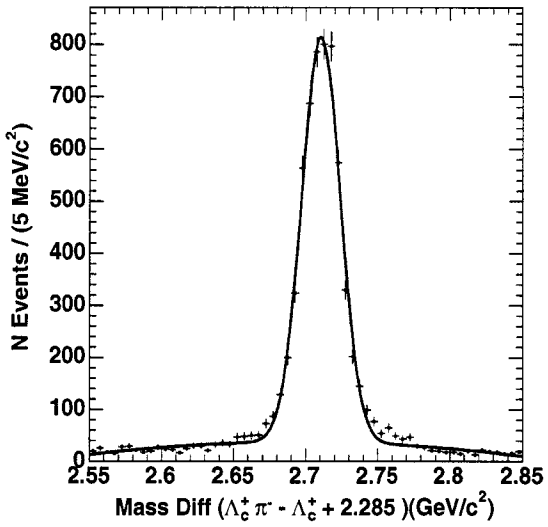

Figure 7.11: $\Lambda_c^+\pi^-$ *combinations from Signal Monte Carlo for* $\Lambda_c^+(2800) \rightarrow \Sigma_c^{++}\pi^-$.

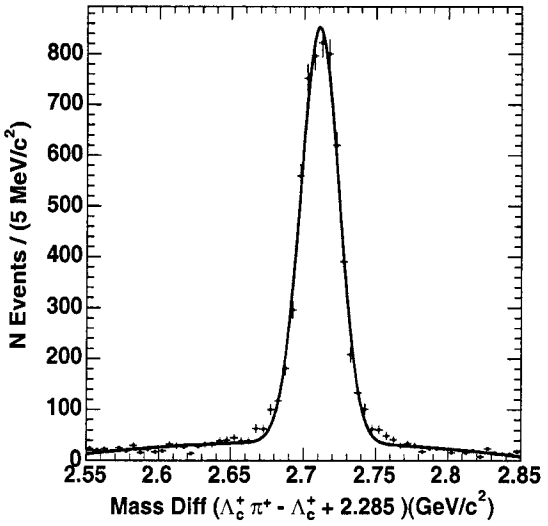

Figure 7.12: $\Lambda_c^+\pi^+$ *combinations from Signal Monte Carlo for* $\Lambda_c^+(2800) \rightarrow \Sigma_c^0\pi^+$.

7.3.5 Detector Resolution

The mass resolution function shape for the signal is determined from the signal Monte Carlo for $\Sigma_c(2800)$ by plotting the difference of generated and reconstructed masses. This resolution function will be convoluted with a Breit-Wigner and will then be used to fit the data. We get a detector resolution of 5.4 MeV for both the charges. The plots for zero and doubly charged Σ_c's are shown in Figs. 7.13 and 7.14, respectively. We also study detector mass resolution as a function of x_p

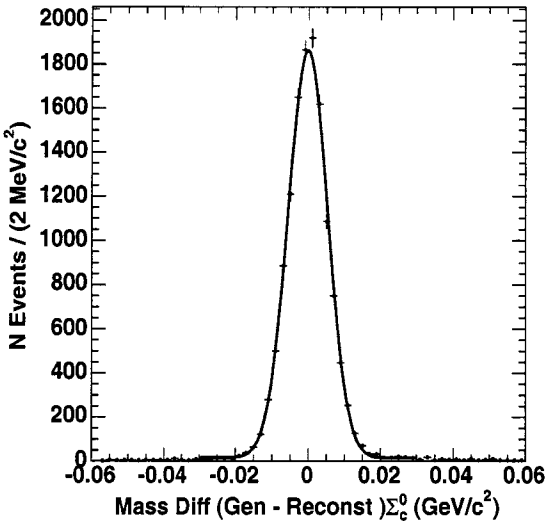

Figure 7.13: *The difference of generated and reconstructed masses from Signal Monte Carlo for* $\Sigma_c^0(2800)$.

bins and do not find it to be sensitive to the x_p values. The detector resolution for different x_p bins is given in Table 7.8.

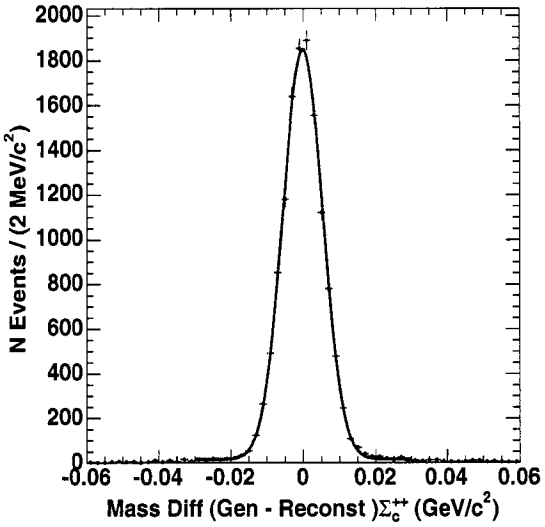

Figure 7.14: *The difference of generated and reconstructed masses from Signal Monte Carlo for* $\Sigma_c^{++}(2800)$.

Table 7.8: Detector resolution for x_p bins.

x_p bins	Det. Mass Res. σ (MeV)	
	Σ_c^0	Σ_c^{++}
$0.5 > x_p \geq 0.6$	5.31 ± 0.06	5.27 ± 0.06
$0.6 > x_p \geq 0.7$	5.24 ± 0.05	5.30 ± 0.05
$0.7 > x_p \geq 0.8$	5.37 ± 0.06	5.43 ± 0.05
$0.8 > x_p \geq 0.9$	5.54 ± 0.07	5.41 ± 0.06
$0.9 > x_p \geq 1.0$	5.22 ± 0.16	5.49 ± 0.19

7.4 Study using the data

As mentioned earlier we use 230 fb^{-1} of data. We apply all of our optimized cuts from the Monte Carlo to the data and look for resonances in $\Lambda_c^+\pi^+$ and $\Lambda_c^+\pi^-$ combinations that fit to a good vertex within a mass range 2.4 to 3.4 GeV/c^2.

7.4.1 Data Sample

The analysis presented here is based on the Λ_c skim created for Runs 1-4. The integrated luminosity values for this data sample are given below.

On Resonance	208.9 fb^{-1}
Off Resonance	21.53 fb^{-1}

We present below the selection criteria for the Λ_c^+ skim.

- 2.235 GeV/c^2< Λ_c mass < 2.335 GeV/c^2
- Proton : pLHVeryLoose
- Kaon : KLHVeryLoose
- Pion : piLHVeryLoose
- Probability of forming a Λ_c Vertex > 0.001

7.4.2 Λ_c^+ Candidates

As mentioned earlier in Section 7.2, $\Sigma_c(2800)$ is reconstructed in the decay mode $\Sigma_c \rightarrow \Lambda_c^+ \pi$. The Λ_c^+ is reconstructed in $\Lambda_c^+ \rightarrow pK^-\pi^+$ mode. The invariant mass distribution for Λ_c^+ candidates is shown in Fig. 7.15. A signal area of 1270100$\pm$5122 events is obtained by fitting the distribution to a double Gaussian over a first order polynomial. The fitted mean value is 2.28588$\pm$0.00001 GeV/c^2. The width (FWHM) of the two Gaussian σ_1 and σ_2 is used to calculate the effective width σ, where $\sigma = \sqrt{f\sigma_1^2 + (1-f)\sigma_2^2}$ and f is the fraction of the first Gaussian. We find σ to be 6.66 MeV. The sidebands are shown with dashed lines in Fig. 7.15.

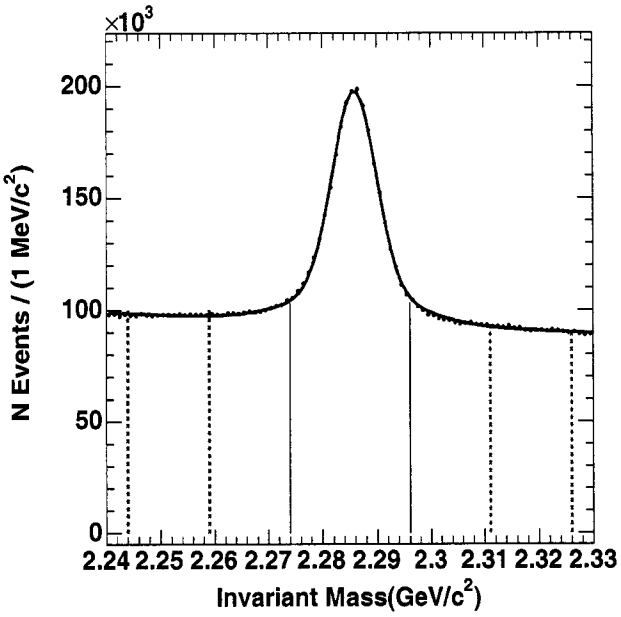

Figure 7.15: *Invariant Mass distribution for Λ_c^+ in data. The solid lines show the signal band and the dashed lines show the sidebands.*

7.4.3 Observation of $\Sigma_c(2455)$ and $\Sigma_c(2520)$

Many experiments have reported the observation of ground state charmed baryons $\Sigma_c(2455)$ and $\Sigma_c(2520)$ decaying to $\Lambda_c^+\pi$. We expect to see these resonances while searching for $\Sigma_c(2800)$. The Λ_c candidates with a reconstructed mass in the signal region ($2.274 < m < 2.296$), shown with solid lines in Fig. 7.15, are combined with a π to reconstruct Σ_c. Using our optimized PID, Λ_c vertex cuts and $x_p > 0.5$, we plot the mass difference distributions for $(\Lambda_c^+\pi^- - \Lambda_c^+ + 2.285)$ and $(\Lambda_c^+\pi^+ - \Lambda_c^+ + 2.285)$ shown in Figs. 7.16 and 7.17. The distributions show peaks around 2.455 GeV/c^2 and 2.520 GeV/c^2.

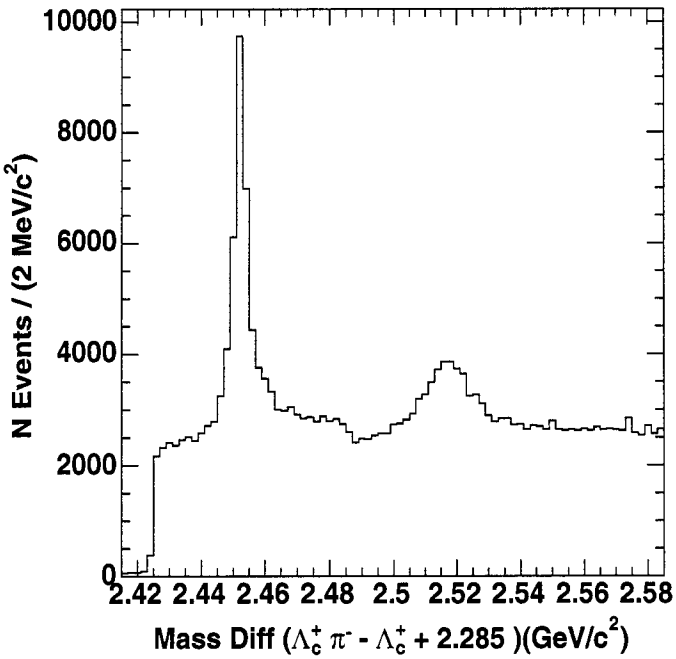

Figure 7.16: *Mass difference distribution* ($\Lambda_c^+\pi^- - \Lambda_c^+ + 2.285$) *for* $\Lambda_c^+\pi^-$ *combinations in data.*

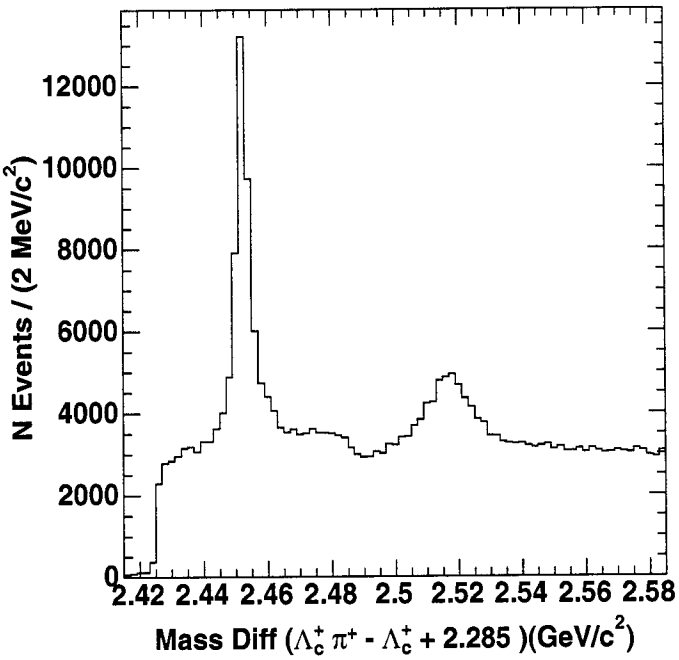

Figure 7.17: *Mass difference distribution* $(\Lambda_c^+\pi^+ - \Lambda_c^+ + 2.285)$ *for* $\Lambda_c^+\pi^+$ *combinations in data.*

7.4.4 Observation of $\Sigma_c(2800)$

As mentioned in the previous section, the Λ_c candidates with a reconstructed mass in the signal region ($2.274 < m < 2.296$), shown with solid lines in Fig. 7.15, are combined with a π to reconstruct Σ_c. All selection criteria for $\Sigma_c^0(2800)$ and $\Sigma_c^{++}(2800)$ candidates described in Section 7.3 are applied. We show the distributions for the mass differences $\Delta M = (\Lambda_c^+\pi^- - \Lambda_c + 2.285)$ and $(\Lambda_c^+\pi^+ - \Lambda_c + 2.285)$ in Figs. 7.18 and 7.19. The scaled Λ_c^+ sidebands ($2.244 < m < 2.259$ and $2.311 < m < 2.326$) shown as histograms, exhibit featureless ΔM distributions.

The distributions are fitted using a Breit-Wigner function convoluted with a Gaussian resolution function. The detector resolution is fixed to the value determined from Monte Carlo i.e; 5.4 MeV. The reflection is fitted with a Gaussian function whose width is fixed to the value obtained from Monte Carlo i.e; 13.4 MeV. A third order polynomial is used to fit the background. The signal yield is defined as the integral of the Breit-Wigner function over the mass interval $2.65\text{GeV/c}^2 < \Delta M < 2.95\text{GeV/c}^2$. We get 3001 ± 578 events for $\Sigma_c^0(2800)$ and 2930 ± 921 for $\Sigma_c^{++}(2800)$. The fitted mean values for the mass difference ΔM are $2.8008 \pm 0.0023\text{GeV/c}^2$ and $2.7980 \pm 0.0028\text{GeV/c}^2$, and the intrinsic widths are found to be 65.6 ± 14.9 MeV and 67.7 ± 16.0 MeV, for the neutral and charged modes, respectively.

In Figs. 7.20 and 7.21, we show the background subtracted distributions in the signal region with the signal component from the fit superimposed. The reflection component is accounted for as a part of the background for subtraction.

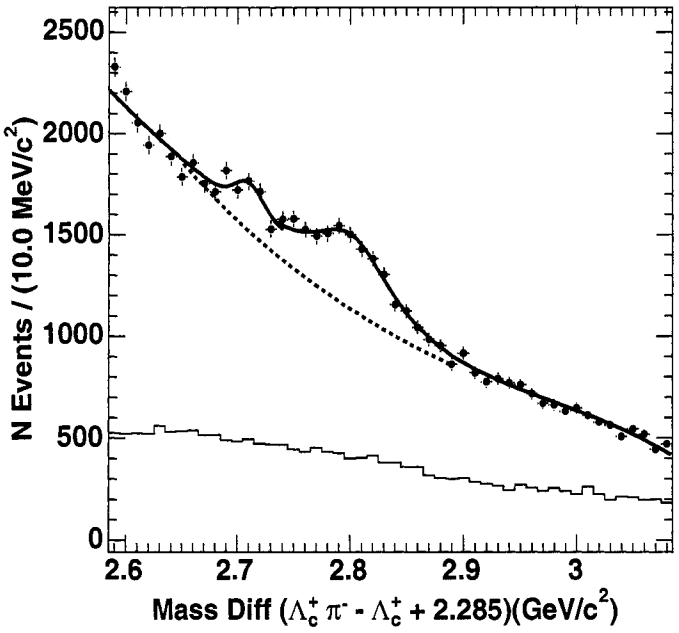

Figure 7.18: *Mass difference distribution* ($\Lambda_c^+\pi^- - \Lambda_c^+ + 2.285$) *for* $\Lambda_c^+\pi^-$ *combinations in data. The* Λ_c^+ *signal window (points with error bars) and normalized sidebands (histograms) are shown, together with the fits described in the text (solid curves) and their combinatorial background components (dashed).*

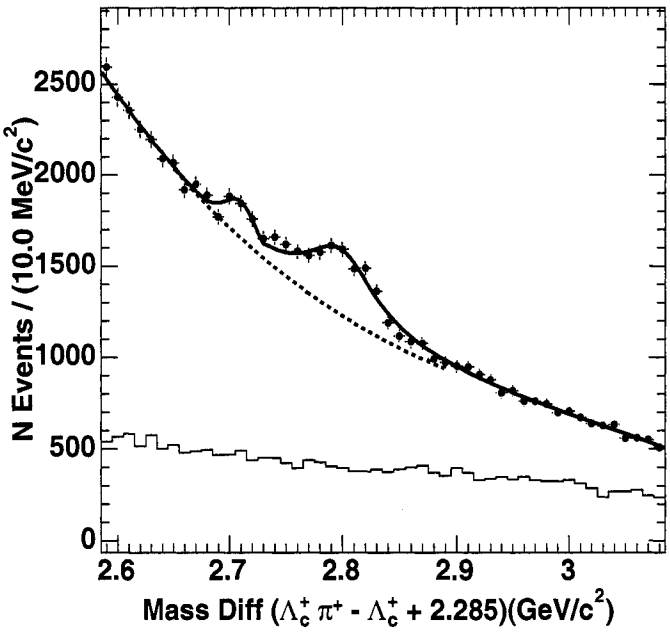

Figure 7.19: *Mass difference distribution* ($\Lambda_c^+\pi^+ - \Lambda_c^+ + 2.285$) *for* $\Lambda_c^+\pi^+$ *combinations in data. The* Λ_c^+ *signal window (points with error bars) and normalized sidebands (histograms) are shown, together with the fits described in the text (solid curves) and their combinatorial background components (dashed).*

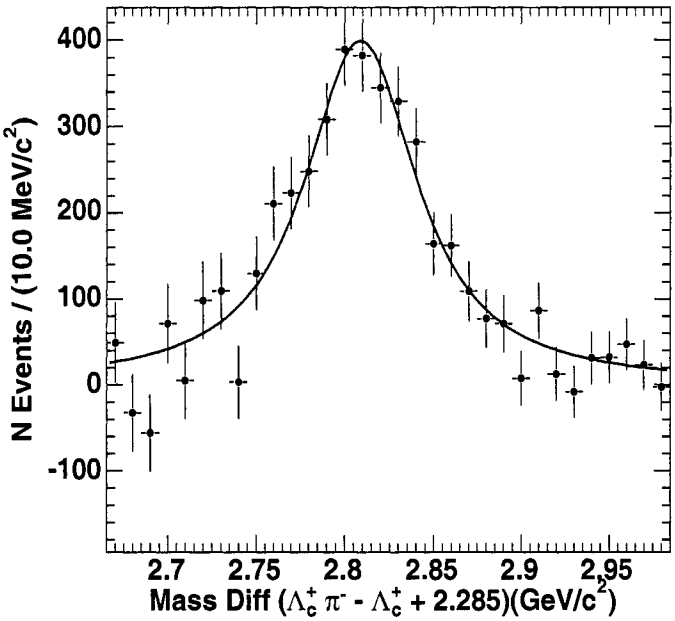

Figure 7.20: *Background subtracted distribution in the signal region (points with error bars) for* $\Sigma_c^0(2800)$ *with the signal component from the fit superimposed.*

7.4.5 Momentum Spectrum of $\Sigma_c^0(2800)$ and $\Sigma_c^{++}(2800)$

To obtain the momentum spectrum of $\Sigma_c(2800)$ baryons in continuum, we divide the momentum range accessible to these particles into ten intervals of scaled momentum, x_p. In each interval we derive the raw Σ_c yields from the data by fitting the appropriate mass difference distribution to a Breit-Wigner convoluted with a Gaussian function and taking into account the contribution from $\Lambda_c^+(2880)$ feed-down. The detector resolution is fixed to the value determined from Monte Carlo for $x_p > 0.7$, because we found that it remains almost constant for all momentum

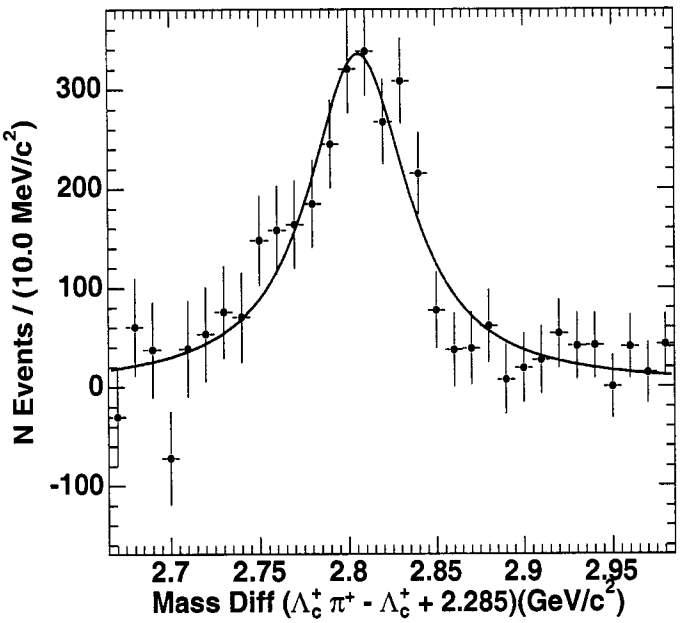

Figure 7.21: *Background subtracted distribution in the signal region (points with error bars) for* $\Sigma_c^{++}(2800)$ *with the signal component from the fit superimposed.*

intervals. The mean and intrinsic width are also fixed to the values obtained from fitting the entire data for $x_p > 0.7$. We do not see any significant signal for x_p values below 0.5 due to high background and so we consider x_p values above 0.5 only. The raw yields are divided by appropriate detection efficiencies for each momentum bin to obtain the corrected yield. Table 7.9 shows the corrected yield in each x_p bin. This corrected yield is a measurement of the number of produced $\Sigma_c(2800)$ baryons per x_p interval. The obtained efficiency-corrected x_p spectra are shown in Figs. 7.22 and 7.23. The curves show fits using Peterson [73] parameterization given by;

$$\frac{dN}{dx_p} \propto \frac{1}{x_p\left(1-\frac{1}{x_p}-\frac{\epsilon}{1-x_p}\right)^2}, \tag{7.2}$$

where ϵ is called the Peterson parameter. We obtain $\epsilon = 0.050 \pm 0.010$ for $\Sigma_c^0(2800)$

Table 7.9: Efficiency corrected yields per x_p bins.

x_p bins	Corrected Yield	
	Σ_c^0	Σ_c^{++}
$0.5 > x_p \geq 0.6$	1726.46 ± 454.17	1932.58 ± 1036.52
$0.6 > x_p \geq 0.7$	2514.04 ± 613.75	3706.13 ± 756.75
$0.7 > x_p \geq 0.8$	4242.32 ± 637.08	6048.88 ± 1511.40
$0.8 > x_p \geq 0.9$	2863.32 ± 411.96	3095.32 ± 1301.48
$0.9 > x_p \geq 1.0$	807.96 ± 134.58	941.30 ± 235.52

and $\epsilon = 0.057 \pm 0.012$ for $\Sigma_c^{++}(2800)$. These values are similar to other measurements for excited charm baryons with non-zero orbital angular momentum [75] and also the ones measured by Belle [26] for $\Sigma_c(2800)$.

7.4.6 Measurement of Production Cross-section of $\Sigma_c(2800)$

The production cross-section σ is given by;

$$\sigma(e^+e^- \rightarrow \Sigma_c(2800)X) = \frac{N_{produced}}{\mathcal{L}} \tag{7.3}$$

where $\mathcal{L}$ is the Luminosity and $N_{produced}$ is the actual number of $\Sigma_c(2800)$'s produced. It is given by;

$$N_{produced} = \frac{N_{corrected}}{\mathcal{B}(\Lambda_c^+ \rightarrow pK^-\pi^+) \times \mathcal{B}(\Sigma_c(2800) \rightarrow \Lambda_c^+\pi)} \tag{7.4}$$

where $N_{corrected}$ is the total corrected yield. Since the $\mathcal{B}(\Sigma_c(2800) \rightarrow \Lambda_c^+\pi^\pm)$ is not known, therefore we calculate $\sigma.\mathcal{B}$ instead which corresponds to,

$$\sigma(e^+e^- \rightarrow \Sigma_c(2800)X).\mathcal{B}({\Sigma_c}^{++/0}(2800) \rightarrow \Lambda_c^+\pi^{+/-}). \tag{7.5}$$

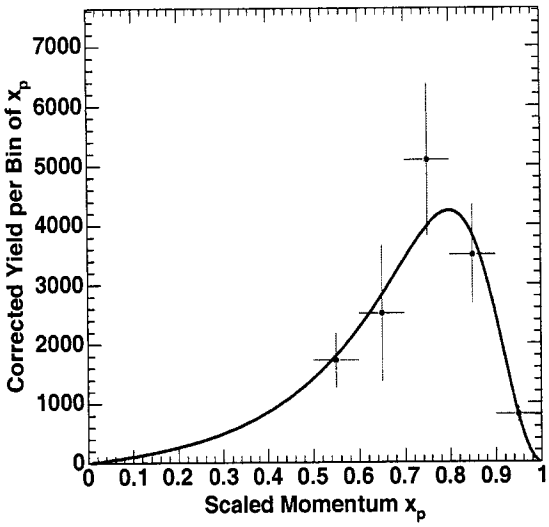

Figure 7.22: *Spectrum of scaled momentum x_p for $\Sigma_c^0(2800)$.*

$N_{corrected}$ is determined by integrating the Peterson function over the x_p range 0.0 to 1.0. We find the following results for the products;

$$\sigma(e^+e^- \rightarrow \Sigma_c^0(2800)X).\mathcal{B}(\Sigma_c^0(2800) \rightarrow \Lambda_c^+\pi^-) = 1.36 \pm 0.42pb \tag{7.6}$$

$$\sigma(e^+e^- \rightarrow \Sigma_c^{++}(2800)X).\mathcal{B}(\Sigma_c^{++}(2800) \rightarrow \Lambda_c^+\pi^+) = 1.68 \pm 0.54pb \tag{7.7}$$

7.5 Systematic Studies

The systematic uncertainties for this analysis are categorized as follows:

1. Tracking Resolution.

2. PID efficiency.

3. Λ_c mass cut.

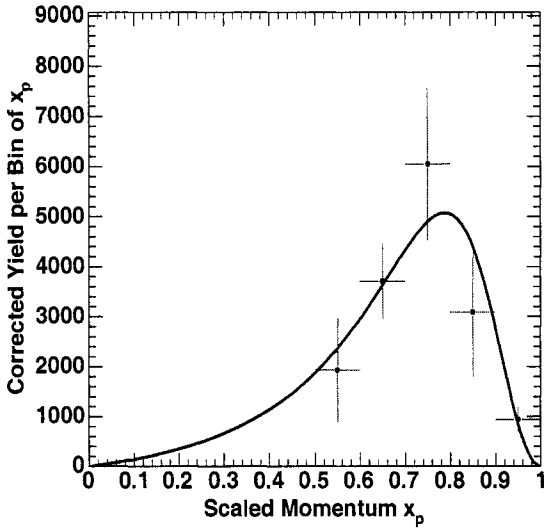

Figure 7.23: *Spectrum of scaled momentum x_p for $\Sigma_c^{++}(2800)$.*

4. χ^2 of the Λ_c Vertex fit.

5. Helicity cut on the π forming the Σ_c.

6. Detector Resolution.

7. Fitting.

8. MC Statistics.

9. Fitting x_p spectrum.

We vary all the cuts one by one and then recalculate $\sigma.\mathcal{B}$. The percentage change with respect to the nominal value is accounted as systematic uncertainty. These uncertainty contributions from various sources are summarized in Table 7.10.

7.5.1 Tracking Resolution

The MC Simulation does not perfectly reproduce the detector's tracking capabilities. We need to make a correction to the efficiency of the signal MC to account for the overestimation of the track-finding efficiency. The Tracking Efficiency Task Force considers the possible tracking resolution differences between the MC and data and recommends to apply an efficiency correction of 0.5% per charged track [76]. This inefficiency leads to a systematic uncertainty of 1.4% per track to each $\sigma.\mathcal{B}$ calculation.

7.5.2 PID Efficiency

PID selectors have been found to be more efficient in MC than in data, and this difference must be corrected. The PID group in *BABAR* provides PID tables for various particle identification selector lists which provide efficiency of each PID selector as a function of transverse momentum, polar and azimuthal angles [77] measured using control data samples. We use these tables to incorporate the efficiency uncertainty and misidentification rate for the selector lists used in this analysis. The systematic uncertainty is 2% for each of pLHVeryTight, KLHVeryLoose and piLHLoose selections.

7.5.3 Λ_c Mass Cut

Both of our decay modes involve Λ_c in the final state. We consider the uncertainty due to the Λ_c mass cut. We change the Λ_c mass window of $\pm 1.7\sigma$ by $\pm\delta\sigma$ where $\sigma \pm \delta\sigma = 6.6 \pm 0.15 \mathrm{MeV/c^2}$ and take into account the uncertainty due to this change.

7.5.4 χ^2 of Λ_c Vertex Fit

We use one decay mode to reconstruct Λ_c, but some other decay mode can have a different distribution for the χ^2 of Λ_c vertex fit. The uncertainty due to the χ^2 cut of > 30 is evaluated by tightening and relaxing the value by 10. The effect of these changes is very small which gives a very small contribution towards systematic uncertainty.

7.5.5 π Helicity Cut

A cut on cos θ_{hel} for the π forming the Σ_c candidates is used to reduce the combinatorial background. But the fact that the total corrected yield could be different for different cos θ_{hel} values, can add to the systematic uncertainty. We change the chosen value of 0.7 to 0.6 and 0.8 to account for the systematic uncertainty. As given in Table 7.10, it adds quite a bit to the total uncertainty.

7.5.6 Detector Resolution

There is an error associated with the detector resolution determined from signal MC. We vary the resolution σ within the error $\pm\delta\sigma$, to determine the uncertainty correction. The uncertainty thus evaluated is negligible.

7.5.7 Fitting

The biggest contribution to systematics comes from the fitting. The final fit is composed of three components, the Gaussian function for reflection, the Breit-Wigner convoluted with a Gaussian resolution function for the signal and a third order polynomial for the background. We study the possible biases due to each component by

varying all the parameters within their errors. The highest uncertainty is taken as the final systematic error due to fitting.

Reflection function

The mean and width for the reflection Gaussian from MC are varied by one standard deviation i.e $\pm 1\sigma$. The change in reflection yield is taken as the systematic uncertainty.

Breit-Wigner function

We vary the mean value and intrinsic width obtained by fitting the $\Sigma_c(2800)$ signal within their errors, while the width of the smearing Gaussian is fixed to the value obtained from the MC. The systematic uncertainty is taken as the change in signal yield.

Polynomial background

We replace the polynomial background function with a lower order one and then with a higher order one to calculate the systematic uncertainty in $\sigma.\mathcal{B}$.

7.5.8 MC Statistics

The statistical errors on efficiencies are calculated using the errors on signal yields in MC. These errors give the systematic uncertainty and can be reduced by using a larger sample of MC events.

7.5.9 Fitting x_p Spectrum

There is an uncertainty associated with the Peterson function used to fit the x_p spectrum. The peterson parameter is varied within one standard deviation i.e. $\pm 1\sigma$, to find the total yield. The change in yield gives the systematic uncertainty due to the momentum spectrum fitting.

7.5.10 Summary Table for Sources of Systematic Uncertainty

The results for the systematic studies are summarized in Table 7.10.

Table 7.10: Sources of systematic uncertainties

Sources of Syst. error	% of Syst. error	
	Σ_c^0	Σ_c^{++}
Tracking	5.6	5.6
PID efficiency	8.0	8.0
Λ_c mass cut	1.0	0.8
χ^2 of Λ_c Vertex Fit	1.1	0.8
π Helicity Cut	18.0	17.5
Det. Res σ	0.1	0.1
Fitting	20.0	16.0
Monte Carlo Statistics	0.4	0.4
Fitting x_p Spectrum	13.5	8.3

All of these sources of systematic error are added in quadrature to give the total systematic error on the $\sigma.\mathcal{B}$ calculations. The total systematic uncertainty is 31.7% for $\Sigma_c^0(2800)$ and 27.0% for $\Sigma_c^{++}(2800)$.

7.5.11 Uncertainty due to $\Lambda_c^+ \to pK^-\pi^+$ Branching Ratio

The branching ratio for $\Lambda_c^+ \to pK^-\pi^+$ is not known very precisely and is $5.0 \pm 1.3\%$ [5]. This uncertainty of 26% on the branching ratio is taken as a separate error on the $\sigma.\mathcal{B}$ measurement.

Chapter 8

Summary and Conclusions

8.1 Summary

We have performed the study of orbitally excited charm baryons $\Sigma_c^0(2800)$ and $\Sigma_c^{++}(2800)$ baryons in *BABAR* using $230\,\mathrm{fb}^{-1}$ of data. These baryons were first observed by the Belle experiment [26] in 2004. We have confirmed their existence in *BABAR*. The final measurements of mass differences, widths and production cross-sections are given below.

Mass Differences

The observed mass difference $(\Lambda_c^+\pi^- - \Lambda_c^+ + 2.285)$ is found to be 2.8008 ± 0.0023 GeV/c^2 and $(\Lambda_c^+\pi^+ - \Lambda_c^+ + 2.285)$ is found to be 2.7980 ± 0.0028 GeV/c^2.

Intrinsic Widths

The intrinsic widths are measured to be $65.6 \pm 14.9\,\mathrm{MeV}$ for $\Sigma_c^0(2800)$ and $67.7 \pm 16\,\mathrm{MeV}$, for $\Sigma_c^{++}(2800)$.

Production Cross-sections

The production cross-sections are calculated to be

$$\sigma(e^+e^- \to \Sigma_c^0(2800)X).\mathcal{B}(\Sigma_c^0(2800) \to \Lambda_c^+\pi^-) = 1.36 \pm 0.42 \pm 0.43 \pm 0.35\ pb \quad (8.1)$$

and

$$\sigma(e^+e^- \to \Sigma_c^{++}(2800)X).\mathcal{B}(\Sigma_c^{++}(2800) \to \Lambda_c^+\pi^+) = 1.68 \pm 0.54 \pm 0.45 \pm 0.44\ pb. \quad (8.2)$$

The first uncertainty is statistical, the second is systematic and the third one is due to the uncertainty in $\Lambda_c^+ \to pK^-\pi^+$ branching fraction.

8.2 Conclusions

The theoretical models described earlier in Chapter2, predict a rich spectrum of excited charm baryons in the vicinity of observed states [29, 51, 52, 46]. One of the candidates is a Σ_{c2} doublet with $J^P = \frac{3}{2}^-$ and $\frac{5}{2}^-$, where the subscript 2 denotes the total angular momentum of the light di-quark system. It is predicted to decay into $\Lambda_c^+\pi$ final state and the predicted mass difference is $(\Lambda_c^+\pi - \Lambda_c) = 500$ MeV/c^2, which is close to our observation. Our mass measurements are not consistent with predicted values of 2.77 GeV/c^2 and 2.654 GeV/c^2 but it is consistent with 2.80 GeV/c^2. The predicted width $\Gamma \approx 12$ MeV is much smaller than what we and Belle observe. However it is also predicted that the $\Sigma_{c2}\{\frac{3}{2}^-\}$ baryon can mix with the nearby $\Sigma_{c0}\{\frac{3}{2}^-\}$ [51, 52] and can produce a wider physical state.

The Belle Collaboration were the first one to report the observation of $\Sigma_c(2800)$ states. They measured mass differences, widths and production cross-sections. We have been able to confirm their observation. For comparison purpose we give our and their measurements in the Table 8.1.

Table 8.1: Comparison of Measurements from *BABAR* and Belle.

Quantity	$\Sigma_c^0(2800)$		$\Sigma_c^{++}(2800)$	
	Belle	*BABAR*	Belle	*BABAR*
Mass Diff. (Σ_c- Λ_c^++ 2.285) (GeV/c^2)	$2.8004\ ^{+0.0032}_{-0.0031}$	2.8008 ± 0.0023	$2.7995\ ^{+0.0034}_{-0.0031}$	2.7980 ± 0.0028
Γ MeV	$61\ ^{+18}_{-13}$	65.6 ± 14.9	$75\ ^{+18}_{-13}$	67.7 ± 16
Peterson Par. ϵ	$0.078\ ^{+0.021}_{-0.017}$	0.050 ± 0.010	$0.069\ ^{+0\ 015}_{-0.012}$	0.057 ± 0.012
$\sigma.\mathcal{B}$ pb	$2.04\ ^{+0.72}_{-0.50}$	1.36 ± 0.42	$2.36\ ^{+0.69}_{-0.50}$	1.68 ± 0.54

From the table we see that all of our measurements are consistent with Belle's measurements. The values for Peterson parameter are consistent but somewhat smaller than theirs, and so are the $\sigma.\mathcal{B}$ measurements.

"We shall not cease from exploration and the end of all our exploring will be to arrive where we started.... and know the place for the first time." –T. S. Eliot

Appendix A

Λ_C Optimization using Data

We cross-check our Λ_c optimization using Run1 data (20 fb^{-1}). We study PID cuts, and track quality cuts for the protons, kaons and pions to achieve the best possible values of the signal significance, $\frac{S}{\sqrt{(S+B)}}$. Here S represents the signal yield of Λ_c candidates obtained from a double-Gaussian fit, and B represents the background count. The results for PID studies are summarized in Tables A.1 and A.2. To suppress the background from random combinations of protons, kaons and pions which do not fit to a good vertex, we require the fit probability P_{χ^2} of the Λ_c vertex to be greater than a certain value. The results for the track quality cuts and P_{χ^2} are given in Table A.3. From these tables we can see that `GoodTracksLoose` for all tracks gives the best value for significance but at the same time we are loosing about 16% of the signal. But it is nevertheless clear that PVTight, KTight and PiLoose are helpful in reducing the background a lot without loosing much of a signal. Our study finds an optimal selection of Λ_c^+ candidates for $P_{\chi^2} > 0.003$. Fig. A.1 shows the optimized mass plot for Λ_c including all Runs 1-4. The signal is fitted using a double Gaussian function and a first order polynomial for the background.

The fitted mean value is 2.2859±0.0000 GeV/c^2. The σ for the first Gaussian is 0.00378±0.00003 GeV and that for the second one is 0.00796±0.00021 GeV. We find around 950,000 Λ_c's candidates available in the whole data, which is quite a big sample to study charm baryons like Σ_c's.

Table A.1: Signal Significance for different PID selections of $\Lambda_c$candidates.

Proton	Kaon	Area	$\frac{S}{\sqrt{(S+B)}}$
PVLoose	KVLoose	168339 ± 8146	125.62
PVLoose	KLoose	150370 ± 6702	129.99
PVLoose	KTight	138811 ± 5195	131.24
PVLoose	KVTight	138837 ± 5226	131.29
PVTight	KVLoose	148914 ± 4796	140.94
PVTight	KLoose	133903 ± 3850	149.25
PVTight	KTight	125106 ± 3040	152.52
PVTight	KVTight	125088 ± 3077	152.53
PTight	KVLoose	142112 ± 3914	150.58
PTight	KLoose	126852 ± 2880	158.91
PTight	KTight	119864 ± 2379	160.34
PTight	KVTight	119816 ± 2382	160.34
PVTight	KVLoose	133690 ± 3348	153.24
PVTight	KLoose	119851 ± 2518	162.79
PVTight	KTight	113521 ± 2130	166.37
PVTight	KVTight	113496 ± 2087	166.36

† PVTight & KTight are the optimized cuts.

Table A.2: Pion PID cuts study for Λ_c

Pion Criteria	Area	$\frac{S}{\sqrt{(S+B)}}$
PiLoose	112151 ± 2102	167.19
PiTight	108925 ± 1982	167.97
PiVTight	104285 ± 2008	162.86

† PVTight and KTight are used for this study.

‡ PiLoose is considered to be the optimized cut here, although PiTight has better significance but PiLoose has almost the same significance with a bigger signal area.

Table A.3: Track Quality and P_{χ^2} cuts study for Λ_c

Particle Criteria	Area	$\frac{S}{\sqrt{(S+B)}}$
P GoodTracks VeryLoose	107471 ± 1420	178.55
P & K GoodTracks VeryLoose	106651 ± 1338	180.34
P, K & πGoodTracks VeryLoose	104850 ± 1102	185.09
P GoodTracks Loose	105037 ± 1352	182.33
P & K GoodTracks Loose	97825 ± 1202	183.58
P, K & πGoodTracks Loose	90572 ± 981	189.08
P_{χ^2}>0.002	88581 ± 740	194.23
P_{χ^2}>0.003	88226 ± 724	196.11
P_{χ^2}>0.004	87860 ± 719	195.89
P_{χ^2}>0.005	87652 ± 738	195.94
P_{χ^2}>0.006	87427 ± 718	193.95

† PVTight, KTight and PiLoose cuts are used here.

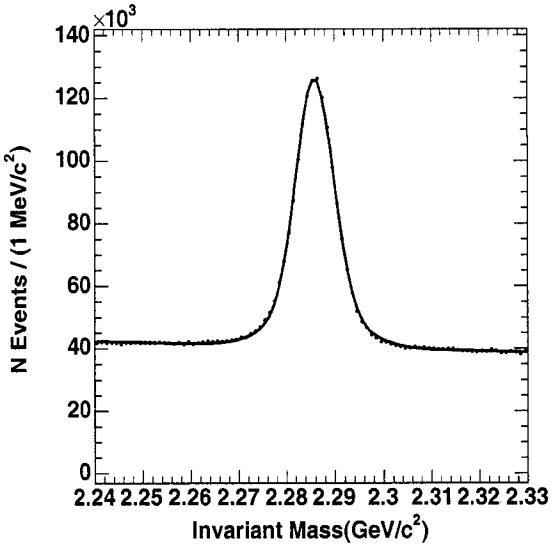

Figure A.1: *Optimized Mass Distribution for Λ_c for the whole data.*

To summarize, we find the following optimized cuts for Λ_c using data.

- PID : PrVTight, KTight, PiLoose,
- Probability of Λ_c vertex > 0.003, and
- all tracks are GoodTracksLoose.

Appendix B

Σ_C γ Study

In the mass difference plots for $\Sigma_c(2800)$, by Belle [26] in Fig. 3.5, we see two peaks at a mean value of 0.43 GeV/c^2 and 0.51 GeV/c^2. We check for possible feed-downs at these two mean values in data by adding a photon. These studies are performed using $\approx 130\,\text{fb}^{-1}$ of data.

We combine the selected Σ_c candidates, falling under the criteria given in section 7.3, with all the photons in the event. The photon candidates are selected from the `GoodPhotonLoose` list. To have good quality photons, we require a simple cut on the ratio of the total energy deposited in the central 3x3 array of crystals to the total energy deposited in the 5x5 array of crystals to be > 0.98. We define two mass bands, the first one has all the Σ_c candidates with reconstructed mass so that $2.68 < (\Sigma_c - \Lambda_c + 2.585) < 2.73$ GeV/c^{2}and the second has the ones with $2.74 < (\Sigma_c - \Lambda_c + 2.585) < 2.86$ GeV/c^2. The distributions for the two mass bands of the $\Sigma_c^0(2800)$ are given in Figs. B.1 and B.2. The white histogram corresponds to $E_\gamma > 50\,\text{MeV}$ and the shaded one correspond to $E_\gamma > 100\,\text{MeV}$. The corresponding plots for $\Sigma_c^{++}(2800)$ are given in Figs. B.3 and B.4. The photon studies show no

prominent feature in the two mass bands.

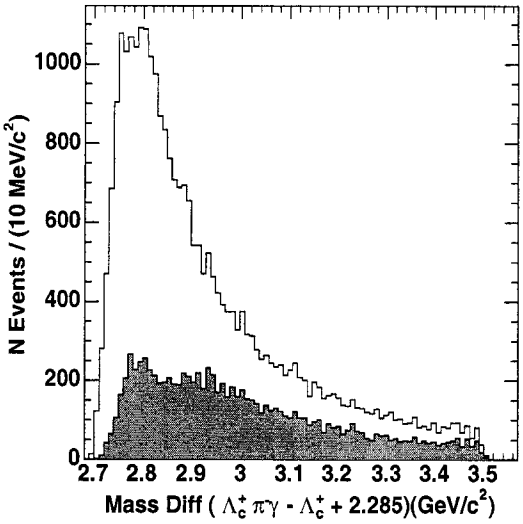

Figure B.1: *Distribution for the Mass Difference* ($\Lambda_c^+\pi^-\gamma$- Λ_c^+) *in data for the first mass band* ($2.68 < (\Lambda_c^+\pi^- - \Lambda_c^+ + 2.285) < 2.73\mathrm{GeV/c^2}$).

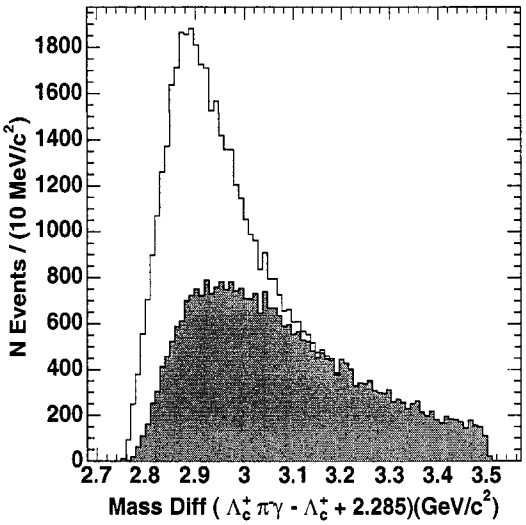

Figure B.2: *Distribution for the Mass Difference ($\Lambda_c^+\pi^-\gamma$- Λ_c^+) in data for the second mass band ($2.74 < (\Lambda_c^+\pi^- - \Lambda_c^+ + 2.285) < 2.86\mathrm{GeV/c^2}$)*

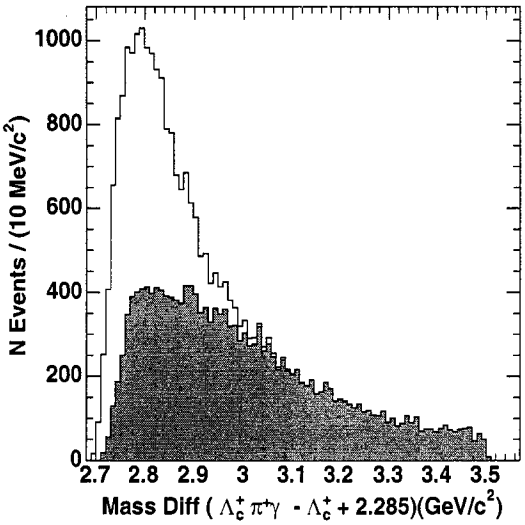

Figure B.3: *Distribution for the Mass Difference ($\Lambda_c^+\pi^+\gamma$- Λ_c^+) in data for the first mass band ($2.68 < (\Lambda_c^+\pi^+ - \Lambda_c^+ + 2.285) < 2.73\mathrm{GeV/c^2}$).*

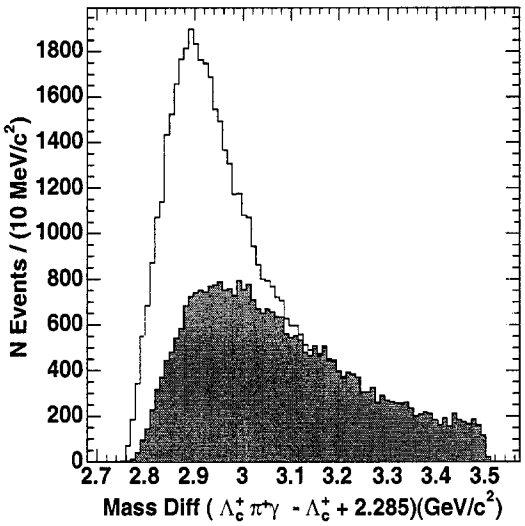

Figure B.4: *Distribution for the Mass Difference* ($\Lambda_c^+\pi^+\gamma$- Λ_c^+) *in data for the second mass band* ($2.74 < (\Lambda_c^+\pi^+ - \Lambda_c^+ + 2.585) < 2.86\mathrm{GeV/c^2}$).

References

[1] URL=http://www.pbs.org/wgbh/aso/databank/entries/baleav.html

[2] A. H. Mahmood, "Observation of Several new Charmed-Strange Baryon States at CESR-CLEO II", Ph.D. Dissertation, 1998. F. R. Wappler, "Measurement of Inclusive Production of Λ_c^+ and Σ_c Baryons in B Decays.", Ph.D. Dissertation, 2000.

[3] Big-Bang Nucleosynthesis by B.D.Fields and S.Sarkar, astro-ph/0601514, 23 Jan (2006).

[4] D. Griffiths, *Introductory Elementary Particles*, Harper & Row Pub., New York, (1987).

D. Perkins, *Introduction to High Energy Physics*, 3rd Ed., Addison-Wesley, California, 1987.

I.S. Hughes, *Elementary Particles*, 3rd Ed., Cambridge Univ. Press, Cambridge, 1990.

F. Halzen and A.D. Martin, *Quarks and Leptons: An Introductory course in Modern Particle Physics*, John Wiley & Sons, 1983.

[5] Particle Data Group, S. Eidelman *et al.*, Review of Particle Physics, Phys. Lett. B **592**, 1-1109 (2004).

[6] S. Weinberg, A. Salam, and S. Glashow, Rev. Mod. Phys. **52**, 515 (1980);
S. L. Glashow, Nucl. Phys. **B22**, 579 (1961);
A. Salam and J. C. Ward, Phys. Lett. **13**, 168 (1964);
S. Weinberg, Phys. Rev. Lett. **19**, 1264 (1967).

[7] P. W. Higgs, Phys. Lett. B **12**, 132 (1964);
P. W. Higgs, Phys. Rev. **145**, 1156 (1966).

[8] M. Kobayashi and T. Maskawa, Prog. Theor. Phys. **49**, 652 (1973).

[9] S. L. Glashow, J. Iliopoulos, and L. Maiani, Phys. Rev. D **2**, 1285 (1970).

[10] J. E. Augustin *et al.* Rev. Lett. **33**, 1406 (1974).

[11] J. J. Aubert *et al.* Rev. Lett. **33**, 1404 (1974).

[12] G. Arnison *et al.*, Phys. Lett. B **122**, 103 (1983) and **126B**, 398 (1983).
For a review of these discoveries, see E. Radermacher, Prog. Part. Nucl. Phys. **14**, 231 (1985).

[13] S. W. Herb *et al.*, Phys. Rev. Lett. **39**, 252 (1977).

[14] C. Berger *et al.*, Phys. Lett. B **76**, 243 (1978);
C. W. Darden *et al.*, Phys. Lett. B **76**, 246 (1978).

[15] S. Okubo, Phys. Lett. **5**, 165 (1963);
G. Zweig, CERN Reps. TH-401, 412 (1964);
J. Iizuka, Suppl. Prog. Theor. Phys. **37-38**, 21 (1966).

[16] E. G. Cazzoli *et al.*, Phys. Rev. Lett. **34**, 1125 (1975).

[17] J. G. Körner, H. W. Siebert, *Heavy Baryons: Theory and Experiment*, Annu. Rev. Nucl. Part. Sci., 41 511 (1991).

[18] W. Greiner and B. Müller, '*Quantum Mechanics Symmetries*, Springer-Verlag.

[19] Rob Kütschke, *Heavy Flavor Spectroscopy*, and the citations therein.

[20] BEBC TST Collaboration, RAL Note (1980).

[21] H. Albrecht, *et al.* (ARGUS Collaboration), Z. Phys. C **C56**, 1 (1992).

[22] G. Crawford *et al.*, Phys. Rev. Lett. **71**, 3259 (1993).

[23] M. Procario *et al.* (CLEO Collaboration), Phys. Rev. Lett. **73**, 1306 (1994).

[24] J. M. Link, *Measurement of the* Σ_c^{++} *and* Σ_c^0 *mass splittings FOCUS*, Phys. Lett. B **488**, 218 (2000).

[25] V. Ammosov *et al.*, JETP Lett. **58**, 247 (1993).

[26] R. Mizuk *et al.* (BELLE Collaboration), Phys. Rev. Lett. **94**, 122002 (2005).

[27] C. Itoh, T. Minamikawa, K. Miura and T. Watanabe, Prog. Theor. Phys. **54**, 908 (1975).

[28] C. Itoh, T. Minamikawa, K. Miura and T. Watanabe, Phys. Rev. D **40**, 3660 (1989).

[29] L. Copley, N. Isgur and G. Karl, Phys. Rev. D **20**, 768 (1979).

[30] J. G. Korner, M. Kramer and D. Pirjol, hep-ph/9406359, June 1994.

[31] T.M. Yan *et al.*, Phys. Rev. D **46**, 1148 (1992).

[32] M. J. Savage, Phys. Lett. **B359**, 189 (1995).

[33] D. Lichtenberg, Phys. Rev. D **16**, 231 (1977).

[34] W. Hwang and D. Lichtenberg, Phys. Rev. D **35**, 3526 (1987).

[35] S. Capstick, Phys. Rev. D **36**, 2800 (1987).

[36] C. Itoh, T. Minamikawa, K. Miura and T. Watanabe, Prog. Theor. Phys. **80**, 208 (1988).

[37] D. Lichtenberg, Phys. Rev. D **48**, 1315 (1993).

[38] J. Dey, M. Dey and P. Volkovitsky, Phys. Lett. **B261**, 358 (1991).

[39] T. Ito *et al.*, Z. Phys., **C59** 57 (1993).

[40] R. Roncaglia, D. B. Lichtenberg, and E. Predazzi, Phys. Rev. **D52**, 1722 (1995).

[41] D. Lichtenberg and R. Roncaglia, Phys. Lett. **B358**, 106 (1995).

[42] D. Lichtenberg and R. Roncaglia, Phys. Rev. D **53**, 6678 (1996).

[43] J. Rosner, Phys. Rev. D **52**, 6461 (1995).

[44] A. Falk, Phys. Rev. Lett. **77**, 223 (1996);
A. Falk, Int. J. Mod. Phys. **A12** 4079 (1997).

[45] E. Jenkins, Phys. Rev. D **54**, 4515 (1996).

[46] L. Glozman and D. Riska, hep-ph/9509269, May 1997.

[47] C. Itoh, T. Minamikawa, K. Miura and T. Watanabe, Phys. Rev. D **61**, 057502 (1989).

[48] N. Mathur, R. Lewis and R. M. Woloshyn, Phys. Rev. D **66**, 014502 (2002) [arXiv:hep-ph/0203253].

[49] C. Albertus, J. E. Amaro, E. Hernandez and J. Nieves, Nucl. Phys. A **755**, 439 (2005) [arXiv:hep-ph/0501085].

[50] D. Ebert, R. Faustov and V. Galkin, Phys. Rev. D **72**, 034026 (2005) [arXiv:hep-ph/0504112].

[51] D. Pirjol and T. Yan, Phys. Rev. D **56**, 5483 (1997).

[52] G. Chiladze and A. Falk, Phys. Rev. D **56**, 6738 (1997).

[53] C. Baltay *et al.*, Phys. Rev. Lett. **42**, 1721 (1979).

[54] E. M. Aitala *et al.*, Phys. Lett. **379B**, 292 (1996).

[55] M. Artuso *et al.*, Phys. Rev. Lett. **65**, 071101 (2002).

[56] A. Warburton, hep-ex/0009040 Sep 15, 2000.

[57] G. Brandenburg *et al.*, Phys. Rev. Lett. **78**, 2304 (1997).

[58] B. Athar *et al.* (CLEO Collaboration), Preprint CNLS 04/1893 (submitted to Phys. Rev.).

[59] S. Capstick, Phys. Rev. D **36**, 2800 (1987). W. Y. P. Hwang and D. Lichtenberg, Phys. Rev. D **35**, 3526 (1987). R. E. Cutkosky and P. Geiger, Phys. Rev. D **48**, 1315 (1993).

[60] M. Artuso *et al.*, Phys. Rev. Lett. **86**, 4479 (2001).

[61] P. F. Harrison and K. R. Quin [*BABAR* Collaboration], *The BABAR Physics Book at the asymmetric B factory.* URL=http://www.slac.stanford.edu/BFROOT/www/doc/PhysBook /physBook.html.

[62] B. Aubert *et al.*, Nucl. Instrum. Methods A **479**, 1 (2002).

[63] URL=http://www.slac.stanford.edu/BFROOT/www/Physics/Tools/PepBeam.

[64] D. H. Perkins, *Introduction to High Energy Physics*, Addison-Wesley (1987).

[65] URL=http://www.slac.stanford.edu/BFROOT/www/DataQuality/

[66] P. Billior, *Track fitting with Multiple Scattering; A New Method* Nucl. Instrum. Methods A **225**, 352 (1984).

[67] URL=http://www.slac.stanford.edu/BFROOT/www/Computing/Offline /Reconstruction/CompRecTracking.html

[68] URL=http://www.slac.stanford.edu/BFROOT/www/doc/workbook /eventstore/nanomicrosummary/Micro/CandLists.html

[69] C. Roat, *Identification of Hadrons for Λ_c Reconstruction in BABAR.* BAD402 (*BABAR* Internal Document).

[70] URL=http://www.slac.stanford.edu/BFROOT/www/Physics/Tools/Pid /Hadrons/pid_summarytable.html

[71] URL=http://www.thep.lu.se/ torbjorn/jetset/pythialc.html

[72] URL=http://www.slac.stanford.edu/BFROOT/www/Computing/Offline /Simulation/web/Workshop040712/davidw.pdf

[73] C. Peterson *et al.*, Phys. Rev. D **27**, 105 (1983).

[74] P. Avery *et al.*, Phys. Rev. **D43**, 3599 (1991).

[75] K. Edwards *et al.*, Phys. Rev. Lett. **74**, 3331 (1995).

[76] URL=http://www.slac.stanford.edu/BFROOT/www/Physics /TrackEfficTaskForce/TrackingTaskForce-2004.html#Recipes.

[77] URL=http://www.slac.stanford.edu/BFROOT/www/Physics/Tools
/Pid/pid.html.